

Infrared Photodetectors Based on 2D Materials and Nanophotonics

Jiajia Zha, Mingcheng Luo, Ming Ye, Tanveer Ahmed, Xuechao Yu, Der-Hsien Lien, Qiyuan He, Dangyuan Lei, Johnny C. Ho, James Bullock,* Kenneth B. Crozier,* and Chaoliang Tan*

2D materials, such as graphene, transition metal dichalcogenides, black phosphorus, and tellurium, have been demonstrated to be promising building blocks for the fabrication of next-generation high-performance infrared (IR) photodetectors with diverse device architectures and impressive device performance. Integrating IR photodetectors with nanophotonic structures, such as surface plasmon structures, optical waveguides, and optical cavities, has proven to be a promising strategy to maximize the light absorption of 2D absorbers, thus enhancing the detector performance. In this review, the state-of-the-art progress of IR photodetectors is comprehensively summarized based on 2D materials and nanophotonic structures. First, the advantages of using 2D materials for IR photodetectors are discussed. Following that, 2D material-based IR detectors are classified based on their composition, and their detection mechanisms, key figures-of-merit, and the principle of absorption enhancement are discussed using nanophotonic approaches. Then, recent advances in 2D material-based IR photodetectors are reviewed, categorized by device architecture, i.e., photoconductors, van der Waals heterojunctions, and hybrid systems consisting of 2D materials and nanophotonic structures. The review is concluded by providing perspectives on the challenges and future directions of this field.

imaging, optical communication, security surveillance, remote sensing, and gas identification.^[1–8] To date, commercially available IR photodetectors with excellent performance typically rely on compound semiconductors with 3D crystal structures, such as II–VI $\text{Hg}_x\text{Cd}_{1-x}\text{Te}$ and III–V $\text{In}_x\text{Ga}_{1-x}\text{As}$ or InSb , as well as type-II InAs/GaSb superlattices.^[9–12] However, these mature IR photodetector technologies still suffer from several drawbacks, for example, complex fabrication processes, volume-dependent thermal noise, and limited pixel size, and one may conclude overcoming these challenges would enable IR photodetectors to be deployed even more widely.^[13–16] The emergence of atomically thin layered 2D materials stacked by weak van der Waals (vdW) interaction, such as graphene, black phosphorus (bP), tellurium (Te), and platinum diselenide (PtSe_2), introduces a promising solution to the above-mentioned problems encountered by current IR photodetectors.^[1,6,17–20] Compared with

bulk compound semiconductors used for IR photodetectors, 2D materials have advantages that include relatively simple fabrication processes, high-quality surfaces that are free from dangling bonds in high densities, strong light–matter interactions per unit volume, and facile heterojunction construction, excellent mechanical flexibility, and the compatibility


1. Introduction

Infrared (IR) photodetectors, here defined as those that can detect light within the wavelength range of 0.8–30 μm , have attracted considerable research interest over the past few decades because of wide-ranging applications in medical

J. Zha, M. Luo, C. Tan
Department of Electrical Engineering
City University of Hong Kong
83 Tat Chee Avenue, Kowloon, Hong Kong, China
E-mail: chaoltan@cityu.edu.hk

M. Ye, J. Bullock, K. B. Crozier
Department of Electrical and Electronic Engineering
University of Melbourne
Melbourne, Victoria 3010, Australia
E-mail: james.bullock@unimelb.edu.au

T. Ahmed, D.-H. Lien
Institute of Electronics
National Yang Ming Chiao Tung University
Hsinchu 30010, Taiwan

 The ORCID identification number(s) for the author(s) of this article can be found under <https://doi.org/10.1002/adfm.202111970>.

DOI: 10.1002/adfm.202111970

X. Yu
Engineering Department
University of Cambridge
9, JJ Thomson Avenue, Cambridge CB3 0FA, UK

Q. He, D. Lei, J. C. Ho
Department of Materials Science and Engineering
City University of Hong Kong
83 Tat Chee Avenue, Kowloon, Hong Kong, China

K. B. Crozier
School of Physics
University of Melbourne
Melbourne, Victoria 3010, Australia
E-mail: kcrozier@unimelb.edu.au

K. B. Crozier
Australian Research Council (ARC) Centre of Excellence
for Transformative Meta-Optical Systems (TMOS)
University of Melbourne
Melbourne, Victoria 3010, Australia

with complementary metal–oxide–semiconductor (CMOS) devices.^[21–25] To this end, much effort has been devoted to the fabrication of IR photodetectors based on 2D materials, exploring conceptual novelties in terms of architectures and materials for improved IR photodetection performance.^[7,26–31]

A variety of design schemes for 2D material-based IR photodetectors have been demonstrated. Among various devices, although it has been experimentally demonstrated that 2D material-based IR photodetectors can exhibit impressive response speeds (e.g., >500 GHz),^[32] broad IR spectral response (e.g., 0.8–10.6 μm),^[13,33] low dark current (e.g., 220 nA),^[34] and large-scale integration (e.g., 388 \times 288 array),^[35] their photore sponsivities are often somewhat low due to the weak light absorption that occurs in these ultrathin materials. This motivates the development of light absorption-enhancement strategies, with the goal of improving the responsivity of 2D material-based IR photodetectors so that they can be used in practical applications.^[36,37] Some of the appealing routes to improve the light absorption of 2D material-based IR photodetectors include integrating 2D materials with nanophotonic structures^[38–40] such as surface plasmon (SP) structures,^[41,42] optical waveguides,^[3,34] and optical microcavities.^[43–45] These configurations can provide considerable light absorption enhancement, while simultaneously maintaining their excellent electrical properties that can include low noise levels and high carrier mobility.

In this review, we summarize critically the state-of-the-art progress made in IR photodetectors based on 2D materials and nanophotonics. The advantages and categories of 2D materials used for IR photodetectors are first discussed. This is followed by discussions of detection mechanisms and relevant figures-of-merit. Next, the principle of light absorption enhancement is discussed, in the context of three classes of nanophotonic structures. Following this, we discuss the experimental realizations of 2D material-based IR photodetectors. These are classified according to device structures into photoconductors, vdW heterojunctions, and hybrid systems with integrated optical nanostructures for stronger light absorption. Our paper concludes with a discussion of the challenges and prospects of this burgeoning research field.

2. Advantages of Layered 2D Materials for Infrared Photodetectors

Due to their unique crystal structures, 2D materials exhibit advantages as absorbers in IR photodetectors compared to traditional materials with 3D crystal structures (e.g., $\text{Hg}_x\text{Cd}_{1-x}\text{Te}$, $\text{In}_x\text{Ga}_{1-x}\text{As}$, InSb , and Ge). These advantages are schematically illustrated as **Figure 1** and can be summarized as follows. 1) Surfaces of 2D materials are naturally passivated without high densities of dangling bonds, since van der Waals interactions replace covalent bonds in the out-of-plane direction in 2D materials.^[22,25] This allows 2D material-based IR photodetectors to be readily integrated with photonic structures, such as waveguides,^[46] and prevents surface-induced performance degradation, i.e., photoexcited carrier recombination at surface defects, meaning that 2D material-based IR photodetectors can have high internal quantum efficiency (IQE).^[14] 2) Adjacent layers in 2D material heterojunctions are bonded by weak vdW forces as

in their bulk forms,^[25,47–49] which allows the construction of vertical heterojunctions by simply stacking different 2D materials together without the issues of lattice mismatch and deposition temperature that one would have for conventional heterostructures.^[7] 3) Compared with photodetectors based on conventional 3D materials, those based on 2D materials will often have smaller volumes, which can result in lower noise. This advantage endows 2D material-based IR photodetectors with the possibility of a high signal-to-noise ratio at room temperature without the need for active cooling.^[50] 4) 2D materials often have strong light–matter interaction per unit volume, which facilitates the excitation of electron–hole pairs by incident photons.^[51,52] The light absorption in 2D materials can thus still be significant, despite their atomic thickness. For example, single-layer graphene absorbs $\approx 2.3\%$ of normally incident light in the infrared-to-visible spectral region.^[26,53–55] Similarly, bP with a thickness of 70 nm can achieve an optical absorption of $\approx 40\%$ for polarized illumination at a wavelength of $\lambda = 0.95 \mu\text{m}$.^[56] 5) 2D materials can be prepared into wafer-scale thin films on different substrates by various methods. An important method is chemical vapor deposition (CVD),^[57–59] which is much more cost-effective than epitaxial growth methods traditionally used for the synthesis of II–VI $\text{Hg}_x\text{Cd}_{1-x}\text{Te}$ and III–V $\text{In}_x\text{Ga}_{1-x}\text{As}$, such as molecular beam epitaxy (MBE) and metal–organic CVD (MOCVD).^[60] 2D materials thus present the opportunity for monolithic integration with CMOS technology because they can be produced by wafer-scale CVD growth and then transferred to almost any substrate, including silicon CMOS.^[35]

3. Categories of Layered 2D Materials Used for Infrared Photodetectors

Since the first report on graphene in 2004 by Novoselov et al.,^[61] a large number of 2D materials have been synthesized and explored, and with this number still increasing rapidly.^[62–65] Within this fast-growing family of 2D materials, only a small portion are suitable for IR photodetectors. At the time of writing, the most commonly used 2D materials for IR photodetectors are graphene, transition metal dichalcogenides (TMDs, e.g., MoS_2 , MoTe_2 , WSe_2 , and WS_2), bP with black arsenic phosphorus (b- $\text{As}_x\text{P}_{1-x}$), noble metal dichalcogenides (e.g., PtSe_2 and PdSe_2), and Te with selenium–tellurium alloys ($\text{Se}_x\text{Te}_{1-x}$). **Figure 2** summarizes the bandgap values and the corresponding wavelength ranges of 2D materials used for IR photodetectors. The IR regime can be divided into the near infrared (NIR, 0.8 to 1 μm), the short-wave infrared (SWIR, 1 to 3 μm), the mid-wave infrared (MWIR, 3 to 5 μm), the long-wave infrared (LWIR, 8 to 12 μm), and the far infrared (FIR, 12 to 30 μm).^[22]

The first frequently used 2D material for IR photodetection was graphene, whose optical and electrical properties have been studied comprehensively.^[66] Intrinsic graphene is a semimetal with zero bandgap and its optical absorption characteristics are largely independent of wavelength.^[53] However, through chemical doping, the electronic properties of graphene can be tuned. For device applications, especially for IR photodetectors, it is desirable to induce a bandgap.^[67,68] By controlling the doping, graphene's bandgap can be adjusted widely, enabling tailoring

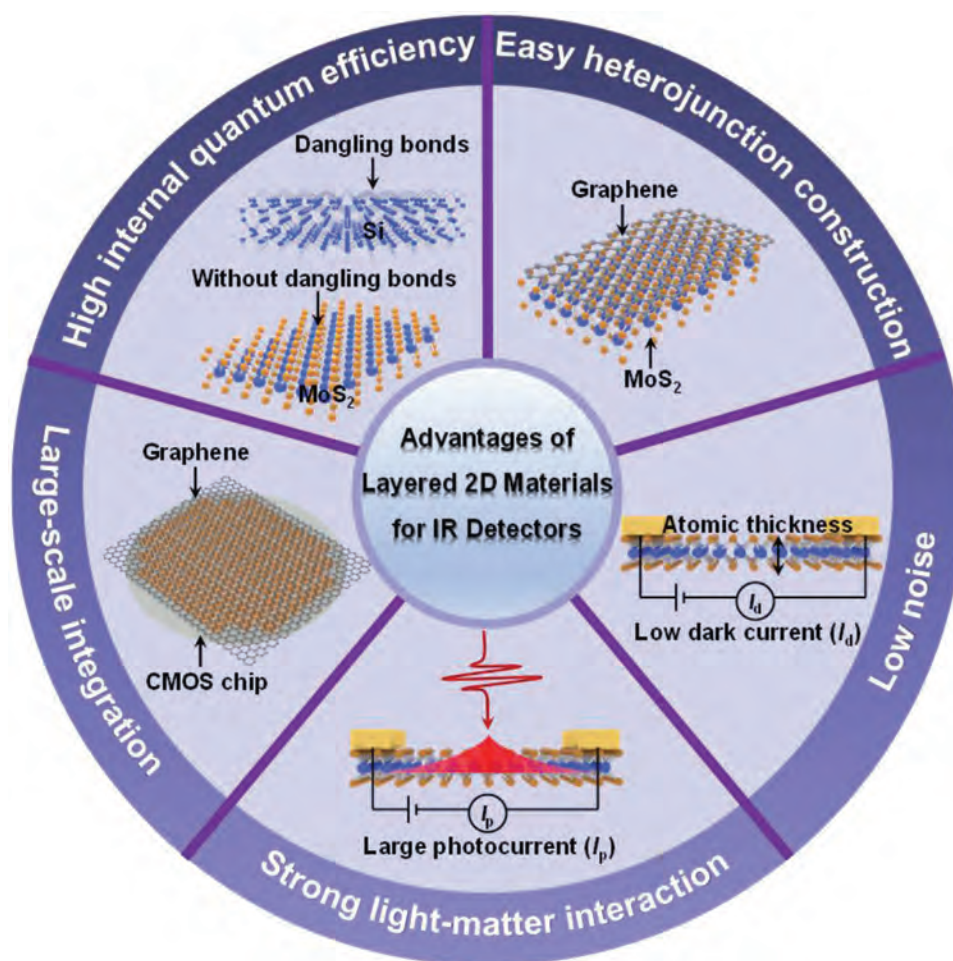


Figure 1. Schematic illustration of the advantages of 2D materials used for IR photodetectors as compared to 3D bulk materials.

of the photoresponse from the visible to the terahertz portions of the spectrum. In addition, graphene itself can support plasmon waves in the MWIR to THz regimes.^[69,70] Plasmon resonances introduced by nanopatterning can enhance light absorption significantly, improving the performance of the graphene-based IR photodetectors.^[41] In addition, in hybrid graphene/quantum dot (QD) phototransistors, graphene can serve as the carrier transport channel, which results in exceptionally high gain.^[71,72]

Most of the semiconducting TMDs possess bandgaps of 1.0–2.5 eV that are large by comparison to graphene. Among 2D TMDs, the most widely explored might be MoS₂. This is because its high stability makes it favorable for optoelectronic devices. Nevertheless, the large bandgaps of 2D TMDs make them unsuitable as active IR absorbers. The creation of van der Waals heterostructures with strong interlayer coupling and decoration with QDs have been used in 2D TMD-based IR photodetectors. For example, atomically thin MoTe₂ or WS₂ can be staggered with MoS₂ to form a type-II heterostructure,^[73,74] whereby IR absorption occurs between the conduction band minimum (CBM) and valence band maximum (VBM) of the two separate materials.^[75,76] This concept provides tunable interlayer band alignment through the stacking of different

2D materials, providing a useful handle for tailored optoelectronics.^[77] In addition, integrating 2D TMDs with sensitizers, especially QDs (e.g., PbS and HgTe), is another way to achieve IR photoresponse using 2D TMD-based photodetectors.^[4,78] Upon the IR light illumination, electrons generated by the QDs layer, which is deposited onto the 2D TMDs, can be transferred into the channel materials. Under an applied voltage, these transferred electrons can drift toward the drain. This configuration can provide exceptionally high IR responsivity, especially at low illumination intensities. Moreover, the peak position of photoresponse spectral can be tuned by the size of the QDs.

Another subset of widely explored 2D materials comprises elemental bP and its alloy with arsenic. These show potential for high specific detectivity photodetection in the MWIR and LWIR regimes.^[79–83] Bulk bP exhibits a direct bandgap of about 0.3 eV, which increases to about 2.0 eV in the monolayer form.^[56] By forming an alloy with arsenic (i.e., b-As_xP_{1-x}), the bulk bandgap can be reduced to ≈0.26–0.15 eV, as reported in different studies.^[84]

The atomically thin 2D noble metal dichalcogenides are another family of potential candidates for high-performance MWIR and LWIR photodetectors. Monolayer and bilayer PtSe₂ have indirect bandgaps of about 1.2 and 0.3 eV, respectively,

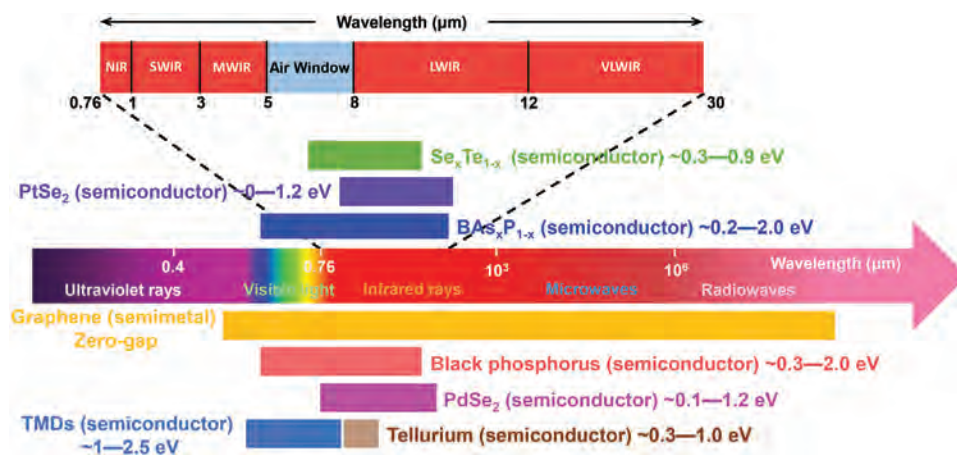


Figure 2. Classification of IR radiation (upper panel) and summary of optical bandgaps of various 2D materials used for IR photodetectors and their corresponding wavelength ranges (bottom panel).

while bulk PtSe₂ is semimetallic.^[85] Similarly, PdSe₂ is another 2D noble metal dichalcogenides with promising IR detection possibilities.^[13,86,87] Both monolayer and bilayer PdSe₂ flakes have indirect bandgaps, which decrease with layer number. From first-principles calculations, the indirect and direct bandgaps for monolayer PdSe₂ are ≈1.23 and 1.43 eV, respectively. For bilayer and trilayer PdSe₂, the indirect bandgaps are 0.85 and 0.64 eV, respectively. The small bandgap of multilayer PtSe₂ (i.e., <0.2 eV) and PdSe₂ (i.e., <0.1 eV) also enable them to bridge the gap between the MWIR and LWIR regimes.^[88,89]

Recently, Te and Se_xTe_{1-x} alloys have proven to be promising materials for SWIR and MWIR photodetectors. As a true 1D crystal, Te has no dangling bonds on the edges and surfaces. This property is very favorable for electronics and optoelectronics.^[14,90-92] Like the aforementioned TMDs, the bandgaps of Te are thickness-dependent.^[93] For bulk to monolayer Te, the bandgap value varies from 0.31 to 1.04 eV. In addition, partially substituting Te atoms with Se atoms to form Se_xTe_{1-x} alloys can maintain tellurium's crystal structure. As an additional benefit, the bandgap values of Se_xTe_{1-x} films can be continuously tuned from 0.31 eV (Te) to 1.87 eV (Se) by changing the ratio of Se to Te.^[45] This bandgap values range of Te and Se_xTe_{1-x} covers the SWIR regime.

4. Detection Mechanism and Figures-of-Merit for IR Photodetectors

In this section, the detection mechanisms and key figures-of-merit of IR photodetectors are described. IR photodetectors are devices that detect IR light by converting incident IR radiation into electronic signals, such as photocurrent and photovoltage. The detection mechanisms of these photodetectors can be classified into two categories, namely, the photon-related detection mechanisms and thermal-related mechanisms. First, we describe the photon-related detection mechanisms, including the photoconductive effect (PCE), the photogating effect (PGE), and the photovoltaic effect (PVE), in which electron-hole pairs are generated by optical transitions. Then, we introduce the thermal-related detection mechanisms, including

the photothermoelectric effect (PTE) and the photobolometric effect (PBE), in which the thermal effect of IR radiation leads to the variation of electrical properties. Last, we introduce the key figures-of-merit for IR photodetectors to better compare the performance of devices with different geometries and operating principles.

4.1. Detection Mechanisms of IR Photodetectors

4.1.1. PCE

The photoconductive effect, as shown in **Figure 3a**, occurs when extra carriers excited by incident photons increase the free carrier concentration and thus the channel conductivity of a material. By applying external biases between a set of symmetrical contacts on this material, these extra carriers can be extracted via the contacts to generate photocurrent. As shown in **Figure 3a**, under dark conditions, the free carriers of the absorbers are driven by an applied bias (V_{ds}), meaning that there is a dark current (I_{dark}). Under illumination, the absorbed photons with energies greater than the bandgap ($h\nu > E_{bg}$) generate electron-hole pairs, which are separated by the applied V_{ds} and collected by metal electrodes, thus yielding a current (I_{light}) that is larger than the dark current. This net increase in current is termed the photocurrent (I_{photo}) and can be written as $I_{photo} = I_{light} - I_{dark}$.

The most common device architecture of photoconductors is the photo-field-effect-transistor (photo-FET), in which the gate electrode is isolated from the semiconductor channel by an insulating layer (**Figure 3b**). Note that photo-FETs normally adopt back-gate configurations, as this avoids the incident light from being blocked by metal electrodes. Compared with nongated photoconductors, photo-FETs can achieve lower dark currents by electrostatically compensating the background doping via the back gate. This can ultimately lead to a higher signal-to-noise ratio. Importantly, photo-FETs based on the 2D channel materials can achieve lower dark currents than photo-FETs based on bulk materials at the same gate bias, since the depletion region (i.e., region for which band is bent) can extend through the entire thickness of the atomically thin 2D channel.

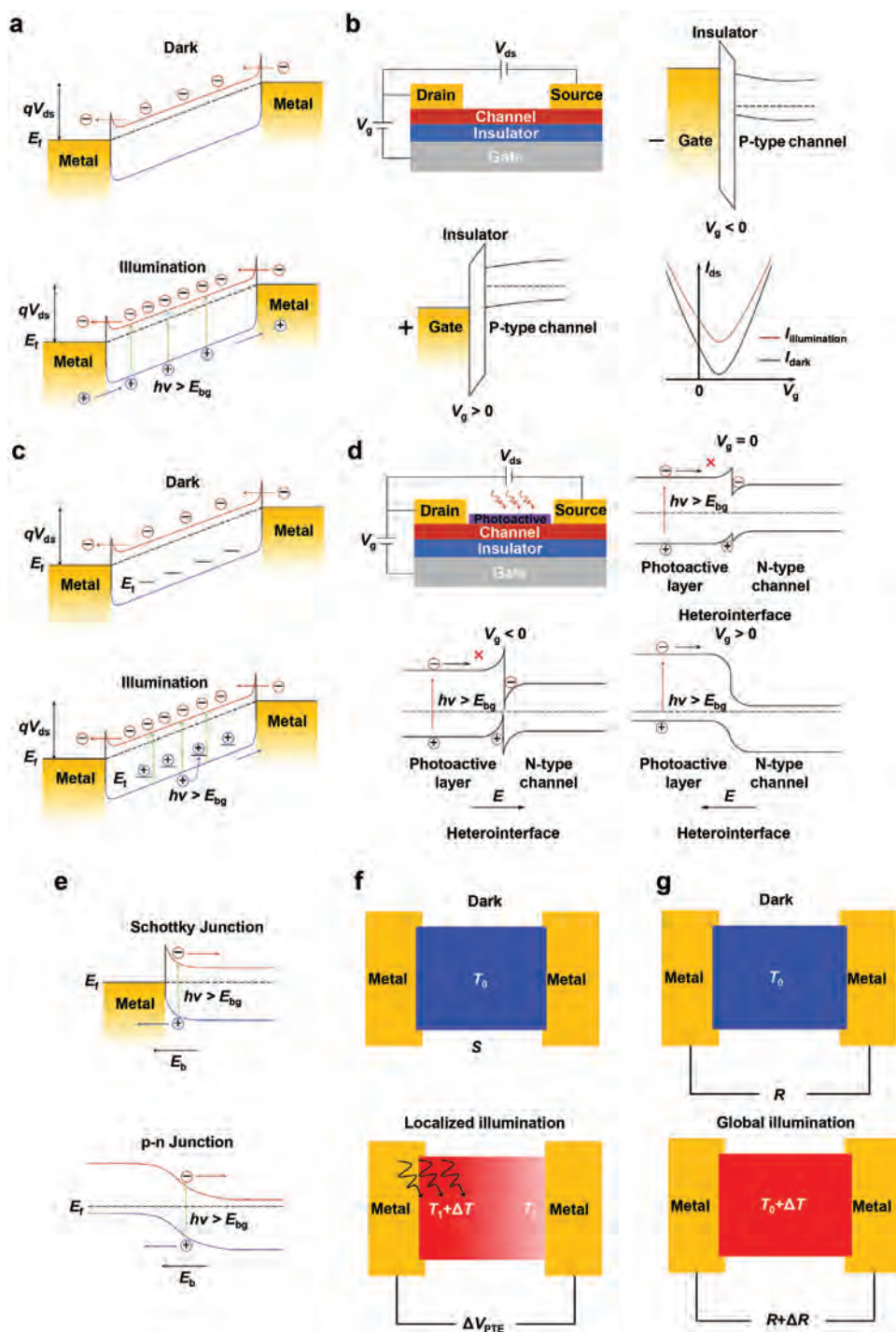


Figure 3. Schematic of the detection mechanisms of IR photodetectors. $h\nu$, E_{bg} , and E_f are the energy of incident photons, the bandgap of semiconductors, and the Fermi level of semiconductors, respectively. a) Schematic of the mechanism of PCE. Under dark conditions (upper panel), a semiconductor channel contacted by two metal electrodes produces a dark current I_{dark} at a bias voltage of V_{ds} . Under illumination (bottom panel), the extra carriers excited by incident photons lead to a large photocurrent I_{light} at a bias voltage of V_{ds} . b) Schematic of a back-gated photodetector (upper left-hand panel), band diagrams across the gate/insulator/channel of the photodetector in the dark at a negative gate bias (upper right-hand panel) and at a positive gate bias (bottom left-hand panel), and the source–drain current versus gate bias for the photodetector under illumination and in the dark (bottom right-hand panel). c) Schematic of the mechanism of PGE. Under dark conditions (upper panel), a dark current I_{dark} is produced in a semiconductor channel at a bias voltage of V_{ds} . Under illumination (bottom panel), the photoexcited holes in the semiconductor are trapped at trap states E_t and thus residual positive charges will attract more electrons from electrodes at a bias voltage of V_{ds} , resulting in a photoconductive gain. d) Schematic of a back-gated photodetector covered by a photoactive layer (upper left-hand panel), band diagrams across the photoactive layer/channel of the photodetector under illumination at a zero gate bias (upper right-hand panel), at a reverse gate bias (bottom left-hand panel), and at a forward

Photoconductors can have a photoconductive gain (G) greater than unity. Photoconductive gain can be understood as follows. Considering that electron mobility is much greater than hole mobility in most semiconductors, photoexcited electrons can drift to electrodes much faster than photoexcited holes under an external electric field. To maintain charge neutrality, electrons may recirculate through the channel many times until they recombine with holes extracted into electrodes, leading to a larger measured photocurrent. The photoconductive gain thus depends on the ratio of the photogenerated carrier lifetime ($\tau_{\text{photocarriers}}$) to the transit time of electrons (τ_{transit}), i.e., $G = \tau_{\text{photocarriers}}/\tau_{\text{transit}}$. To achieve a high photoconductive gain, either the lifetime of photogenerated carriers should be long or the transit time of electrons should be short. However, the longer lifetime of photocarriers means a slower recombination process, which will affect the response speed of the photodetectors. Hence, it is necessary to manage a trade-off between gain and response speed.

4.1.2. PGE

In phototransistors, the photogating effect may help improve the detector performance. The photogating process is described in Figure 3c, the photoexcited carriers are separated by an applied bias (V_{ds}) under illumination. If the trap states (E_t) in the channel capture one type of carrier such as holes, then these states with positive charges can act as a local gate, which will effectively modulate the conductivity of the channel by electrostatic interactions. The photogating effect is particularly important in low-dimensional nanomaterials, including 0D QDs, 1D nanowires, and 2D materials, as these have inherently large surface-area-to-volume ratios, meaning that there can be more surface defect states to trap carriers.^[94] In addition, as screening effects are low in these materials, the modulation ability of the local gate is large.^[95]

The impact of the photogating effect can also be maximized by holding the phototransistor at a particular gate bias, usually achieved using a separate back gate. As the gain is related to the slope of $I_{\text{ds}}-V_{\text{g}}$ (i.e., transconductance) and a maximum responsivity is achieved in the region where the transconductance is highest, which means a small photogating effect superimposed on top of the back gate has a large influence on the magnitude of the current change.

Besides the traps within the channel, the photogating effect can also be induced by an extra photoactive layer. As shown in Figure 3d, a photoactive layer, also called a sensitized layer or a sensitizer, can lie on the conducting channel so as to absorb incident photons, and the bottom channel is used to transport the photoexcited carriers into the

source–drain electrodes. Commonly, the photoactive layers are made of QDs, thus we take a gated photoconductor based on type-II heterostructure consisting of QD-based photoactive layer/n-type channel as an example to illustrate this type of photogating effect. With these structures, under the right conditions, one of the photoexcited carriers (e.g., electrons) from the QDs is injected into the channel and the other remains trapped in the QDs (e.g., holes). This creates a local gating effect that can considerably improve the gain of detectors, especially in low light conditions.^[4] The charge transfer dynamics at the heterointerface and the traps within the QD layer have a significant influence on this effect and are topics of current research.^[72,78] This approach circumvents the mobility limitations of QDs and hence received a lot of attention.^[71,94,96]

4.1.3. PVE

In the photovoltaic effect, photoexcited electron–hole pairs are separated toward opposite polarity contacts by an internal mechanism, commonly p–n or Schottky junctions as shown in Figure 3e, or heterocontacts with asymmetric band offsets. Photodetectors based on the photovoltaic effect are known as photodiodes. For 2D materials, the photovoltaic effect can be readily realized via the construction of heterojunctions based on opposite-doped 2D semiconductors or by combining 2D semiconductors with metals. For example, p-type bP and n-type MoS₂ can be stacked vertically to achieve a NIR p–n junction photodetector,^[15] and a vertical Schottky junction formed in Au/MoS₂/ITO layers has been employed in NIR photodetectors.^[97] Photodiodes exhibit a rectifying current–voltage behavior, which features a small and almost bias-independent reverse current and a forward current that increases exponentially with bias. Signals from photovoltaic devices are usually measured as an open-circuit voltage, as a short-circuit current, or as a current under reverse bias. When photodiodes are reverse biased (e.g., the applied electric field across the device enhances the built-in electric field), the photoexcited carriers can be separated faster and more efficiently. In general, photodiodes cannot possess greater than unity gain, a clear distinction from devices based on the photoconductive or photogating effects. However, if the reverse bias is large enough to accelerate the photoexcited carriers and enable the initiation of impact ionization, free carriers will be multiplied and thereby enabling high gain for photodiodes. The avalanche photodiode (APD) is a typical example based on this effect and is suitable for applications requiring high detection precision, such as weak light detection and single-photon detection.

gate bias (bottom right-hand panel). e) Schematic of the mechanism of PVE. Under illumination, a Schottky junction (upper panel) and a p–n junction (bottom panel) hold a built-in electric field E_b , which can separate photoexcited carriers and thus produces a photocurrent I_{light} at zero bias. f) Schematic of the Seebeck effect. Under localized illumination, incident photons are absorbed at one side of the semiconducting material and converted into local heat, and a device composed of this material with a Seebeck coefficient S produces a temperature difference ΔT and thus outputs a voltage difference ΔV_{PTE} at the metal electrodes. g) Schematic of the mechanism of PBE. Under dark conditions, a device composed of a temperature-sensitive material exhibits a temperature T_0 and a resistance R (upper panel). Under global illumination, the device in panel (e) obtains an increased temperature of ΔT and thus a resistance change of ΔR (bottom panel).

4.1.4. PTE

The photothermoelectric effect can be utilized in cases where a temperature gradient (ΔT) or a Seebeck coefficient gradient is formed across a device. The basic Seebeck effect is shown in Figure 3f, the photons are absorbed and converted into heat by one side of the semiconducting material, which results in a temperature difference (ΔT) between the two ends of the semiconductor channel. The temperature difference will drive a directed diffusion of carriers and build a photothermoelectric voltage across the channel. This voltage can be described as $V_{\text{PTE}} = S\Delta T$, where S is the Seebeck coefficient of the semiconductor. However, in terms of 2D material-based photodetector, it is impractical to only locally illuminate one side of the photoactive channel to induce an asymmetric carrier temperature gradient. On the other hand, to obtain a net current via the thermoelectric effect, the local gating or dissimilar contact metals are applied to induce asymmetric Seebeck coefficient gradients in channel materials.^[98–101] Seebeck coefficient is related to the electrical conductivity of the materials, which can be described by the Mott relation.^[102] Both the local gating and the dissimilar metal induced-doping can alter the electrical conductivity across the different parts of the channel materials, thus resulting in asymmetric Seebeck coefficient gradients. Moreover, the metal electrodes can serve as heat sinks, which helps create a temperature gradient in channel materials. In addition, through specific design, the substrate with high optical absorption can be used to heat one side of the channel material to generate a voltage output.^[103] Recently, the burgeoning development of the plasmon-assisted scheme offers a playground for further exploring PTE in 2D materials. A typical example is that only one side of the channel material is patterned to induce the plasmonic excitation, in that case, even under a uniform illumination, a significant temperature difference between two ends of the channel material will be observed, resulting in a considerable photothermoelectric response.^[104]

4.1.5. PBE

The photobolometric effect is based on the resistance change (ΔR) of the conductive channel induced by the heating of the active material upon absorption of the incident light, as shown in Figure 3g. The resistance change in the PBE is proportional to the temperature coefficient of resistance ($\text{TCR} = dR/RdT$) and the temperature increase (ΔT) induced by heat. Photodetectors based on the PBE are also called bolometers. The commercially available bolometers are mainly built on vanadium oxide (VO_x) and amorphous silicon (a-Si) (VO_x possesses a high temperature coefficient of $\approx 4\% \text{ K}^{-1}$,^[105] while the temperature coefficient of a-Si usually depends on its processing history and is an order of magnitude smaller than VO_x ^[106]). It is also worth mentioning that some bolometers are held at a temperature very close to a particularly steep TCR region. Note that the photocurrent generation mechanisms of the PBE and PTE are entirely different despite them both depending on the heating of the active material. For the PBE, photocurrent cannot be observed without applying an external bias voltage, while for PTE the photocurrent generation does not rely on external bias,

which is similar to the photovoltaic effect. Owing to the wavelength-independent property of the thermal effect, bolometers operating at wavelengths varying from MWIR to THz have been widely used in applications that require broadband operation, such as astronomy and Fourier-transform infrared (FTIR) spectroscopy. The PBE can also be utilized in 2D material-based IR photodetectors to achieve broadband spectral response beyond the limitation of the bandgap of the material being used. For example, bolometers based on SnSe thin films with a high TCR of $\approx 4.4\% \text{ K}^{-1}$ are capable of realizing a sub-bandgap response with a responsivity of 0.16 A W^{-1} at a wavelength of $10.6 \mu\text{m}$.^[107]

4.1.6. Short Discussion on Detection Mechanisms

It should be noted that the photocurrent generation in a photodetector is commonly a result of the combination of multiple detection mechanisms. For example, the photobolometric effect is a widespread phenomenon in various types of semiconductor-based photodetectors, as the absorption of light will heat the semiconductor through converting the photon energy into lattice vibrations, inevitably contributing to the photocurrent through the above mechanism. For photodetectors that are designed to work by nonthermal effects, including photoconductive effect and photovoltaic effect, a dominant thermal effect is undesired, as the thermal effect will normally slow the response speed of photodetectors by a few orders of magnitude, from submicrosecond (μs) for nonthermal effects to approximately millisecond (ms) for thermal effects. Photocurrent induced by thermal effects is often likely to be mistakenly attributed to nonthermal effects. It should be expected that the impact of the thermal effects is treated carefully when attempting to clarify the generation mechanism of photocurrent. Based on the fact that the response speed between the thermal and nonthermal effects are quite different, a feasible approach to distinguish these two types of effect in experiments is to compare the speed characteristics of the photoreponse by varying the modulation frequency. In this review, we only introduce the experimental demonstration of IR photodetectors based on nonthermal effects including PCE, PGE, and PVE, while photodetector based exclusively on the thermal effects including PTE and PBE will not be discussed further.

4.2. Figures-of-Merit of IR Photodetectors

4.2.1. Responsivity (R)

The responsivity of photodetectors is defined as the ratio of photocurrent (I_p) or photovoltage (V_p) to the incident light power, expressed by $R_I = I_p/P$ or $R_V = V_p/P$, where R_I , R_V , and P are the current responsivity, voltage responsivity, and the illumination power on the active area of detectors, respectively. Except for photovoltaic photodetectors that output an open-circuit voltage under illumination, the majority of photodetectors are characterized using the current responsivity. The current responsivity can also be described by $R_I = N_C e \lambda / N_I h c$, where N_C is the number of carriers in the photocurrent, e is the element charge, λ is the wavelength of the incident light, N_I is the

number of incident photons hitting the photodetectors, h is the Planck constant, and c is the speed of light in vacuum. This formula indicates that the responsivity increases with the wavelength of incident light (for a fixed collection efficiency N_C/N_I). This trend is valid until the wavelength of the incident light approaches the cut-off wavelength (corresponding to the optical bandgap of the absorbing materials), at which point N_C/N_I is dramatically reduced due to the lower absorption coefficient of the absorbing materials at its cut-off wavelength. This consequently reduces the responsivity and dictates the lower end of the detectable wavelength range for a given material. For commercially available IR photodetectors, their response wavelength ranges are typically limited to 1.7 μm for Ge and lattice-matched $\text{In}_x\text{Ga}_{1-x}\text{As}$, 5 μm for InSb, and 14 μm for $\text{Hg}_x\text{Cd}_{1-x}\text{Te}$.

4.2.2. External Quantum Efficiency (EQE)

External quantum efficiency is the ratio of the number of the carriers contributing to photocurrent to the number of incident photons hitting the photodetector. As discussed in Section 4.2.1, the EQE plays an important role in the responsivity, expressed by $\text{EQE} = N_C/N_I = Rhc/e\lambda$. It should be noted that not all incident photons can be absorbed because of imperfect light trapping. The number of absorbed photons can be expressed as $N_A = \eta N_I = N_I(1 - R - T)$, where η is the absorption, R is the reflection, and T is the transmission. Similarly, we define the IQE as the ratio of the number of carriers contributing to photocurrent (N_C) to the number of photons absorbed by the photodetectors (N_A), expressed by $\text{IQE} = N_C/N_A = \text{EQE}/\eta$. The IQE is dependent on internal loss mechanisms within the detector such as recombination, parasitic absorption, and resistive losses. For example, some devices suffer from poor IQE at shorter wavelengths due to parasitic absorption in a front cladding layer. Most of the commercial IR photodetectors have a high IQE across a wide spectral range, for example, the IQE is larger than 90% in the 1–14 μm range in $\text{Hg}_x\text{Cd}_{1-x}\text{Te}$ IR photodetectors.^[108]

4.2.3. Response Time and Bandwidth

Response time (τ_r) is a crucial parameter for photodetectors intended for use in high-speed applications, such as video-rate imaging or optical communication. It can be divided into the rise time (τ_{rise}) and fall time (τ_{fall}), which are the times over which the photocurrent grows from 10% to 90% (of its peak value) and over which it declines from 90% to 10%, respectively, in response to modulated illumination (e.g., step function). One of the most effective methods to reduce response time involves narrowing the spacing between the photodetector's electrodes, which will lower the transit time of photogenerated carriers to the electrodes but simultaneously decrease the light-sensitive area of photodetectors. The response times of commercially available IR photodetectors typically range from tens to hundreds of nanosecond (ns), for example, ≈ 30 ns for InSb and ≈ 500 ns for HgCdTe, while graphene-based IR photodetectors can achieve a response time of ≈ 34 ns at 1550 nm.^[109] Bandwidth measurements suggest

much faster response times are possible, particularly for graphene-based detectors. The bandwidth (f_{bw}) of photodetectors is defined as the modulation frequency of the incident light at which the photocurrent reduces to 3 dB of the peak photocurrent obtained under continuous illumination. Photodetectors suitable for high bit-rate optical communication require large bandwidths (i.e., >GHz). The reported bandwidths of the graphene-based IR photodetectors are comparable with those commercially available ones such as InGaAs-based, even in some cases, the former can obtain a faster response thanks to the high carrier mobility. By considering the time and frequency response of an ideal resistor–capacitor (RC) low-pass filter (i.e., a resistor and capacitor in series) that passes low-frequency signals but attenuates high-frequency signals, the relationship between the response time and the 3 dB bandwidth can be found to be $f_{\text{bw}} = 0.35/\tau_r$. Note that this equation can only provide useful approximate values for photodetectors that respond like low-pass filters.

4.2.4. Noise

Noise is an important consideration when designing infrared photodetectors. Generally, the noise of photodetectors consists of four components, that is, thermal noise, flicker noise, shot noise, and photon noise. 1) Thermal noise, also called Johnson noise, is generated in all resistors because of the thermal agitation of the charge carriers. The thermal noise current ($I_{N, \text{thermal}}$) flowing a photodetector can be expressed by $I_{N, \text{thermal}} = (4kT\Delta f/R)^{1/2}$, where k is the Boltzmann constant, T is the temperature of the photodetector, Δf is the measurement bandwidth, and R is the resistance of the photodetector. 2) Flicker noise is inversely proportional to the frequency f and exists in all semiconductors, usually ascribed to the random trapping and detrapping of the charges. This noise is also called $1/f$ noise. The flicker noise current ($I_{N, 1/f}$) of a photodetector is given by

$$I_{N, 1/f} = \sqrt{\int_0^{\Delta f} K \frac{I^n}{f^m} df} \quad (1)$$

where K is the flicker constant related to the properties of materials, I is the current of the photodetector in the dark, and n and m are dimensionless constants close to 2 and 1, respectively. To reduce the flicker noise current, a photodetector should be operated at a sufficiently high frequency. 3) For photodiodes, shot noise comes from the random arrival rate of carriers at the junctions, but for photoconductors, it arises from the random generation–recombination rate of carriers, which is also known as generation–recombination noise (i.e., GR noise). The shot noise current ($I_{N, \text{shot}}$) in photodiodes is given by $I_{N, \text{shot}} = (2Ie\Delta f)^{1/2}$, similarly, the shot noise current in photoconductors is given by $I_{N, \text{shot}} = (4IeG\Delta f)^{1/2} = (4IeR\Delta f)^{1/2}$. Here, e is the element charge, G (R) is the carrier generation rate (recombination rate). 4) Photon noise arises from the fluctuation of background radiation falling on IR photodetectors, which is not influenced by the detectors or their associated electronics. This means that although detector-related noises could be eliminated or reduced as desired, the photon noise inevitably

exists. Hence, the ultimate performance of an IR photodetector is limited by its photon noise.

4.2.5. Noise Equivalent Power (NEP)

NEP, specified in units of W, is the ratio of the noise current (I_N) to the current responsivity (R_I), expressed as $NEP = I_N/R_I$. NEP represents the minimum illumination power that can be detected by photodetectors, so a low NEP is desirable for IR photodetectors. The noise current can be estimated by integrating the current noise power spectral density (S_f) of photodetectors measured in the dark over the measurement bandwidth Δf , which can be expressed by

$$I_N = \sqrt{\int_0^{\Delta f} S_f df} \quad (2)$$

In addition, the noise current except for photon noise can be given by the above noise formulas as follows (for the example of a photodiode)

$$I_N = \sqrt{I_{N, \text{thermal}}^2 + I_{N, 1/f}^2 + I_{N, \text{shot}}^2} = \sqrt{\frac{4kT}{R} \Delta f + \int_0^{\Delta f} K \frac{I^n}{f^m} df + 2Ie\Delta f} \quad (3)$$

Since 2D materials with the atomic thickness normally possess a small volume, which enables a large resistance R and thus a suppressed current I , IR photodetectors based on 2D materials may exhibit a lower noise than those based on bulk semiconductors.

4.2.6. Specific Detectivity (D^*)

Specific detectivity (D^*), expressed in units of $\text{cmHz}^{1/2} \text{W}^{-1}$ (Jones), is one of the most important figures-of-merit for photodetectors. It normalizes the influence of bandwidth and active area of photodetectors with different geometries for a better comparison of their performance. It can be expressed as

$$D^* = \frac{\sqrt{A\Delta f}}{NEP} = \frac{\sqrt{A\Delta f}}{I_N} R_I \quad (4)$$

where A is the active area of photodetectors. For a shot noise limited photodiode, its specific detectivity can be approximated by

$$D^* = \sqrt{\frac{A}{2Ie}} R_I \quad (5)$$

For commercially available IR photodetectors based on compound semiconductor systems, the range of specific detectivity is normally from $\approx 10^{11}$ to $\approx 10^{12}$ Jones at a low operating temperature of 77 K at the range of 1–3 μm ,^[110,111] while 2D material-based IR photodetectors have been reported to reach a similar specific detectivity at room temperature, for example, $\approx 10^{12}$ Jones at a SWIR wavelength of 2 μm for the MoS_2/HgTe quantum dot hybrid photodetector.^[4]

While the state-of-the-art photodetectors can reach a specific detectivity of 10^{12} Jones in the SWIR spectral region, it is almost impossible for them to reach such a high specific detectivity at MWIR or LWIR wavelengths. This is because the highest detectivity of most IR photodetectors is limited by the background-limited IR photodetector (i.e., BLIP, in which photon noise from the background radiation exclusively limits performance), whose specific detectivity decreases from the SWIR to LWIR due to the increased background noise. For example, at a hemispherical field of view (FOV) angle of 90° at a background temperature of 300 K, the specific detectivity curve of the BLIP with unity quantum efficiency experiences a dramatic drop from $\approx 10^{13}$ Jones at 2 μm to $\approx 4 \times 10^{10}$ Jones at 12 μm .^[108]

5. Nanophotonics for Absorption Enhancement of 2D Materials

Although the optical absorption coefficients of 2D materials are remarkably high, the light absorption is still limited by their nanometer-scale thickness. For example, the optical absorption coefficient of graphene is given by $-\ln(1 - n\pi\alpha)/nd$ (where $d = 0.335$ nm is the thickness of single-layer graphene, n is the layer number, and $\alpha = 1/137$ is the fine structure constant),^[43] which means that the absorption coefficient could be up to $7 \times 10^5 \text{ cm}^{-1}$ for single-layer graphene. However, single-layer graphene only absorbs 2.3% of incident light due to its atomic thickness.^[53,55] For TMDs, light absorption in 2D crystals is still low compared with their bulk counterparts. The light absorption in monolayer MoS_2 is about 10% at the excitonic resonance wavelengths.^[52] The light absorption of mono-, bi-, and trilayer bP is no more than 15% in the IR regime.^[56] To overcome the above-mentioned obstacle and improve the optoelectronic performance of 2D material-based IR photodetectors, many optical techniques such as the use of plasmonic enhancement,^[36,39,112] optical microcavities,^[43,44] optical cavity substrate,^[14,45] and waveguides^[3,113] have been developed. In this section, we will introduce these optical techniques and the working principles behind them.

5.1. Plasmonic Enhancement

5.1.1. Surface Plasmon Waves in Metal Nanostructures

Plasmons are the collective oscillations of electrons in metallic nanostructures that could occur upon optical excitations. These oscillations produce electromagnetic waves localized at the interface between metallic nanostructures and the surrounding dielectric. These waves are also referred to as surface plasmon waves.^[114] Usually, surface plasmons, also termed as surface plasmon polaritons (SPPs), corresponds to electromagnetic waves propagating along the flat metal–dielectric interface. Surface plasmons confined on the surface of metallic nanoparticles (NPs) are usually called localized surface plasmons (LSPs).

SPP is a kind of electromagnetic excitation coupled with the collective oscillation of conduction electrons concentrated very close to the flat metal–dielectric interface, as shown in **Figure 4a**. Through the concentration of electromagnetic field

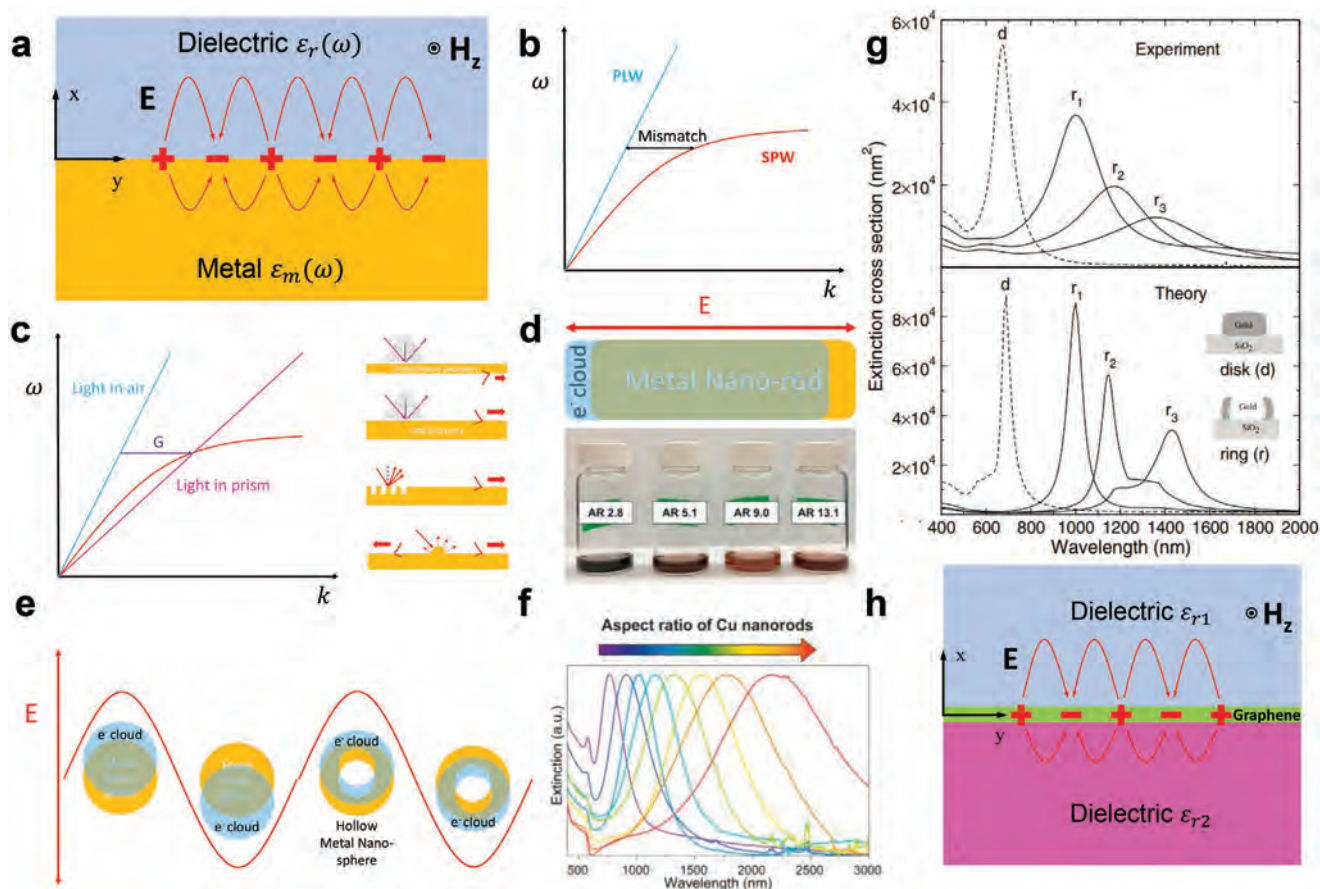


Figure 4. Surface plasmon polaritons. a) Schematic of propagating SPPs at a metal–dielectric interface. b) Dispersion relations of a propagating light wave (PLW, light-blue) in a dielectric environment and a surface plasmon wave (SPW, red), showing the momentum mismatch between them. c) Dispersion relations of light in air (light-blue), in prism (purple), and SPW (red), showing the compensation of momentum mismatch between the light in air and SPW by the prism coupling and diffraction mechanism. The top two schematics in the right panel are the Kretschmann and Otto geometries for achieving the momentum matching condition, respectively. The bottom two schematics in the right panel show light diffraction on a metallic grating and scattering on a rough metal surface, respectively. Schematic of localized surface plasmon resonance (LSPR) in d) a metal nanorod and e) a metal nanosphere (left) and a metal nanoring (right). f) Extinction spectra for Cu nanorods with different aspect ratios in water, with their LSPR tunable from 0.76 to 2.2 μm . The bottom part of panel (d) is a photograph of these Cu NRs. Reproduced with permission.^[118] Copyright 2020, American Chemical Society. g) The tunable extinction spectrum of gold nanorings with different geometrical properties. Reproduced with permission.^[120] Copyright 2003, American Physical Society. Intrinsic graphene plasmon. h) Schematic of the graphene plasmons excited in a dielectric–graphene–dielectric structure.

energy, the intensity of the SPP field could be enhanced significantly. For example, the intensity of the electric field on the surface could be enhanced by more than two orders of magnitude compared with the incident electric field in the case of a perfect coupler on a silver surface.^[115] However, due to the wavevector mismatch between the propagating light wave in the adjacent dielectric medium, k_{PLW} , and the surface plasmon wave in the metal surface, k_{SPW} , as shown in Figure 4b, special experimental arrangements is needed to excite SPPs by light.^[116] One method is to use the total internal reflection geometries including Kretschmann and Otto configurations, as shown in Figure 4c. In the Kretschmann configuration, a prism made up of optically dense medium is used to increase the wavevector of incident light to couple with SPPs in the metal surface, as shown in the first line in the right panel of Figure 4c. However, this configuration is only helpful to excite SPPs of thin metal films since the limitation of the tunneling distance. For thick metal films or even surfaces of bulk metals, the Otto configuration can be

used to excite SPPs, as shown in the second line in the right panel of Figure 4c. Another frequently used method utilizes the diffraction effects. The wavevector of the diffracted light could be modified by designing special patterns of the diffracting elements. For example, diffraction gratings can be employed to generate diffracted light appropriate for coupling to SPPs, as shown in the third line in the right panel of Figure 4c. Both air–metal and substrate–metal SPP modes could be excited by this diffraction configuration through proper design of grating profiles. In addition, the SPPs excitation conditions can be realized on a randomly rough surface, as shown in the bottom line in the right panel of Figure 4c. However, the SPPs coupling efficiency is quite low on rough surfaces due to the generation of diffracted light with random wavevectors. Since the electric field intensity of incident light can be enhanced significantly by coupling it into SPPs that propagate along the metal surface, we can use SPPs to enhance the light absorption by 2D materials placed in proximity to the surface. However, at low frequencies

(i.e., longer wavelengths), the metal behaves more like an ideal metal and SPPs are less confined to the surface. This can lead to reduced absorption enhancement.

Compared with SPPs, the excitation of LSPs require no wavevector matching as they are resonant excitation induced by light absorption of specific wavelengths in the metallic nanostructures, as shown in Figure 4d,e.^[117] The resonances associated with the oscillations of electrons in nanoparticles are often called localized surface plasmon resonances (LSPRs). Since the energy of incident light with specific wavelength is confined to the surface of the metallic nanoparticles, the electric field can be enhanced significantly. The LSPRs are excited when the frequency of incident light matches the resonant frequency of the particle. The resonant wavelength range of LSPRs can be adjusted by changing the material properties and geometric parameters of the nanoparticles. Figure 4f illustrates the extinction spectrum of LSPRs occurring in colloidal copper nanorods prepared by the heterometallic seed-mediated synthesis method.^[118] By varying the size and shape of silver nanoparticles, the LSPR wavelength can be tuned to beyond 6 μm .^[119] The bottom panel of Figure 4d shows a photograph of these prepared Cu NRs. Figure 4g shows the tunable extinction spectrum of the gold nanorings.^[120] Through the localized electromagnetic field enhancement by LSPRs, the overall light absorption of 2D materials placed in close proximity to the metal nanoparticles can be significantly improved. Based on this effect, LSPRs can provide spectral selectivity for 2D material-based IR photodetectors.

Metal contacts in 2D material-based optoelectronic devices can be designed to support plasmonic resonances to improve performance. This can be achieved in two ways: 1) the direct generation of electron–hole pairs in adjacent 2D materials induced by the highly enhanced electromagnetic fields associated with the metal plasmons; 2) the “hot electrons” (high-energy electrons excited through the decay of surface plasmons) can enter the conduction band of 2D materials and thus contribute to the photoresponse.^[120–123]

5.1.2. Intrinsic Graphene Plasmons

As discussed, surface plasmon modes can be excited by light in metallic nanostructures. In addition, as a semimetal, graphene can also support surface plasmons, as shown in Figure 4h.^[69,70,112,124] This property can be favorable for tailoring the responsivity spectra of photodetectors. Graphene supports plasmons in the MWIR-to-THz regimes, meaning that optoelectronic devices can also operate in this spectral range. Because of the high carrier mobility of graphene, its plasmon waves are subject to pronounced spatial confinement, which endows graphene with strong light absorption. Furthermore, the spectral response of graphene is tunable through electrostatic gating in the MWIR to THz regime. To excite graphene plasmon, special geometries have to be employed to match the wavevector of plasmons with electromagnetic fields.^[125] The most widely used method is by patterning the graphene into periodic nanostructures.^[126] Such a method is easy to implement with modern nanofabrication technologies. In addition, the light scattered by individual graphene nanostructures can excite the plasmons in

the nearby graphene nanostructures.^[127] Metal grating can also be used to excite the graphene plasmon.^[128]

5.2. Optical Microcavities

Optical microcavities can confine the incident light into small volumes by resonant light recirculation inside them. The optical absorption in 2D materials placed at the plane of field enhancement inside the microcavities can thus be improved.^[137,129] The two figures-of-merit often used to evaluate the quality of optical microcavities are the cavity quality factor (Q) and the microcavity mode volume (V_m). The former is proportional to the confinement time and usually measured in the unit of optical period and the latter describes the light confinement in space. For ideal microcavities, optical fields can be confined without any losses, leading to high-quality factors. The optical microcavities can be divided into three types. 1) The Fabry–Pérot microcavity as shown in Figure 5a. The top and bottom surfaces are Bragg mirrors consisting of layers of alternating materials with appropriate thickness. The spectral response of the middle 2D materials can be tuned by adjusting the resonance property of the cavity. 2) The whispering gallery microcavity is as shown in Figure 5b. Such cavity makes use of standing waves to confine the electromagnetic field. Whispering gallery microcavities can be constructed based on spheres,^[130] disks or self-suspended disks,^[131,132] and rings.^[133,134] 3) The 2D photonic crystal microcavities is shown in Figure 5c. The energy of the optical field can be confined in the planar defect region in the photonic crystal.

Optical cavity substrates have also been employed to enhance the light absorption in 2D materials by transferring them onto the substrate, resulting in performance improvement of 2D material-based IR photodetectors.^[14,15,45] The optical cavity substrates normally consist of dielectric spacing materials on back-reflectors, as shown in Figure 5d. A typical procedure for fabricating optical cavity substrates involves the evaporation of noble metal reflectors on the substrates, followed by the atomic deposition of dielectric materials. The dielectric materials usually have no optical absorption, serving as optical spacers for the cavities. By choosing the proper thickness of these dielectric materials, absorption enhancement can be realized at specific wavelengths. Noble metals are usually selected to construct the back-reflector, such as gold and silver whose reflectivity is very close to unity, especially in the IR region.

By integrating with these optical microcavities or optical cavity substrates, the intensity of the electromagnetic field near the 2D materials and therefore the optical absorption can be enhanced significantly. This leads to a considerable performance improvement of the 2D material-based photodetectors.

5.3. Optical Waveguides

Another common method to improve the light absorption of 2D material-based IR photodetectors is to integrate 2D materials with optical waveguides.^[135] By doing so, light absorption by the 2D materials, which is usually limited by the atomic thickness of the 2D materials for normally incident light, can

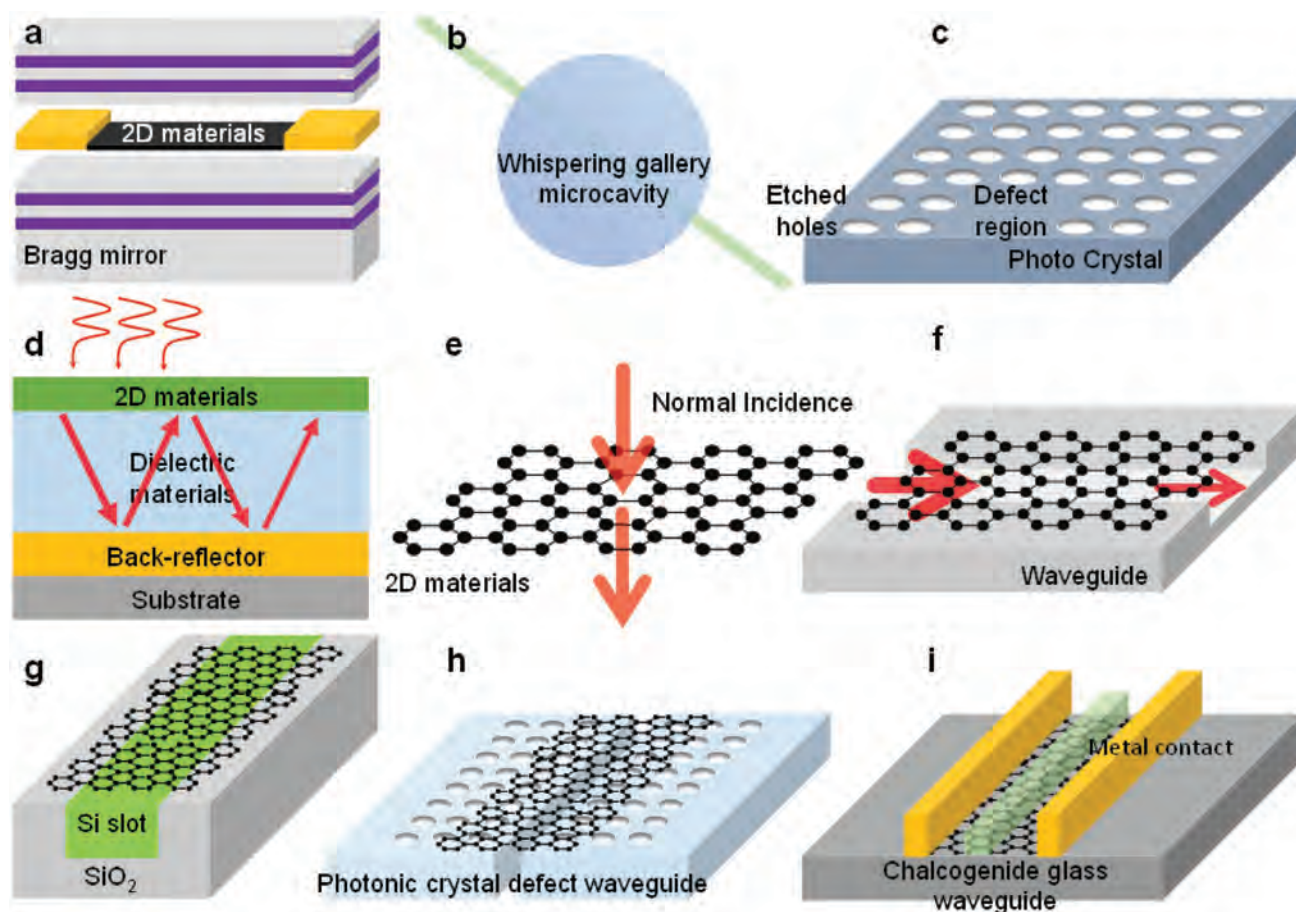


Figure 5. Optical microcavities and waveguides for enhancing the absorption of 2D materials. a) Schematic of a Fabry–Pérot (F–P) microcavity. The 2D material is located between the top and bottom Bragg mirrors forming an F–P cavity. b) Schematic of a whispering gallery microcavity based on a dielectric sphere. c) Schematic of a 2D photonic crystal microcavity. The optical field is confined in the defect region. d) Schematic of an optical waveguide for enhancing the light absorption of a 2D material on top. e) Schematic of light normally incident on a 2D material sheet, leading to a limited absorption due to the atomic thickness of the material. Schematics of coupling a 2D material with f) a groove gap waveguide, g) a Si slot waveguide, h) a photonic crystal defect waveguide, and i) a chalcogenide glass waveguide.

be enhanced by increasing the interaction distance with evanescent wave propagating along the waveguides, as shown in Figure 5e,f. After introducing the electromagnetic field into the waveguide channel, the 2D material is usually spatially overlapped with the evanescent field corresponding to the optical mode of the waveguide, thus the light absorption coefficient (i.e., absorption per unit length) is lower than normal incidence. However, the interaction distance between 2D materials and the light field can be made long, making the overall light absorption strong.

To enhance the light absorption in 2D materials, three waveguide types have been mainly used. 1) The traditional Si slot waveguide, as shown in Figure 5g. For this structure, an optical fiber is usually used to couple the incident light into the slot area. 2) The photonic crystal (PhC) defect waveguide, as depicted in Figure 5h. The photonic crystal defect waveguide allows for a better photothermoelectrical conversion compared with the traditional slot waveguide design for the larger gating area enables a full exploitation of the temperature profile in graphene.^[136] 3) The chalcogenide glass (ChG) waveguide, as demonstrated in Figure 5i.^[137] The chalcogenide glass is a

multifunctional material that can be directly deposited and patterned on a wide variety of 2D materials at room temperature and serves as a wave-guiding medium. The fabrication method for the ChG waveguide allows the crystalline orientation and the geometry of the beneath ultrathin 2D materials to be considered during fabrication. As an additional benefit, the ChG can serve as a passivation layer to 2D crystals, improving the stability of 2D material-based IR photodetectors.

6. IR Photoconductors Based on 2D Materials

Owing to the availability of photoconductive gain and ease of fabrication, the initial trials of 2D material-based IR photodetectors have mostly used the photoconductor configuration. The photoconductor is generally constructed using a typical contact/2D material absorbers/contact configuration, sometimes with a back-gate architecture in which the conductivity of the 2D material channel on the insulator/gate substrate can be electrostatically controlled. However, photoconductors typically exhibit a large noise current because of the applied external

electric field, which is necessary to drive the photoexcited carriers in the photoconductors without the built-in fields of junctions. Though the back-gate architecture of photoconductors can effectively suppress the noise current, it would not be practical for use in an array. Currently, a wide range of 2D materials have been explored as absorbers in IR photoconductors. In this section, we summarize the recent progress in 2D material-based IR photoconductors based on different material categories. For the reader's reference, key figures-of-merit of some 2D material-based IR photodetectors are listed in **Table 1**.

6.1. Graphene-Based IR Photodetectors

As one of the most widely explored 2D materials, graphene exhibits a variety of remarkable electronic and optical properties, such as the high carrier mobility of $\approx 10^6 \text{ cm}^2 \text{ V}^{-2} \text{ s}^{-1}$ observed in suspended samples,^[67] as well as the strong light absorption covering ultraviolet to terahertz regimes for single-layer graphene. To date, various types of graphene-based IR photoconductors have been demonstrated,^[138] with a particular emphasis being those for high-frequency applications.^[139] These detectors were typically constructed in a simple gate–source–drain transistor architecture, in which large-area single- or few-layer graphene sheets would act as the conducting channel in contact with two metal electrodes for carrier extraction. The channel conductivity of the graphene was modulated by applying gate-biases through the bottom gate. The speed of the photodetectors can be improved by adjusting the channel resistance, which determines the resistor–capacitor time constant of the detectors. As shown in **Figure 6a**, under $1.55 \mu\text{m}$ illumination with optical modulation frequencies up to 40 GHz, the graphene-based photodetector reported by Xia et al. did not show any degradation in photoresponsivity, at a gate bias of 80 V.^[32] The authors found that the observed fast IR response was a direct result of the high carrier mobility in graphene. They also argued that the RC circuits limited the ultimate bandwidth in their photodetector, with the assumption of the capacitance of the $\approx 3 \mu\text{m}^2$ graphene was 5 fF, the RC limited bandwidth would be 640 GHz. In addition, under steady (unmodulated) illumination, a maximum responsivity of 0.5 mA W^{-1} was achieved at a gate bias of 80 V, as presented in **Figure 6b**. The estimated internal quantum efficiency was around 6–16% in its operating region. Note that unlike in conventional metal–semiconductor–metal photodetectors in which a large external bias was necessary for high-speed operation, all the measurements in this work were implemented at zero or close to zero source–drain bias, which ensured a low dark current. Following this work, Mueller et al. reported a similar metal–graphene–metal IR photoconductor, which exhibits also a broad 3 dB bandwidth of 16 GHz at a wavelength of $1.55 \mu\text{m}$.^[140] More importantly, as compared to the aforementioned graphene-based photoconductor, this IR photodetector achieved a significant photoresponsivity improvement up to ≈ 15 times. The enhancement in performance was attributed to the novel contacting scheme, in which two asymmetrically interdigitated electrodes were employed at the terminals of the graphene channel, as shown in **Figure 6c**. This resulted in the

broken mirror symmetry of the internal electric field profile in the graphene channel, which permits more efficient extraction of photogenerated carriers. It should be noted however that the low light absorption and short photogenerated carrier lifetime are detrimental to the performance of IR photodetectors based on pristine graphene. Various materials engineering methods have thus been used to process graphene to obtain higher performance. As a typical example, the reduced graphene oxide (RGO) and graphene nanoribbons (GNRs) were first prepared by Chitara et al. to construct an IR photoconductor, which exhibited improved photodetection performance compared with photodetectors based on few-layer pristine graphene.^[141] More specifically, a responsivity of 4 mA W^{-1} was acquired under $1.55 \mu\text{m}$ SWIR illumination for the RGO-based photodetector, while a responsivity as high as 1 A W^{-1} (corresponding to an EQE of 80%), was achieved for the GNR-based photodetector. The significant increase of responsivity for the GNR-based photodetector was due to the stronger light absorption as a result of the nonzero bandgap of the GNRs, while the RGO has zero bandgap.

In addition to material engineering, surface modification of materials is also an effective approach to enhance the performance of 2D material-based photodetectors. For example, Chang et al. developed a high-responsivity IR photoconductor by controlling the oxygen defects and atomic structure in few-layer reduced graphene oxide (FRGO).^[142] The authors found that by varying the duration of the thermal reduction of FRGO, the number of defects was able to be tuned, making it possible to improve the transfer properties of the FRGO-based photodetector. As shown in **Figure 6d**, the photodetector with FRGO undergone 260 min of reduction treatment showed a responsivity of 0.7 A W^{-1} at a bias voltage of 19 V under NIR illumination at a wavelength of $0.895 \mu\text{m}$. This responsivity was much higher than the responsivity of $\approx 0.01 \text{ A W}^{-1}$ observed in the photodetector with FRGO undergone 20 min of reduction treatment.

Beyond the NIR and SWIR regime, surface engineering of graphene has also been employed for the realization of photodetection of longer IR wavelengths. For example, Du et al. demonstrated an MWIR photoconductor composed of multilayer graphene and its surface fluorine-functionalized derivative.^[143] As shown in **Figure 6e**, compared with the photodetector based on pristine graphene, the fluorine–graphene (FG/Gr) photodetector achieved a considerable room-temperature specific detectivity that is higher than $\approx 10^9$ Jones across a broad IR wavelength range from 1 to $4 \mu\text{m}$. The reason for the improved performance was that the sp^2 and sp^3 nanodomains induced by the rehybridization of carbon with fluorine not only enhanced the light absorption of graphene but also acted as trap states to enhance gain. Zhang et al. reported an LWIR photoconductor consisting of monolayer graphene with defect mid-gap states, which were introduced by forming the quantum dot-like array structure via the surface etching method, as shown in **Figure 6f**.^[144] Note that these defect states strengthened the light–graphene interaction and induced trapping of charge carriers, leading to a photoconductive gain. Benefiting from these effects, a photoresponsivity of 0.4 A W^{-1} was acquired at a source–drain bias voltage of 20 mV bias at a wavelength of $9.9 \mu\text{m}$.

Table 1. Figures-of-merit of 2D material-based IR photodetectors.

Materials	Wavelength [μm]	R (A W^{-1})	EQE [%]	D^* [Jones]	Response speed	Type	Refs.
Graphene	1.55	0.5×10^{-3}			40 GHz	PC	[32]
Graphene	0.514–1.55	6.1×10^{-3}			16 GHz	PC	[140]
GNRs ^{a)}	1.55	1	80		2 s, 26 s	PC	[141]
FRGO ^{b)}	0.895	0.7	97		2 s, 20 s	PC	[142]
Fluorographene	0.255–4.3	$\approx 10^4$ –10		$\approx 10^{11}$ – 10^9	≈ 100 ms	PC	[143]
QD ^{c)} -like graphene	0.532–9.9	≈ 1.25 –0.4				PC	[144]
Graphene/SiO ₂ /graphene	1.3–3.2	4–1.1				PC	[12]
3D graphene	10.6–119	0.23		2.8×10^{10}	256 ns, 220 ns	PC	[145]
Twisted bilayer graphene	5–12	2.6×10^{-2}				PC	[146]
Graphene/MoS ₂	≈ 0.4 –1.44	1.26		4.2×10^{10}		PD	[175]
MoS ₂ /graphene/WSe ₂	0.4–2.4	0.1		10^9	53.6 μs , 30.3 μs	PD	[176]
Graphene/MoTe ₂ /graphene	1.064	0.11	12.9		24 μs , 46 μs	PD	[177]
MoS ₂ /graphene/MoS ₂	0.532–1.6	≈ 1.1 – 10^{-5}		2×10^7		PD	[178]
MoTe ₂ /graphene/SnS ₂	0.4–1.6	$\approx 2.64 \times 10^3$	$\approx 10^4$	1.1×10^{13}	24.1 ms, 28.6 ms	PD	[179]
Graphene/PbS QDs	0.6–1.4	5×10^5	25		10 ms	PC	[71]
Graphene/Si QDs	0.375–3.9	$\approx 10^8$	5×10^9	10^{13}		PC	[27]
Graphene/TiO ₂ /PbSe QDs	1	0.13		5.7×10^{12}	750 ns	PC	[96]
Graphene/TiO ₂ NPs ^{d)}	4.5–10	$\approx 10^2$		7×10^8	1.2 ms, 2.6 ms	PC	[164]
Graphene/Bi ₂ Te ₃	0.4–1.6	10			8.7 ms	PC	[170]
Graphene/CNTs ^{e)}	0.4–1.55	100	25		100 μs	PC	[165]
Graphene/HgTe NCs ^{f)}	1.55	6×10^{-3}		$\approx 10^9$	9 μs , 7 μs	PD	[184]
RGO/ZnO/Ge QDs	1.4	≈ 9.7		6.42×10^{11}	40 μs , 90 μs	PD	[185]
Graphene/InAs NWs ^{g)}	1	0.5				PD	[186]
Graphene/Si NWs	10.6	9×10^{-3}			70 ms	PD	[187]
MoTe ₂	1.06	2.4×10^{-2}		1.3×10^9	1.6 ms, 1.3 ms	PC	[148]
ReSe ₂	0.52–1.064	$\approx 10^2$			30 ms, 64 ms	PC	[149]
PtSe ₂	0.632–10	4.5		$\approx 7 \times 10^8$	1.1 ms, 1.2 ms	PC	[85]
PdSe ₂	0.532–4.05	708	8.27×10^4	1.31×10^9	220 ms	PC	[150]
SnTe	0.405–3.08	3.75			0.31 s, 0.85 s	PC	[151]
GeAs	1.6	6			2.5 ms, 3.2 ms	PC	[152]
NbS ₃	0.83–10.6	2.5×10^{-2}		10^8	11.6 μs	PC	[153]
TaIrTe ₄	0.532–10.6	2.5×10^{-5}		1.8×10^6	27 μs	PC	[154]
Bi ₂ O ₂ Se	1.200	≈ 65		3.0×10^9	500 GHz	PC	[19]
b ^{ph)}	3.39	82			≈ 10 kHz	PC	[158]
b-PAs ⁱ⁾	0.98–4.6	≈ 10	6.4	2.4×10^{10}	12.4 μs , 8.6 μs	PC	[81]
b-PC	2.004	2163	1.3×10^5	$\approx 10^{11}$	0.7 ns	PC	[159]
Te	0.52–3	$\approx 1.36 \times 10^3$		1.15×10^{10}	48.7 μs , 62.7 μs	PC	[160]
WS ₂ /PbS QDs	0.808	14		3.9×10^8	226 μs	PC	[171]
SnS ₂ /PbS QDs	0.3–1	$\approx 10^5$		2.2×10^{12}	160–240 ms	PC	[172]
MoS ₂ /PbS QDs	0.4–1.5	$\approx 6 \times 10^5$		5×10^{11}	0.35 s	PC	[78]
MoS ₂ /HgTe QDs	2.1	$\approx 10^4$		$\approx 10^{12}$	≈ 4 ms	PC	[4]
CdS _x Se _{1-x} /PbS QDs	0.808	0.18		1.29×10^{11}	0.47 s, 0.72 s	PC	[173]
Bi ₂ O ₂ Se/PbSe QDs	0.5–2	$\approx 10^3$			4 ms	PC	[174]
MoTe ₂ /MoS ₂	1.55					PD	[73]
PdSe ₂ /MoS ₂	0.45–10.6	42.1		8.21×10^9	74.5 ms, 93.1 ms	PD	[13]
MoTe ₂ /MoS ₂	0.8	3.7×10^{-2}	6		25 ms	PD	[33]

Table 1. Continued.

Materials	Wavelength [μm]	R (A W^{-1})	EQE [%]	D^* [Jones]	Response speed	Type	Refs.
PtSe ₂ /PtSe ₂	0.405–2.2	0.19	0.05–1.2		66 ms, 75 ms	PD	[180]
WSe ₂ /Bi ₂ Te ₃	0.375–1.55	2.7×10^{-2}	4.39		210 μs	PD	[28]
bP/MoS ₂	1.5–3.8	0.9	35	1.1×10^{10}	3.7 μs , 4 μs	PD	[14]
b-AsP ^l /MoS ₂	3–5	≈ 0.2	11.36–3.33	4.9×10^9	0.54 ms, 0.52 ms	PD	[176]
bP/MoS ₂	0.532–1.55	≈ 0.15		2.13×10^9	15 μs , 70 μs	PD	[15]
WSe ₂ /bP/MoS ₂	0.532–1.55	1.12		2.21×10^{10}		PD	[181]
bP/PdSe ₂	0.532–1.31	1.63×10^5	9.4×10^6	$\approx 10^{13}$ – 10^{11}	1.6 ms, 4.7 ms	PD	[182]
PtSe ₂ /perovskite	0.3–1.2	≈ 0.12		2.91×10^{12}	78 ns, 60 ns	PD	[188]
MoS ₂ /Si	0.35–1.1	0.3		$\approx 10^{13}$	3 μs	PD	[159]

^a)GNRs: graphene nanoribbons; ^b)FRGO: few-layer reduced graphene oxide; ^c)QDs: quantum dots; ^d)NPs: nanoparticles; ^e)CNTs: carbon nanotubes; ^f)NCs: nanocrystals; ^g)NWs: nanowires; ^h)bP: black phosphorus; ⁱ)b-PAs: black phosphorus-arsenic; ^j)b-AsP: black arsenic-phosphorus.

Liu et al. reported that by leveraging the hot-carrier effect of graphene, efficient broadband IR detection was achieved by a graphene/Si/graphene photoconductor, in which two graphene monolayers were separated by a thin interlayer of Si, with the bottom graphene layer on the SiO₂/Si substrate acted as the channel of the device.^[12] Under IR illumination, the asymmetric tunneling barrier favors photoexcited hot-electrons tunneling into the bottom graphene layer from the top graphene layer through the middle thin Si layer, resulting in the residuals of the holes on the gate so that produces a photogating effect and thus a photoconductive gain. As a result, high responsivities were observed at room temperature at different IR wavelengths, i.e., 4 A W⁻¹ at 1.3 μm , 1.9 A W⁻¹ at 2.1 μm , and 1.1 A W⁻¹ at 3.2 μm , as shown in Figure 6g.

While all of the above examples are based on planar configurations, other researchers have investigated the advantages of 3D configurations. For example, Deng et al. demonstrated an IR photoconductor based on the 3D tubular graphene field-effect transistor (GFET).^[145] Note that the tubular structure served as a resonant microcavity to enhance the optical absorption by the graphene. As compared to the typical 2D GFET photodetector, the 3D GFET photodetector exhibited higher responsivities over a wide wavelength range up to the FIR regime, with the highest room-temperature responsivity of 0.23 A W⁻¹ obtained at a wavelength of 96 μm , corresponding to a specific detectivity of 2.8×10^{10} Jones, as shown in Figure 6h. In addition to the 3D tubular graphene formed via the out-plane twist force, in-plane stacking of bilayer graphene with a small-twist-angle has been leveraged to construct IR photoconductors. In small-twist-angle graphene, a superlattice bandgap will form, which improves the IR photodetection. Recently, Deng et al. demonstrated a gated LWIR photoconductor with h-BN-encapsulated small-twist-angle bilayer graphene.^[146] Under the IR illumination for three different wavelengths (i.e., 5.0, 7.7, and 12 μm), the twisted graphene-based photodetector exhibited a responsivity, which depends strongly on the gate-voltage V_{BG} as shown in Figure 6i, with a peak responsivity of ≈ 1.2 mA W⁻¹ acquired at 5 μm at 80 K at the Dirac point, in which the gate-voltage V_{BG} is applied in such a way that the residual charge carrier density reaches a minimum.

6.2. 2D Semiconductor-Based IR Photodetectors

Besides semimetallic graphene, various TMDs have been used to fabricate IR photoconductors in recent years.^[147] For example, Huang et al. developed a 2H-type MoTe₂ IR photoconductor, which exhibits a specific detectivity of 1.3×10^9 Jones at a source–drain and back-gate voltage of 10 V at a wavelength of 1.06 μm .^[148] Materials engineering has also been employed to enhance 2D TMD-based IR photoconductors. For example, Jo et al. demonstrated a ReSe₂-based IR photoconductor in which the ReSe₂ layer doped by triphenylphosphine (PPh₃) yielded a responsivity of larger than $\approx 10^2$ A W⁻¹ across a spectral range from 0.52 to 1.064 μm .^[149] In this work, the responsivity of the photodetector was significantly improved by two methods: a triethoxysilane (APTES) treatment of the ReSe₂/SiO₂ interface to suppress the scattering of interfacial carriers, and a PPh₃-based n-doping technique to obtain a low resistance at the metal–semiconductor contacts. In addition to MoTe₂ and ReSe₂, other 2D TMDs with intrinsic narrow bandgaps have also exhibited potentials in building IR photodetectors, including those capable of photodetection at longer IR wavelengths. For example, Yu et al. developed a PtSe₂-based photoconductor that achieves an efficient LWIR detection at a wavelength of 10 μm , achieving a specific detectivity of 7×10^8 Jones at room temperature.^[85] In addition to the high specific detectivity, the photodetector using bilayer PtSe₂ also exhibited a response time of ≈ 1 ms at a bias voltage of 0.1 V at different IR wavelengths (i.e., 0.632, 1.47, and 10 μm) as shown in Figure 7a. This excellent LWIR performance observed in the PtSe₂-based photodetector was a result of the well-designed layer numbers and defects, as the bandgap of PtSe₂ was reduced with both the increased number of atomic layers and the increased concentration of defects. More recently, Liang et al. fabricated a PdSe₂-based IR photoconductor, which realized broadband response spectra ranging from visible light to MWIR due to the thickness-dependent bandgap of PdSe₂ (i.e., from 1.3 eV for the monolayer to 0 eV for the bulk).^[150] Under 1.064 μm NIR illumination, a responsivity of the PdSe₂-based photodetector as high as 708 A W⁻¹ was achieved at a bias voltage of 1 V at room temperature, which corresponds to a considerable

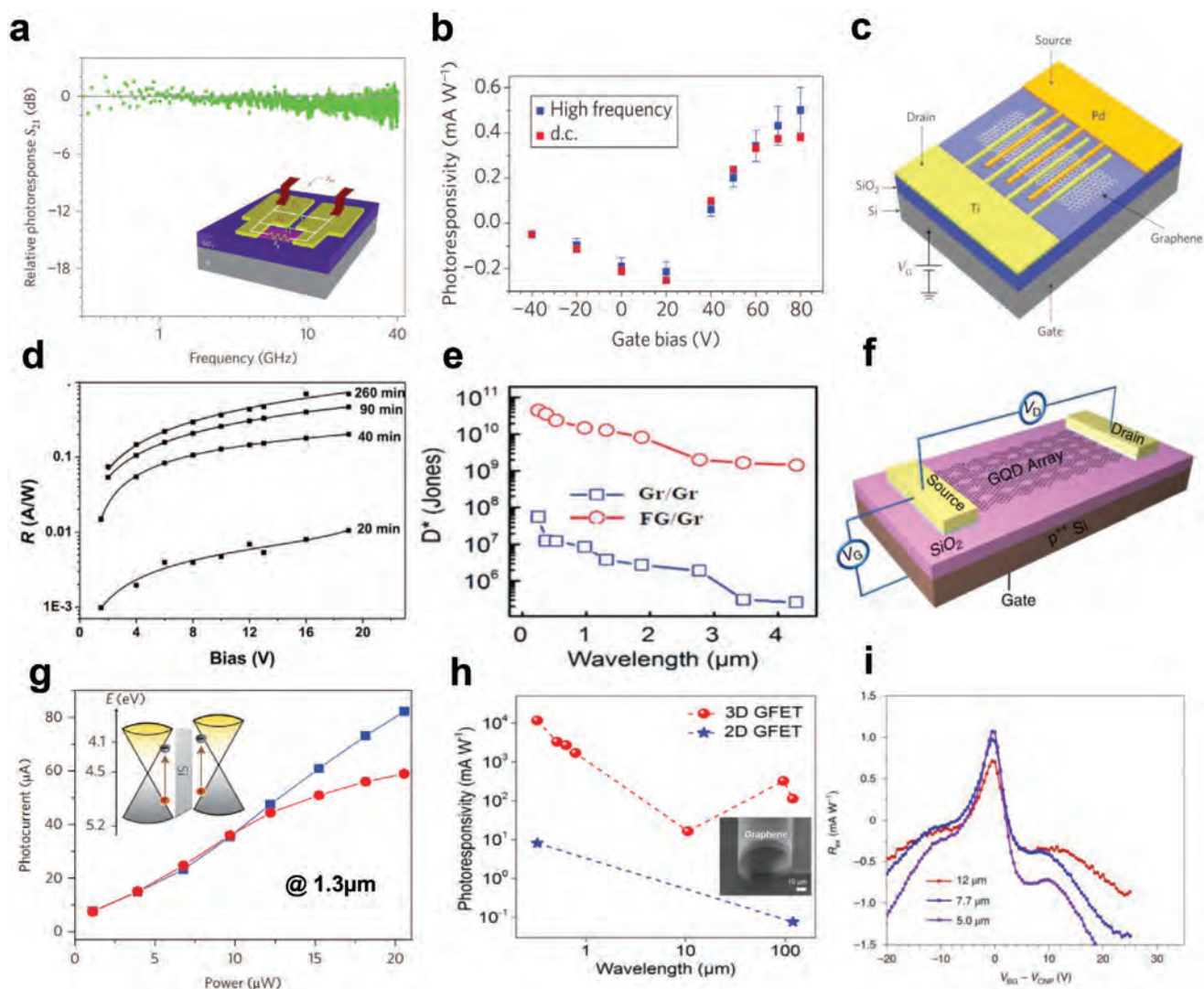


Figure 6. a) 1.55 μm photoresponse as a function of the incident-light modulation frequency for a graphene-based IR photodetector. The inset shows the device configuration. b) 1.55 μm photoresponsivity measured for the graphene photodetector in panel (a) as a function of gate bias, with a maximum photoresponsivity of 0.5 mA W^{-1} at a gate bias of 80 V. The extracted bandwidth is up to 40 GHz. Reproduced with permission.^[32] Copyright 2009, Nature Publishing Group. c) Schematic of a graphene IR photodetector with asymmetric interdigitated electrodes. Reproduced with permission.^[140] Copyright 2010, Nature Publishing Group. d) 0.895 μm responsivity R as a function of bias voltage for an FRGO IR photodetector treated with different reduction times (i.e., 20, 40, 90, and 260 min). Reproduced with permission.^[142] Copyright 2013, American Chemical Society. e) The specific detectivity D^* as a function of the incident light wavelength for an IR photodetector based on pristine graphene (Gr/Gr) and graphene decorated by fluorine-functionalized derivative (FG/Gr). Reproduced with permission.^[143] Copyright 2017, John Wiley & Sons, Inc. f) Schematic of an IR photodetector based on an array of graphene quantum dots (GQDs). Reproduced with permission.^[144] Copyright 2013, Nature Publishing Group. g) 1.3 μm photocurrent as a function of the incident-light power for an IR photodetector with a stacked graphene/SiO₂ interlayer/graphene structure at a back-gate voltage of -60 V (blue squares) and -30 V (red circles).^[12] The inset represents the band diagram of the stacked structure. Reproduced with permission.^[12] Copyright 2014, Nature Publishing Group. h) Spectral responsivity for IR photodetectors based on 3D tubular graphene (3D GFET, red dots) and 2D planar graphene (2D GFET, blue dots). The inset represents the SEM image of the 3D tubular graphene photodetector. Reproduced with permission.^[145] Copyright 2019, American Chemical Society. i) The extrinsic responsivity R_{ex} as a function of the difference between the applied gate voltage V_{BG} and the charge-neutrality-point gate voltage V_{CNP} for a twisted-bilayer graphene detector covered by an h-BN layer under 5, 7.7, and 12 μm light illumination. Reproduced with permission.^[146] Copyright 2020, Nature Publishing Group.

photoconductive gain of 82 700%, as shown in Figure 7b, and a specific detectivity of 1.31×10^9 Jones. The authors concluded that the high photoconductive gain was attributed to the photogating effect, in which some photoexcited holes were trapped by trap states and acted as a charged gate, enabling extended lifetime of the photoexcited electrons. Moving beyond the NIR

region, the PdSe₂-based photodetector exhibited a much lower responsivity of 1.9 mA W^{-1} at a source–drain voltage of 0.2 V at an MWIR wavelength of 4.05 μm due to the weak light absorption of PdSe₂ at longer IR wavelengths.

In addition to 2D TMD semiconductors, some 2D compound semiconductors (e.g., SnTe,^[151] GeAs,^[152] NbS₃,^[153] TaIrTe₄,^[154]

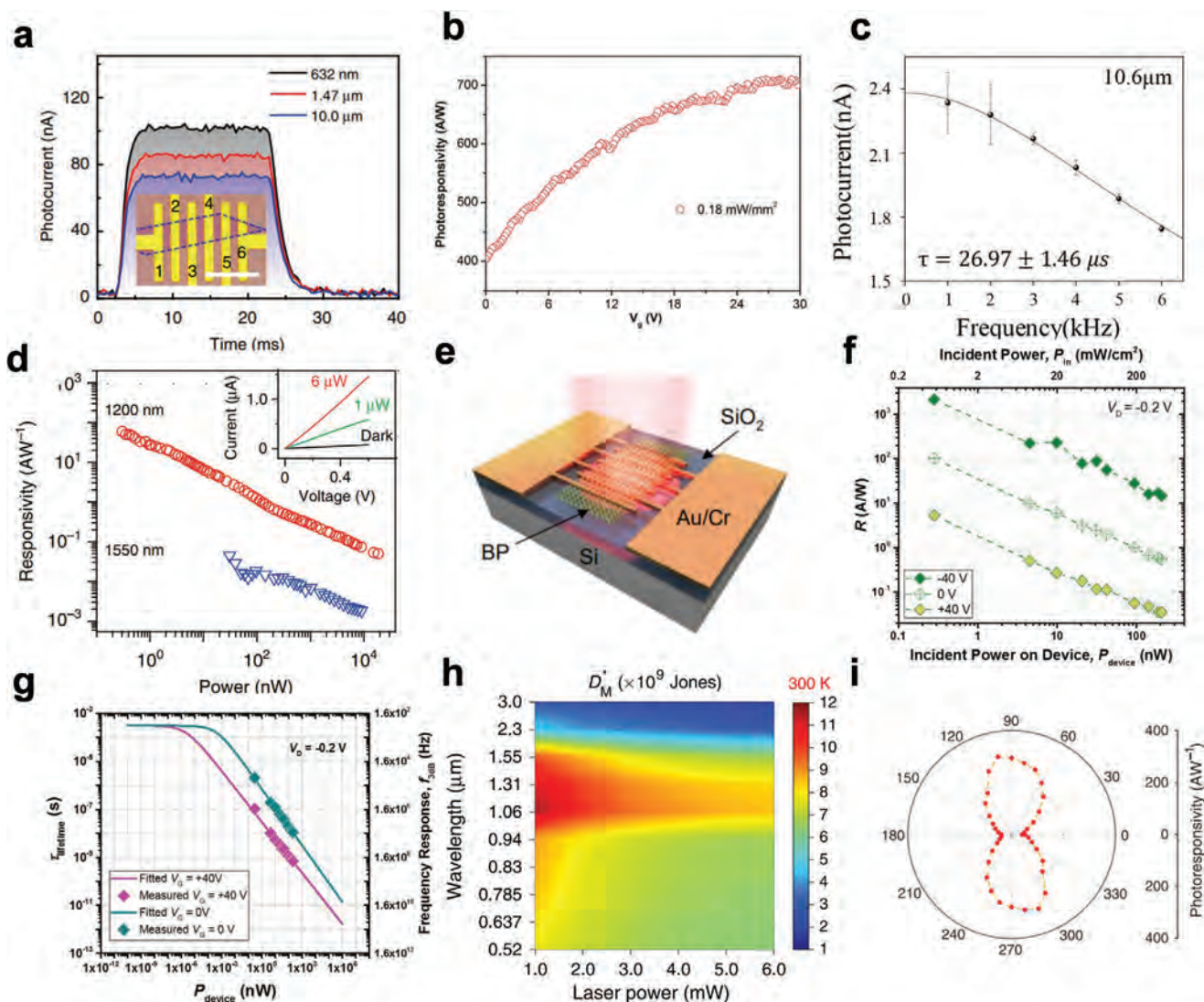


Figure 7. a) Time trace of the photocurrent for a bilayer PtSe₂-based IR photoconductor under 0.632, 1.47, and 10.0 μm illumination. The inset shows an optical image of the bilayer PtSe₂-based IR photoconductor. Reproduced with permission.^[85] Copyright 2018, Nature Publishing Group. b) Responsivity as a function of gate voltage V_g under 1.06 μm illumination for the 2D PdSe₂-based IR photoconductor. Reproduced with permission.^[150] Copyright 2019, John Wiley & Sons, Inc. c) Photocurrent as a function of the modulation frequency of incident light with a wavelength of 10.6 μm for the 2D TaIrTe₄-based IR photoconductor. Reproduced with permission.^[154] Copyright 2018, American Chemical Society. d) Responsivity as function of the power of incident light with a wavelength of 1.2 μm (red circles) and 1.55 μm (blue triangles) for the 2D Bi₂O₂Se-based IR photoconductor. The inset presents the I - V characteristics of this photoconductor under dark conditions (the black line) and illumination (the red and green lines). Reproduced with permission.^[19] Copyright 2018, Nature Publishing Group. e) Schematic of the bP-based IR photoconductor adopting the finger-like contact. Reproduced with permission.^[158] Copyright 2016, American Chemical Society. f) Responsivity R as a function of incident power on device P_{device} under 2.004 μm illumination for the b-PC IR photoconductor. g) Carrier lifetime τ_{lifetime} and frequency response $f_{3\text{dB}}$ as a function of P_{device} under 2.004 μm illumination for the b-PC photoconductor in panel (f). Reproduced with permission.^[159] Copyright 2018, John Wiley & Sons, Inc. h) Specific detectivity D^* as a function of incident wavelength and laser power at a temperature of 300 K for the 2D Te-based IR photoconductor. i) Photoresponsivity as function of the polarization angle of incident light with a wavelength of 2.3 μm for the Te-based photoconductor in panel (h). Reproduced with permission.^[160] Copyright 2020, Nature Publishing Group.

ZrGeTe₄,^[155] and Bi₂O₂Se^[19] have been used to explore high-performance IR photoconductors. For example, Lai et al. demonstrated a TaIrTe₄-based LWIR photoconductor, which realized high speed and highly anisotropic photoresponse over a broad spectral range from 0.532 to 10.6 μm.^[154] Under modulated illumination at a wavelength of 10.6 μm, the room-temperature photocurrent of the photodetector does not undergo a dramatic decrease with modulation frequency below a few kilohertz

(kHz) as shown in Figure 7c, which corresponds to a response time of 26.97 μs. Similarly, Yin et al. fabricated a Bi₂O₂Se-based IR photoconductor, which realized a high responsivity of $\approx 65 \text{ A W}^{-1}$ at 1.2 μm, as shown in Figure 7d, and a fast response time of $\approx 1 \text{ ps}$ corresponding to a photodetection bandwidth up to 500 GHz. The large bandwidth of the detector is likely due to the high electron mobility of Bi₂O₂Se.^[19] Note that although graphene can also achieve a high-speed response comparable to

$\text{Bi}_2\text{O}_2\text{Se}$, the nonzero bandgap of $\text{Bi}_2\text{O}_2\text{Se}$ could render a lower dark current and thus higher specific detectivity.

In addition to the aforementioned compound 2D semiconductors, 2D bP as a promising candidate for IR photodetectors has received extensive research attention, particularly in the MWIR regime owing to its narrow bandgap of ≈ 0.3 eV.^[29,156,157] For example, Guo et al. demonstrated a bP-based IR photoconductor that was able to work in a wide wavelength range from 0.532 to 3.39 μm , as shown in Figure 7e.^[158] The photoconductor consists of ≈ 12 nm thick bP on a SiO_2/Si substrate and is contacted with 1 μm spacing interdigitated electrodes. This electrode configuration enabled fast transit time of the carriers in the channel and efficient carrier extraction. Consequently, a considerable photoconductive gain was achieved in the bP-based photodetector, which results in a responsivity up to 82 A W^{-1} at an MWIR wavelength of 3.39 μm at room temperature. Note that the trap states in bP also played an important role in producing photoconductive gain, as these increased the carrier lifetime by reducing carrier recombination. Besides pristine bP, alloyed bP has been used to fabricate IR photoconductors, including $\text{bAs}_x\text{P}_{1-x}$ and black phosphorus carbide (b-PC).^[81,159] For example, Tan et al. demonstrated SWIR photoconductors based on the 2D b-PC, in which the few-layer b-PC was sandwiched between the top Al_2O_3 passivation layer and the bottom SiO_2 layer on the Si substrate.^[159] Under illumination at a wavelength of 2.004 μm , a responsivity as high as 2163 A W^{-1} was achieved at a bias of 0.2 V at room temperature. This high responsivity was realized by a considerable photoconductive gain of 1.3×10^4 , as shown in Figure 7f. A specific detectivity of $\approx 10^{11}$ Jones was realized. A fast response time of ≈ 0.7 ns was also acquired at the same wavelength and bias voltage, corresponding to a 3 dB bandwidth of ≈ 0.2 GHz, as shown in Figure 7g. As another emerging 2D semiconductor, tellurium with a tunable bandgap (i.e., from 0.35 eV in the bulk case to 1.04 eV in the monolayer case) is a promising candidate for IR photodetectors. Most recently, Tong et al. proposed a 2D Te-based photoconductor, which realized an excellent detection performance over the SWIR regime.^[160] Specifically, the Te-based photodetector achieved a wide spectral response ranging from 0.52 to 3.0 μm at room temperature, with the highest responsivity of $\approx 1.36 \times 10^3$ A W^{-1} obtained under 1.06 μm illumination, corresponding to a specific detectivity of $\approx 1.15 \times 10^{10}$ Jones. For illumination at a wavelength of 3.0 μm , the same device maintained a responsivity that is higher than $\approx 3.53 \times 10^2$ A W^{-1} , corresponding to a detectivity of $\approx 3.01 \times 10^9$ Jones, as shown in Figure 7h. Importantly, due to the asymmetric crystal structure of Te, a highly polarization-dependent photoresponse was observed, with an anisotropic ratio up to ≈ 7.58 under illumination at a wavelength of 2.3 μm , as shown in Figure 7i.

Recently, Wang et al. put forward a new IR photodetector scheme based on the combination of MoS_2 with ferroelectric materials.^[161] The electrostatic field enabled by ferroelectric polarization suppresses the dark current and tunes the bandgap of the photoactive materials. This not only leads to improved photoresponse, but also broadens the detection range to that it spans visible to NIR. This approach opens a new avenue for 2D material photodetectors.

6.3. IR Photodiodes Based on 2D Material/Sensitizing Layer Hybrid Structures

For the aforementioned IR photoconductors based on single channels of various 2D materials, a thinner channel can favor a lower dark current and a more efficient gate-modulation, which are both desirable for high-performance IR photodetectors.^[162] However, a thinner channel will possess a larger bandgap, which limits the operational spectral range of these 2D material-based photodetectors. In addition, the light absorption in an ultrathin channel is relatively low, which limits the responsivity of photodetectors. Consequently, it remains challenging to achieve large optical absorption in 2D material-based IR photoconductors with very thin channels. Next to optical methods using metallic nanostructures and microcavities, another exciting strategy to enhance the light absorption in 2D channel materials is to sensitize the thin channels with strong absorbing semiconductors. The sensitizing layer can also act as a source of trap centers to trap photoexcited electrons (or holes), which allows the holes (or electrons) in the channels to recirculate many times, thus resulting in a photoconductive gain considerably higher than those in typical photoconductors. To date, several types of sensitizing layers have been employed in IR photoconductors, including QDs,^[30,163] nanoparticles,^[164] carbon nanotubes (CNTs),^[165] and certain 2D materials.^[166–169] As a typical example, Konstantatos et al. first demonstrated a hybrid IR photoconductor composed of single or few-layer graphene covered by a thin film of PbS QDs, as shown in Figure 8a.^[71] In the hybrid photoconductor decorated with PbS QDs, a peak spectral response varying from the NIR to the SWIR was realized by tuning the size of PbS QDs. More specifically, the peak position of the responsivity was shifted from ≈ 0.95 μm NIR to ≈ 1.45 μm SWIR when the size of PbS QDs becomes large, as shown in Figure 8b. Remarkably high responsivities were obtained across the NIR region at room temperature, with values of $\approx 5 \times 10^7$ and $\approx 5 \times 10^5$ A W^{-1} at wavelengths of 0.95 and 1.45 μm , respectively. This high responsivity was due to electrons being trapped in the PbS QDs, which induced positive charges from the external electrodes to recirculate in the graphene channel, leading to a photoconductive gain and high responsivity, as shown in Figure 8c. Following this, Ni et al. fabricated a Si QDs/graphene hybrid MWIR photoconductor, in which a thin layer of boron-doped Si QDs was deposited onto the graphene on a SiO_2/Si substrate.^[27] Under the illuminations at wavelengths shorter than 1.82 μm , the Si QD-covered photodetector achieved an excellent responsivity as high as $\approx 10^8$ A W^{-1} , as shown in Figure 8d. In contrast, the responsivities observed at longer wavelengths were much lower (i.e., ≈ 1 A W^{-1} at 3.0 μm). This distinct difference in the responsivity originated from the fact that a strong light absorption at short IR wavelengths was enabled by the optical bandgap transition of Si QDs, while Si QDs does not absorb MWIR light, instead it supports localized surface plasmon resonances, which only provide modest enhancement to the absorption in the graphene. Besides PbS and Si QDs, PbSe QDs,^[96] Ti_2O_3 nanoparticles,^[164] Bi_2Ti_3 nanoplatelets,^[170] and CNTs^[165] have been utilized as the sensitizing layers in graphene-based IR photoconductors. For instance, Yu et al. demonstrated an LWIR hybrid photoconductor made by the

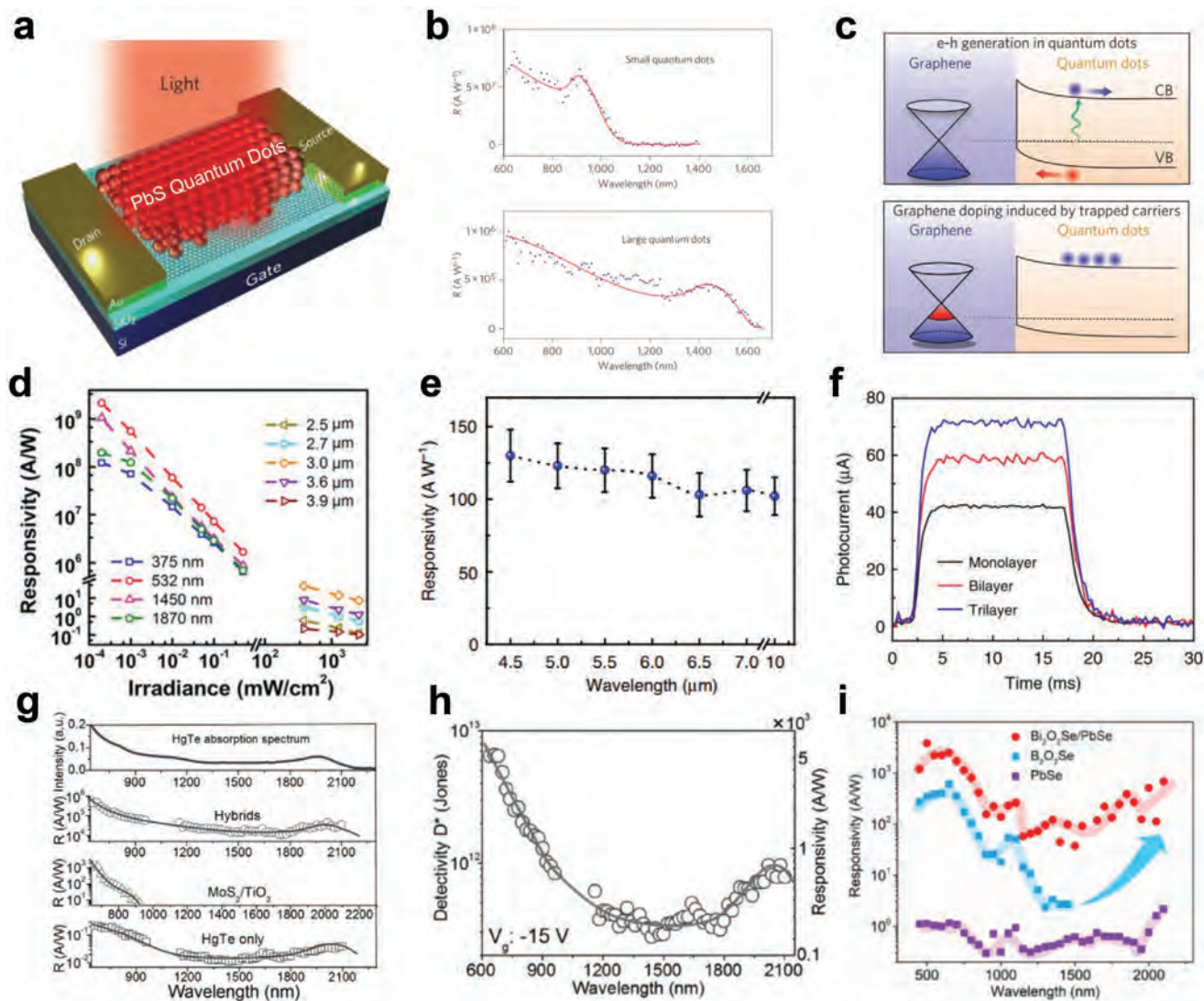


Figure 8. a) Schematic of a photoconductor made by graphene covered by a thin film of PbS QDs as a sensitive layer. b) Responsivity R as a function of the wavelength of incident light for the graphene photoconductor in panel (a), with small PbS QDs (upper panel) and large PbS QDs (bottom panel), respectively. c) Band diagram of the graphene/PbS QDs heterostructure, corresponding to the generation of electron–hole pairs in QDs (upper panel) and the doping of graphene induced by trapped carriers (bottom panel). Reproduced with permission.^[27] Copyright 2012, Nature Publishing Group. d) Responsivity as a function of the incident power at a series of wavelengths for the graphene-based IR photoconductor sensitized by a layer of Si QDs. Reproduced with permission.^[27] Copyright 2017, American Chemical Society. e) Responsivity as a function of the wavelength of incident light for the IR photoconductor based on graphene covered by Ti_2O_3 nanoparticles. f) Time trace of the photocurrent of the IR photoconductor in (e), with different layer-number graphene. Reproduced with permission.^[64] Copyright 2018, Nature Publishing Group. g) Responsivity R as a function of the wavelength of incident light for the IR photoconductor based on the $\text{MoS}_2/\text{TiO}_2/\text{HgTe}$ QDs hybrid structure, $\text{MoS}_2/\text{TiO}_2$, and only HgTe QDs, respectively. The top panel represents the absorption spectrum of HgTe as reference. h) Specific detectivity D^* and responsivity as a function of the wavelength of incident light at a gate voltage of -15 V for the hybrid photoconductor in panel (g). Reproduced with permission.^[4] Copyright 2017, John Wiley & Sons, Inc. i) Responsivity as a function of the wavelength of incident light for the IR photoconductor based on the $\text{Bi}_2\text{O}_2\text{Se}/\text{PbSe}$ hybrid structure, $\text{Bi}_2\text{O}_2\text{Se}$, and PbSe, respectively. Reproduced with permission.^[74] Copyright 2019, American Chemical Society.

few-layer graphene coupled with Ti_2O_3 nanoparticles.^[164] In such a photodetector configuration, Ti_2O_3 nanoparticles with a narrow bandgap of ≈ 0.09 eV produced a broadband response up to the LWIR spectral region, while graphene enabled the high-speed transport of carriers in the channel. As a result, the Ti_2O_3 /trilayer-graphene photodetector achieved a room-temperature responsivity higher than $\approx 10^2$ A W^{-1} over a broad-spectral range spanning from 4.5 to 10 μm , and a specific detectivity of 7×10^8 Jones at a wavelength of 10 μm , as shown in Figure 8e.

In addition, a response time of ≈ 1.2 ms was measured on these devices as shown in Figure 8f.

Besides graphene, 2D TMDs have been integrated with various sensitizing layers to develop high-performance IR photoconductors.^[171,172] For example, Kufer et al. presented a MoS_2/PbS QDs hybrid photoconductor, in which a few layers of n-type MoS_2 were covered with p-type PbS QDs.^[78] By using the narrow-bandgap PbS QDs as an optical absorber, the hybrid photodetector exhibited a broader spectral response compared

with the bare MoS₂-based photodetector, which extended to wavelength of 1.1 from 0.7 μm. In addition, the hybrid photodetector also achieved an overall improvement of ≈5 orders of magnitude in the responsivity, which was achieved by the high photoconductive gain offered by the PbS QDs. The use of PbS QDs has also been demonstrated on WS₂ and SnS₂-based photoconductors for SWIR detection.^[171,172]

As another narrow-bandgap semiconductor, HgTe colloidal QDs (CQDs) have also been utilized to sensitize IR photodetectors for higher performance. Huo et al. demonstrated a MoS₂/HgTe QDs hybrid SWIR photoconductor, in which HgTe CQDs were coated onto a few layers of MoS₂ across a thin gap-layer of TiO₂.^[4] Compared with the case of MoS₂/TiO₂ and bare HgTe, the hybrid photodetector realized both a wider spectral response extending to 2.1 μm and a high responsivity of ≈10⁴ A W⁻¹ at a wavelength of 2.1 μm, as a result of a photoconductive gain induced by HgTe CQDs at the IR regime, as shown in Figure 8g. Note that a high specific detectivity of ≈10¹² Jones was acquired at an SWIR wavelength of 2 μm as shown in Figure 8h, which was realized due to the significantly suppressed dark current when the detector was working in the depletion regime by applying an appropriate gate-voltage.

In addition to the aforementioned graphene and TMD-based devices, sensitizing layers have been introduced into other 2D semiconductor-based IR photoconductors, including CdS_xSe_{1-x}^[173] and Bi₂O₂Se.^[174] Taking Bi₂O₂Se as an example, Luo et al. reported a Bi₂O₂Se-based hybrid IR photoconductor sensitized by PbSe CQDs.^[174] As compared to the bare Bi₂O₂Se-based photodetector, the hybrid device exhibited a wider response spectrum extending to 2 μm in the SWIR, at which a high responsivity of ≈10³ A W⁻¹ was acquired at room temperature, as shown in Figure 8i. This extended spectral response was due to the fact that the PbSe CQDs absorb SWIR light. Compared with the bare PbSe CQD-based photodetector, a few orders of magnitude enhancement of the spectral responsivity were achieved in the hybrid device, as the band offset at the interface of Bi₂O₂Se and PbSe CQDs led to a photogating effect, which yielded a photoconductive gain for the photodetector. Note that such a band offset also permits a fast response time of ≈4 ms, since the photogenerated carriers at the interface can be collected rapidly via the built-in field.

Besides 0D QDs and nanoparticles, Liu et al. also demonstrated that a sensitizing layer consisting of a large number of 1D single-wall carbon nanotubes (SWCNTs) could be placed below the graphene channel to realize a SWIR photoconductive photodetector. A responsivity of ≈10 A W⁻¹ was observed at a wavelength of 1.55 μm at room temperature.^[165] For such a 1D SWCNT-sensitized photodetector, the carriers generated in the SWCNTs/graphene interface were separated efficiently due to the existence of the built-in field. More importantly, photogenerated carriers were trapped in the SWCNTs, leading to a prolonged carrier lifetime and a photoconductive gain.

7. IR Photodiodes Based on 2D Materials van der Waals Heterojunctions

2D material-stacked van der Waals heterojunctions possess many fascinating properties such as ease of band alignment

engineering, efficient interface photocarriers transfer, and strong optical absorption. Due to these advantages, an increasing research effort have been devoted to developing 2D material-based heterojunctions for the realization of high-performance IR photodiodes. Compared with IR photoconductors discussed in Section 6, 2D material-based heterojunction photodiodes feature a built-in electric field that facilitates efficient collection of photocarriers. This provides IR photodetectors with several advantages, including fast response and low dark current, leading to improved bandwidth and specific detectivity, respectively. In this section, we introduce the recent advancements in van der Waals heterojunction-based IR photodiodes assembled by various 2D materials. For clarity, the heterojunction-based IR photodiodes to be introduced adopt the electrode/2D material-based heterojunction/electrode architectures, in which the heterojunction serves as both the absorber to produce photoexcited carriers and the conducting channel for separation of carriers.

7.1. IR Photodiodes Based on Graphene/2D Semiconductor van der Waals Heterojunctions

To further improve the performance of graphene-based devices, a heterojunction with another 2D material can be introduced to decrease the dark current. A specific solution is to construct van der Waals heterojunction-based photodiodes by stacking graphene and 2D semiconductors together, in which the existence of junction potential barriers can lead to a reduction of the dark current. Note that the separation of photogenerated carriers is also more efficient under the built-in field in the junction region. Based on these considerations, various kinds of photodiodes based on graphene/2D semiconductor heterojunctions have been reported for IR detection. As a typical example, Vabbina et al. fabricated a SWIR photodiode by stacking a few layers of p-type MoS₂ over a graphene layer to form a vdW heterojunction.^[175] The photodetector exhibited a broad spectral response covering the SWIR regime, as shown in Figure 9a. A maximum responsivity of 1.26 A W⁻¹ at a wavelength of 1.44 μm was extracted, which corresponds to a specific detectivity of 4 × 10¹⁰ Jones. This broadband spectral response was attributed to the existence of two operating modes of the photodetector, namely an optical bandgap excitation mode and an internal photoemission mode. In the former mode, electron–hole pairs are excited when the incident photon energy is larger than the bandgap of MoS₂, which leads to the photoresponse at short wavelengths. However, in the latter mode, electron–hole pairs can still be excited by incident photons with an energy lower than the bandgap of MoS₂, due to the internal transition occurring between the graphene and MoS₂. This transition leads to the photoemission across the potential barrier at the junction region, as shown in Figure 9b. Later on, Long et al. presented an SWIR photodiode based on the MoS₂/graphene/WSe₂ vdW heterojunction, in which the graphene layer was sandwiched between the bottom p-type MoS₂ layer and the top n-type WSe₂ layer on the SiO₂/Si substrate.^[176] In such a vdW heterojunction-based photodiode, the combination of the broadband absorption in graphene and the efficient separation of the carriers in the p–n junction region made it possible to realize both

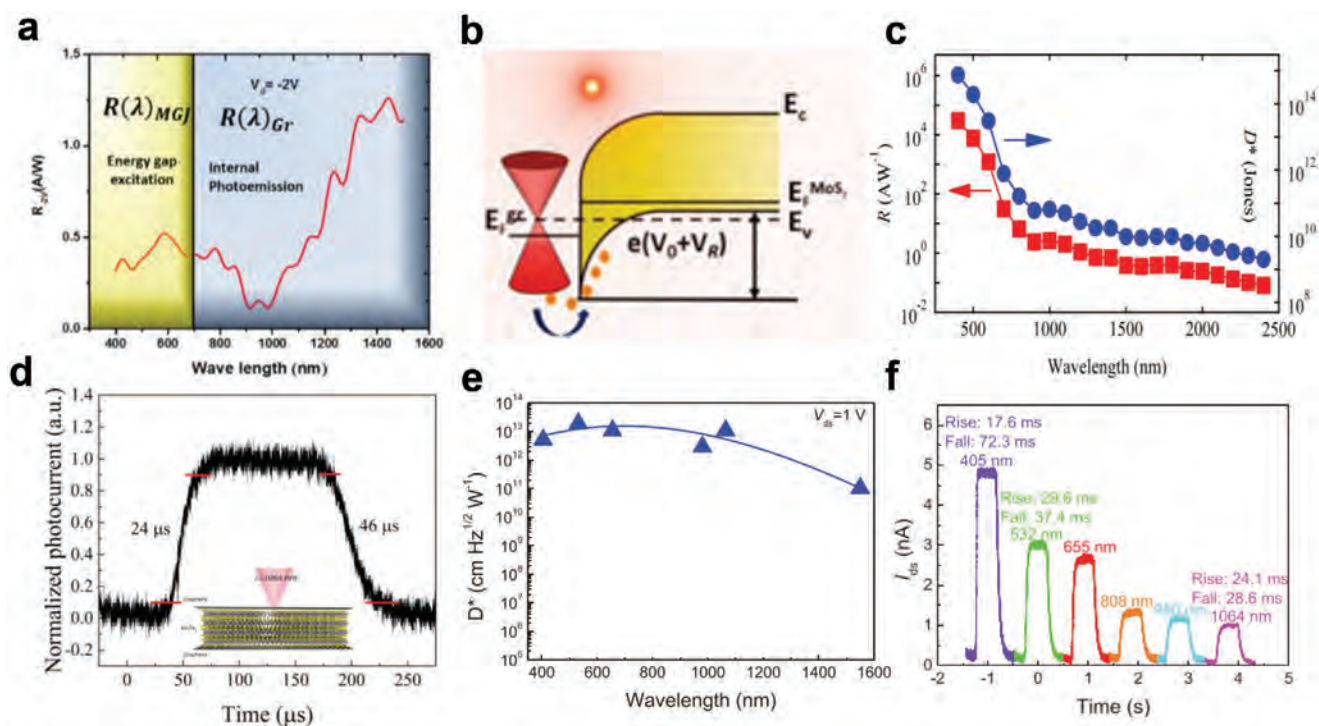


Figure 9. a) Responsivity R as a function of the wavelength of incident light at a bias of -2 V for the graphene/ MoS_2 IR photodiode. b) Band diagram of the graphene/ MoS_2 heterostructure in panel (a) when internal photoemission occurs under reverse bias. Reproduced with permission.^[175] Copyright 2015, American Chemical Society. c) Responsivity R and specific detectivity D^* as a function of the wavelength of incident light for the IR photodiode based on the MoS_2 /graphene/ WSe_2 heterojunction. Reproduced with permission.^[176] Copyright 2016, American Chemical Society. d) Time trace of the normalized photocurrent of the IR photodiode based on the graphene/ MoTe_2 /graphene heterojunction. The inset is a schematic of this photodiode. Reproduced with permission.^[177] Copyright 2017, American Chemical Society. e) Specific detectivity D^* as a function of the wavelength of incident light at a source–drain voltage V_{ds} of 1 V for the IR photodiode based on the MoTe_2 /graphene/ SnS_2 heterojunction. f) Time trace of the source–drain current I_{ds} under illumination with different wavelengths (represented by colored lines) for the IR photodiode in panel (e). Reproduced with permission.^[179] Copyright 2019, John Wiley & Sons, Inc.

wide spectral response and high specific detectivity. Consequently, a broadband photodetection was achieved that covered a wavelength range from 0.4 to 2.4 μm , as shown in Figure 9c. Importantly, the room-temperature specific detectivity of the photodetector was as high as $\approx 10^9$ Jones at a SWIR wavelength of 2.4 μm . In addition to the aforementioned MoS_2 /graphene/ WSe_2 heterojunction, other kinds of sandwich-like heterojunctions based on graphene have also been demonstrated for IR photodetectors, such as the graphene/ MoTe_2 /graphene heterojunction^[177] and the MoS_2 /graphene/ MoS_2 heterojunction.^[178] Under the SWIR illumination ($\lambda = 1.064$ μm), the photodetector exhibited a responsivity of 110 mA W^{-1} under zero-bias at room temperature, corresponding to an EQE of $\approx 12.9\%$. Notably, a short response time of ≈ 24 μs was achieved at the same wavelength as shown in Figure 9d, which benefited from the short transit distance of the photogenerated carriers in this vertical graphene/ MoTe_2 /graphene heterojunction. As in photoconductors, the photoconductive gain has been achieved in graphene-based vdW heterojunction IR photodiodes. For example, Li et al. demonstrated a SWIR photodiode based on the MoTe_2 /graphene/ SnS_2 vdW heterojunction, in which the graphene layer was placed between the top MoTe_2 layer and the bottom SnS_2 layer. The MoTe_2 /graphene/ SnS_2 stacked heterostructure was isolated from the environment by covering it with two layers of thin h-BN.^[179] In such a photodetector configuration,

the combination of p-type MoTe_2 (bandgap ≈ 1.0 eV) and n-type SnS_2 (bandgap ≈ 2.2 eV) provided the photodetector with a broad absorption spectrum. In addition, the vertical built-in field in the graphene interlayer strengthened the charge transfer and exciton dissociation efficiently. As a result, the photodetector exhibited a wide spectral response spanning from 0.4 to 1.6 μm as shown in Figure 9e. More importantly, a responsivity of $\approx 2.64 \times 10^3$ A W^{-1} was observed at a forward bias of 1 V at a wavelength of 1.064 μm , corresponding to a specific detectivity of 1.1×10^{13} Jones and an EQE up to $\approx 10^4$. The EQE larger than one means that a photoconductive gain was produced in the photodetector, which was due to the short transit distance of the charges in the vertical junction, interlayer inelastic tunneling effect, and rapid carrier transport. Besides, the detector response time also reached a few tens of ms at various wavelengths, e.g., a rise time of 24.1 ms was measured at 1.064 μm , as shown in Figure 9f.

7.2. IR Photodiodes Based on 2D Semiconductor van der Waals Heterojunctions

Unlike graphene, which lacks a bandgap, 2D semiconductors such as TMDs typically show a low dark current as desired in IR photodetectors, due to their moderate bandgaps. However,

the existence of the bandgaps in 2D semiconductors also limits the spectral response range of photodetectors made by these families of materials. For example, MoS₂ has exhibited excellent potential in many optoelectronic applications, especially in photodetectors. However, the photodetectors based on bare MoS₂ can only work in the visible region, which limits their IR applications. To overcome this, different 2D semiconductors can be stacked to form van der Waals heterojunctions. By forming heterojunctions between 2D semiconductors with different bandgaps and work functions, it is possible to engineer the optical bandgap of the photodetectors. In addition to the bandgap engineering, the carrier densities and band alignments in 2D semiconductors could be tuned by applying an electrostatic voltage, providing the opportunity to develop novel heterostructures with various features.^[15] Significant efforts have been devoted to exploring high-performance IR photodiodes based on 2D semiconductor vdW heterojunctions. 2D TMDs are commonly used in this application. As a typical example, Zhang et al. demonstrated a SWIR photodiode based on a MoTe₂/MoS₂ vdW heterojunction as shown in **Figure 10a**, which realized a sub-bandgap detection at a wavelength of 1.55 μm at room temperature.^[73] This response at the sub-bandgap wavelength was due to the formation of the type-II staggered band, which enabled an interlayer optical transition with an energy of ≈0.657 eV, as shown in **Figure 10b**. The interlayer optical transition allows for photogeneration of carriers even though the energy of incident photons is less than the bandgap of either monolayer MoS₂ (1.80–1.90 eV) or monolayer MoTe₂ (≈1.05 eV). By employing this device architecture, the spectral response of the photodetector was extended effectively. Beyond this, 2D materials with narrow nonzero bandgaps can also be used directly as an IR absorber. For example, Long et al. reported an LWIR photodiode based on the PdSe₂/MoS₂ vdW heterojunction.^[13] Under illumination at a wavelength of 10.6 μm, the photodetector exhibited a high responsivity of ≈42.1 A W⁻¹ at a forward bias of 1 V at room temperature, corresponding to an excellent specific detectivity of 8.21 × 10⁹ Jones as shown in **Figure 10c**. Apart from the high detection sensitivity, a broadband response was achieved that ranges from the visible to the LWIR, with a room-temperature specific detectivity higher than ≈5 × 10⁹ Jones, which is higher than many mainstream IR photodetectors. Note that the formation of the vdW heterojunction allowed a low dark current, which was the main reason for the improved specific detectivity observed in the PdS₂/MoS₂ vdW heterojunction-based photodiode, as compared to the PdS₂-based photoconductor. In addition to the aforementioned 2D TMDs, other types of 2D TMDs have been used to construct 2D vdW heterostructures for high-performance photodetection at various IR wavelengths, such as the MoS₂/MoTe₂ heterojunction for 0.8 μm NIR detection,^[33] the PtSe₂/PtS₂ heterojunction for 1.064 μm SWIR detection,^[180] and the WSe₂/Bi₂Te₃ heterojunction for 1.55 μm SWIR detection.^[28] Unlike 2D TMDs, which are used mainly for SWIR detection, bP is a promising 2D material for the construction of the vdW heterojunction for the detection of longer IR light due to its narrow bandgap. For example, Bullock et al. presented a high-performance MWIR photodiode based on the MoS₂/bP vdW heterojunction consisted of a 150 nm thick p-type bP layer and a thin (≈10 nm thick) n-type MoS₂ layer. The MoS₂ layer acted as electron-selective contact and MWIR optical

window.^[7] In such a photodiode, the dark current noise was effectively suppressed by the potential barrier presented in the heterojunction. As a result, under illumination at a wavelength of 3.8 μm, a high room-temperature specific detectivity of 1.1 × 10¹⁰ Jones was achieved at zero-bias, corresponding to an external quantum efficiency of ≈35%, as shown in **Figure 10d**. The response spectrum of the photodetector covered a broad wavelength range from 1.5 to 3.8 μm, with an overall specific detectivity higher than ≈10¹⁰ Jones, which outperforms many of the established state-of-the-art IR photodetectors at room temperature. Besides the sensitive photodetection, the photodetector also realized a fast response with a measured rise time of 3.7 μs and a fall time of 4 μs for illumination at a wavelength of 2.7 μm, as shown in **Figure 10e**. Owing to the anisotropic crystalline structure of bP, the bP-based photodiode also exhibited a strong polarization-dependent quantum efficiency (η_e) under the illumination at a wavelength of 3.5 μm, as shown in **Figure 10f**. In addition to pristine bP, black arsenic phosphorus has also been exemplified as a promising candidate for MWIR photodetectors. Long et al. reported that, by leveraging the narrow optical bandgap and facile heterojunction construction of the 2D b-AsP in the form of As_xP_{1-x}, a b-AsP/MoS₂ stacked vdW heterojunction-based photodiode was fabricated and exhibited a superior MWIR photodetection performance.^[16] Specifically, under broadband illumination from the 3 to 5 μm, the photodetector showed an excellent specific detectivity higher than 4.9 × 10⁹ Jones at zero-bias at room temperature, which outperformed some of the commercially available IR photodetectors, such as the PbSe-based and thermistor-based IR photodetectors as shown in **Figure 10g**. This superior specific detectivity observed in the b-AsP-based vdW heterojunction photodiode was attributed to the suppressed dark current, due to the existence of a potential barrier at the p-type b-As_xP_{1-x} and n-type MoS₂ heterojunction, as shown in **Figure 10h**. A significant specific detectivity improvement of ≈2 orders of magnitude was achieved over the bare b-As_xP_{1-x} photoconductor. In addition to the high specific detectivity, a short response time of ≈0.5 ms was acquired at a wavelength of 4 μm as shown in **Figure 10i**. Apart from the MWIR regime, some bP-based vdW heterojunction photodiodes have also achieved high-performance in the SWIR region, such as the MoS₂/bP heterojunction for 1.55 μm detection,^[181] the WSe₂/bP/MoS₂ sandwich-like heterojunction for 1.55 μm detection, and the PdSe₂/bP heterojunction for 1.31 μm.^[182]

7.3. IR Photodiodes Based on 2D Materials Mixed-Dimensional Heterojunctions

In addition to van der Waals heterojunctions fabricated by assembling different 2D materials, the combination of 2D materials and non-2D materials (i.e., 0D, 1D, and 3D) can also form mixed-dimensional vdW heterojunctions, as the 2D materials that are free of dangling bonds can form vdW heterojunctions with materials of any dimensions.^[183] The versatility of mixed-dimensional approaches has attracted intensive research attention to explore their use in diverse applications, particularly in IR photodetectors. As a typical example, Noubé et al. demonstrated an IR photodetector based on the 2D graphene/0D HgTe

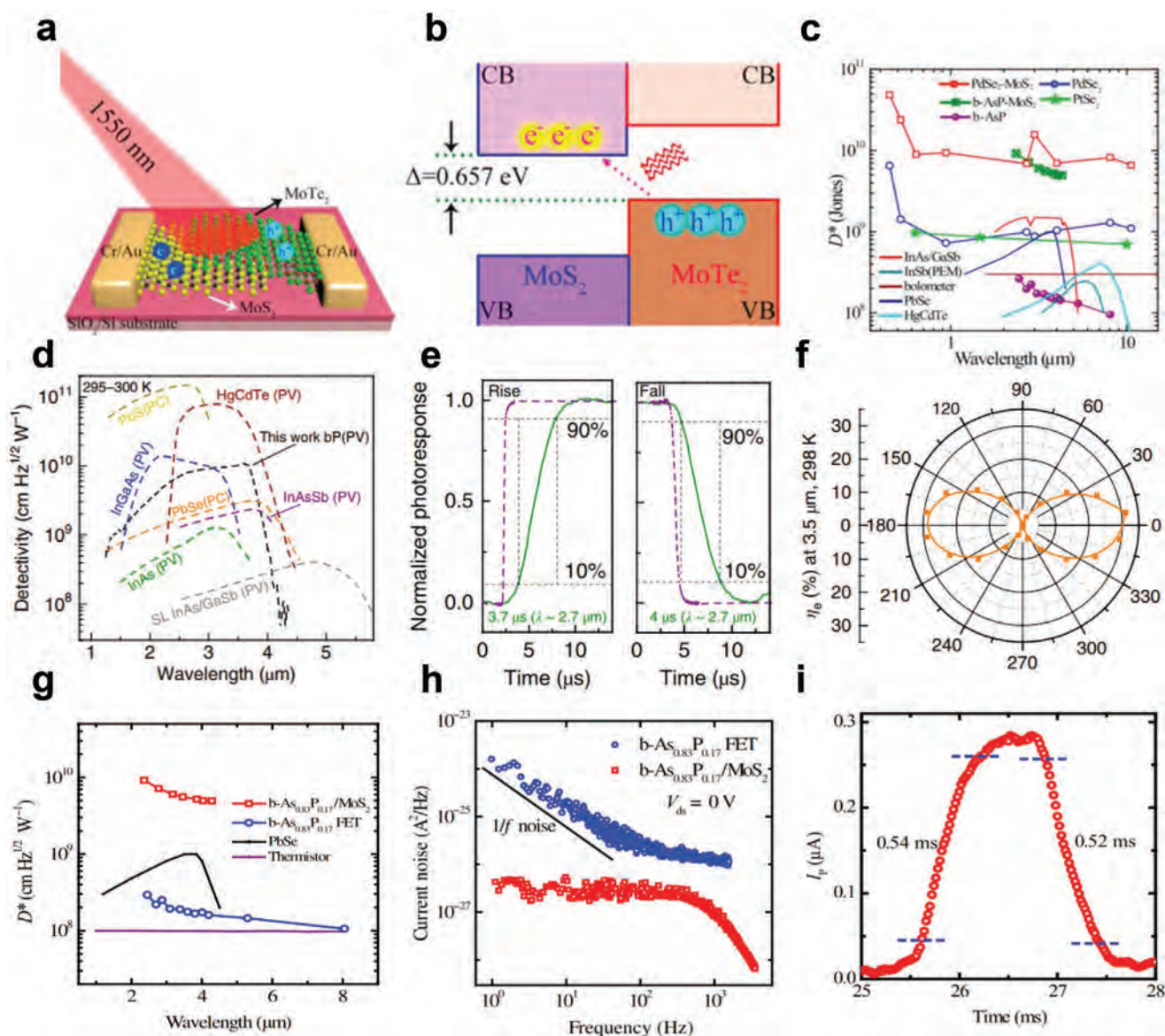


Figure 10. a) Schematic of a photodiode based on the MoTe₂/MoS₂ heterojunction. b) Band diagram of the MoTe₂/MoS₂ heterostructure in panel (a). Reproduced with permission.^[73] Copyright 2016, American Chemical Society. c) Specific detectivity D^* as a function of the wavelength of incident light for PdSe₂/MoS₂ IR photodiodes (red squares) and other types of IR photodetectors. Reproduced with permission.^[13] Copyright 2019, American Chemical Society. d) Specific detectivity as a function of the wavelength of incident light for the IR photodetector based on the MoS₂/bP heterojunction (the black dash line) and compound semiconductors. e) Time response characteristics under 2.7 μm illumination for the IR photodiode in panel (d). f) Polarization dependence of quantum efficiency η_e under 3.5 μm illumination for the IR photodiode in panel (d). Reproduced with permission.^[7] Copyright 2018, Nature Publishing Group. g) Specific detectivity D^* as a function of the wavelength of incident light for the b-AsP/MoS₂ IR photodiode (red squares) and other types of IR photodetectors. h) Current noise versus frequency for the IR photodetector based on the b-AsP/MoS₂ heterojunction (red squares) in panel (g) and only b-AsP (blue circles), respectively. i) Time response characteristics under 4 μm illumination for the photodiode in panel (g). Reproduced with permission.^[16] Copyright 2017, American Association for the Advancement of Science.

nanoparticle vdW heterojunction, which consists of a thin film of HgTe nanocrystals connected with two graphene electrodes on an ionic glass substrate of LaF₃, as shown in Figure 11a.^[184] Owing to the existence of graphene electrodes combined with the ionic glass, the HgTe nanocrystal, and the graphene electrode can be selectively reconfigured between the n-doped and p-doped state to form a p–n junction by applying an appropriate gate voltage. The formation of a p–n junction suppressed the

dark current of the device. As a result, under illumination at a wavelength of 1.55 μm, a specific detectivity of $\approx 10^9$ Jones was acquired at a gate voltage of -2.5 V, despite a weak light absorption of 8%, as shown in Figure 11b. The detector also showed a fast response with a measured rise time of ≈ 9 μs and fall time of ≈ 7 μs, as shown in Figure 11c. Similarly, Liu et al. presented a SWIR photodetector based on a heterostructure formed between a ZnO thin-film and RGO film decorated with

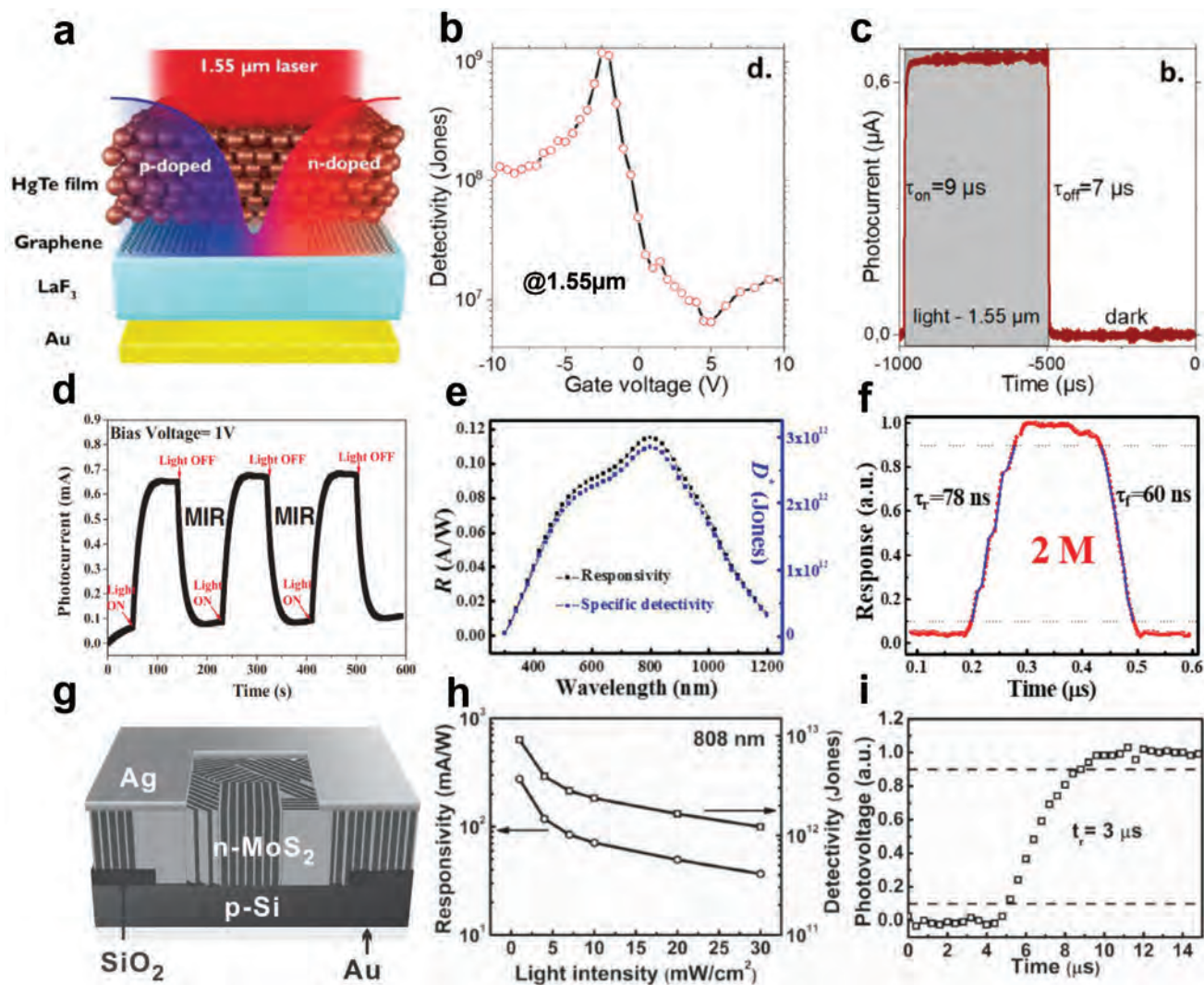


Figure 11. a) Schematic of a graphene/0D HgTe IR photodiode. b) Specific detectivity as a function of gate voltage under 1.55 μm illumination for the photodiode in panel (a). c) Time response characteristics of the photodiode in panel (a). Reproduced with permission.^[184] Copyright 2020, American Chemical Society. d) Time response characteristics of the IR photodiode based on the Si nanowire/graphene heterojunction. Reproduced with permission.^[187] Copyright 2014, John Wiley & Sons, Inc. e) Responsivity R and specific detectivity D^* as a function of the wavelength of incident light for the IR photodiode based on the 3D Cs-doped FAPbI₃ perovskite/2D PtSe₂ heterojunction. f) Time response characteristics of the IR photodiodes in panel (e). Reproduced with permission.^[188] Copyright 2018, American Chemical Society. g) Schematic of an IR photodiode based on the 3D Si/2D MoS₂ heterojunction. h) Responsivity and specific detectivity as a function of light intensity for the IR photodiode in panel (g). i) Time response characteristics of the IR photodiode in panel (g). Reproduced with permission.^[189] Copyright 2015, John Wiley & Sons, Inc.

Ge QDs.^[185] The photodetector realized a high specific detectivity of 6.42×10^{11} Jones for illumination at a wavelength of 1.4 μm . It should be noted that the relatively low dark current of ≈ 3 nA contributed to the high specific detectivity. Notably, a rise time of ≈ 40 μs and a recovery time of ≈ 90 μs were also demonstrated in this photodetector. In addition to 0D nanomaterials, 1D materials such as nanowires can be combined with 2D materials to form mix-dimensional vdW heterojunctions for IR detection.^[186] For example, Cao et al. demonstrated an LWIR photodiode based on a 1D Si nanowire/graphene vdW heterostructure, consisting of an array of vertical n-doped Si nanowires etched into the Si substrate, which was covered by an RGO nanosheet.^[187] Under illumination at a wavelength of 10.6 μm , a peak responsivity of ≈ 9 mA W⁻¹ was achieved at

room temperature as shown in Figure 11d. The measured photoresponse at this wavelength was due to the broadband absorption in graphene.

The most popular strategy for mixed-dimensional IR detectors is by combining 3D bulk semiconductors with 2D materials. For example, Zhang et al. reported a SWIR photodiode based on a 3D/2D vdW heterojunction composed of FA_{0.85}CS_{0.15}PbI₃ perovskite and multilayer PtSe₂ on a SiO₂/Si substrate.^[188] Under illumination at a wavelength of 1 μm at room temperature, the photodetector exhibited an estimated rise/fall time of $\approx 78/60$ ns, corresponding to a bandwidth of ≈ 2 MHz, as shown in Figure 11e. A specific detectivity of up to $\approx 10^{12}$ Jones was realized as shown in Figure 11f. The high speed and specific detectivity of this device can be attributed to the

Table 2. Figures-of-merit of 2D material-based IR photodetectors based on nanophotonic structures.

Materials	Wavelength [μm]	Absorption (enhancement) ^{a)}	IQE/R/D* (enhancement)	Used nanophotonic structures	Refs.
Monolayer graphene	4.45	10% (4–5)	0.4 V W ⁻¹ (>200)	Au nanoantenna array	[39]
Monolayer graphene	10.84	0.36% (558)	D [†] (\approx 32)	Au nanoantenna, Al grating	[41]
Bilayer MoS ₂	1.07	\approx 20%	4.5 A W ⁻¹ (10 ⁵)	Au nanoantenna array	[40]
Graphene	1.55	24%	83 A W ⁻¹	Au nanoparticles array	[208]
Few-layer MoS ₂	0.98	15.1%	64 mA W ⁻¹	Au nanoparticles	[209]
Monolayer graphene	0.855	60% (26)		Fabry–Pérot microcavity	[43]
bP ^{b)} /MoS ₂	3.0	\approx 20% in bP	0.11 A W ⁻¹ /1.7 \times 10 ⁹ Jones	Fabry–Pérot microcavity	[212]
Monolayer graphene	1.535		Photocurrent (\approx 8)	Photonic crystal cavity	[44]
Tellurium nanoflakes	1.4–2.4	\approx 20%	8–13 A W ⁻¹	Optical cavity substrate	[14]
Se _{0.32} Te _{0.68} thin film	1.55		6.5 \times 10 ¹⁰ Jones	Optical cavity substrate	[45]
Monolayer graphene	2.75		0.13 A W ⁻¹	Silicon optical waveguide	[3]
100 nm thick bP	\approx 1.55	17.5%	50%/657 mA W ⁻¹	Silicon photonic waveguide	[34]
32.4 nm thick bP	2.185		40 mA W ⁻¹	ChG ^{c)} waveguide	[217]
Monolayer graphene	1.55		4.7 V W ⁻¹	Silicon PhC ^{d)} waveguide	[136]
Monolayer graphene	12.4	32%		Intrinsic graphene plasmon	[228]
Monolayer graphene	8–12	\approx 60%	2.9 \times 10 ³ V W ⁻¹ /1.1 \times 10 ⁹ Jones	Intrinsic graphene plasmon	[104]

^{a)}In the columns 3 and 4, the numbers in the brackets indicate the corresponding enhancement value compared with the performance of these photodetectors without using the nanophotonic structures; ^{b)}bP: black phosphorus; ^{c)}ChG: chalcogenide glass; ^{d)}PhC: photonic crystal.

rapid separation of the carriers within the heterojunction and the large optical absorption coefficient of the perovskite film.

Crystalline Si has also been widely used to construct 2D material-based mix-dimensional vdW heterojunctions for IR photodetection. For example, Wang et al. demonstrated an NIR photodetector based on a Si/MoS₂ hybrid 3D/2D vdW heterojunction as shown in Figure 11g. The device consists of a \approx 150 nm thick n-type MoS₂ layer deposited vertically on a p-type Si substrate via sputtering deposition.^[189] Note that the gap between these vertical MoS₂ films facilitates the coupling of incident light with a targeting wavelength and hence enhances the absorption at that wavelength. In addition, the in-plane carrier mobility of the MoS₂ layer is much larger than the out-plane carrier mobility, which shortens the transit time of photoexcited carriers between two electrodes. As a result, a high specific detectivity of \approx 10¹³ Jones and a short response time of \approx 3 μs were realized at an NIR wavelength of 0.808 μm at room temperature, as shown in Figure 11h,i. In addition to the vertically stacked structures, other types of 2D materials have also been integrated with bulk Si to form coplanar vdW heterostructures for high-performance IR photodetection, including graphene and WS₂.^[11,190] Besides the aforementioned 2D materials, bulk Ge,^[8] GaAs,^[191] and AuO_x^[192] have also been used to construct 2D material-based mix-dimensional heterojunctions for photodetection at different IR wavelengths.

8. 2D Material-Based IR Photodetectors Integrated with Nanophotonic Structures

Though the volume-dependent thermal noise can be greatly reduced by using ultrathin materials in photodetectors, the performance of 2D material-based IR photodetectors is limited

by the low light absorption. To overcome this limitation, the integration with optical nanostructures has been employed in many IR photodetectors. Optical nanostructures including plasmonic nanostructures, dielectric nanostructures, and graphene nanostructures will be summarized in this section. For readers' reference, key figures-of-merit of some 2D material-based IR photodetectors integrated with nanophotonic structures are listed in Table 2.

8.1. 2D Material-Based IR Photodetectors Integrated with Plasmonic Metal Nanostructures

Metallic nanostructures are capable of supporting surface plasmon waves upon excitation by an optical illumination. The plasmon resonance frequency can be tuned by controlling the geometric parameters of these nanostructures.^[118,119,193–195] Recently, Jeong et al. prepared colloidal copper nanorods whose aspect ratios varied from 2.8 to 13.1 by using a heterometallic seed-mediated growth method. The longitudinal surface plasmon resonances of these different copper nanorods were located in the spectral region from 0.76 to 2.2 μm .^[118] According to Jensen et al.'s report, by carefully controlling the lithographic process, the longitudinal surface plasmon resonance wavelength of silver nanoparticle arrays with different size, height, and shape was tuned from \approx 0.4 to 6 μm .^[119] The metallic nanostructures not only confined the electromagnetic field at sub-wavelength scales but also transferred the energy of incident photons to high energy electrons (i.e., hot electrons) through the excitation and decay of surface plasmons.^[121,122,196–198] These hot carriers can be transferred to the conduction band of the 2D materials in contact with the metallic nanostructures, which could be leveraged to induce photoresponse in

IR photodetectors combining 2D materials and metallic nanostructures. In addition, since metal electrodes are commonly used in IR photodetectors, they could be conveniently designed into nanoantennas to enhance the light–matter interactions in 2D materials. Those electrodes could also improve the photo-carrier collection efficiency at the same time.^[39,45] In addition, it is convenient to fabricate metallic nanostructures at a relatively low cost by either physical or chemical methods.^[199–201]

The metallic nanostructures are commonly made of noble metals.^[38,202–204] Azar et al. put forward a “Nanoantennas and Grating” structure, which significantly enhanced the electromagnetic field intensity around the 2D materials by coupling the incident optical fields into surface plasmon modes down to subwavelength scale in the lateral dimensions.^[41] This nanostructure consisted of a metallic bull’s eye grating and an aperture made up of an array of nanoantennas, which is shown in **Figure 12a**. The bull’s eye grating collected the incident light and coupled it into SPPs. According to the simulation result, the optical aperture increased the electric field intensity by two orders of magnitude in the near-field zone through LSPRs compared with the norm of the incident electric field. The combination of the diffraction grating and the optical apertures led to a total graphene absorption up to $\approx 0.36\%$ at a wavelength of $10.84\ \mu\text{m}$, as shown in **Figure 12b**, which was ≈ 558 times larger than the absorption of graphene without the plasmonics nanostructures. Finally, the “Nanoantennas and Grating” photodetector gave rise to a specific detectivity enhancement of ≈ 32 times by comparison with the same-area graphene without plasmonics. Plasmonic nanoantennas can also serve as electrodes to improve the photocarrier collection efficiency.^[39,205] Yao et al. reported a graphene-based IR photodetector. In that work, the metallic antennas were designed to improve the performance of the device in two aspects. First, the metallic nanoantennas improved the light absorption of graphene. In addition, these metallic nanostructures served as electrodes, which improved the photoconductive gain in this detector, as shown in **Figure 12c**. The simulated current density distribution showed a current pathway in the nanoantennas, which indicated the fact that the metallic antennas had lower resistance than the graphene sheet. This is because the Pd layer helped to reduce the contact resistance between the Au antenna with graphene, as shown in **Figure 12d**. The transit time of photo-carriers generated in the $\approx 100\ \text{nm}$ nanogap was shortened to subpicosecond and the collection efficiency was improved significantly. The wavelength-dependent photoresponse of this graphene detector and the electric field intensity enhancement are shown in **Figure 12e**. As can be seen, the maximum responsivity occurred at $\lambda = 4.45\ \mu\text{m}$, which is very close to the peak wavelength of the electric field enhancement spectrum. The decay of surface plasmons can generate hot electrons, which can contribute to the photogain of 2D material-based IR photodetectors in the sub-bandgap regime.^[40,204,206] For example, Wang et al. proposed a NIR photodetector that consisted of bilayer MoS_2 film and Au wires, decorated by nonresonant wires (NRWs) and resonant wires (RWs).^[40] The hot electrons with energy greater than the Schottky barrier between Au and MoS_2 were generated through nonradiative decay of surface plasmon resonance and then injected into the bilayer MoS_2 . Under optical excitation with horizontally polarized light, hot

electrons were mainly generated by the RWs as they support strong plasmonic resonances. In contrast, no plasmonic resonances were excited in the NRWs. Based on this mechanism, the photodetector showed a polarization-selective photoresponse. The photoresponsivity peak appeared at $\lambda = 1.12\ \mu\text{m}$ for a positive source–drain bias (0.6 V) and disappeared for a negative bias (–0.6 V). This phenomenon was explained by the energy band diagrams. For a positive bias of 0.6 V, the hot electrons generated by the RWs resonance were injected into the 2D material and resulted in a peak photoresponse. On the other hand, for a negative bias of –0.6 V, only the hot electrons generated by NRWs were injected into bilayer MoS_2 , resulting in a responsivity spectrum with no resonant feature. Under zero bias, hot electrons generated by RWs and NRWs drifted in opposite directions, resulting in a small photocurrent. Recently, Wei et al. have integrated graphene with noncentrosymmetric metallic nanoantennas to achieve an artificial bulk photovoltaic effect (BPVE).^[207] Based on the hot carrier-assisted photothermoelectric effect, photocurrent was generated under zero-bias at room temperature. With the help of the noncentrosymmetric nanoantennas design, the noise equivalent power was reduced down to $0.12\ \text{nW Hz}^{-1/2}$. Moreover, they have demonstrated a calibration-free three-port device, which can unambiguously detect the polarization angle of the incident light.

Metallic NPs arrays can also be used to improve the performance of 2D material-based IR photodetectors.^[208,209] The plasmonic resonance wavelength can be tuned by adjusting the sizes and shapes of the metallic nanoparticles.^[210] By depositing triangle-like Au nanoparticles with different trilateral sizes on the graphene, the response spectrum of SWIR photodetectors based on graphene could be tuned.^[208] In Chen et al.’s work, the triangle-like Au nanoparticles were made by first, transferring close-packed polystyrene (PS) sphere onto the SiO_2/Si substrate creating a triangle-like hole between every three PS spheres. Then, the gold film was deposited onto the PS spheres layer. After controlling the annealing time followed by the removing of the PS spheres, triangle-like Au nanoparticles with three kinds of lateral sizes were prepared, as shown in **Figure 12g**. **Figure 12f** depicts the wavelength-dependent transmission and absorption spectra by simulation. This figure clearly shows that the absorption of graphene–silicon heterojunction is tunable by controlling the lateral sizes of Au NPs. **Figure 12h** shows the wavelength-dependent photoresponse of the SWIR photodetector corresponding to the three patterns in **Figure 12g**. The photoresponse peaks at the plasmonic resonance of the triangle-like Au nanoparticles array. Based on this approach, the graphene-based SWIR photodetectors possess spectral selective photoresponse. By using the pulsed magnetron sputtering method, the Au nanoparticles can be deposited on the surface of MoS_2 to form an Au NPs/ MoS_2 heterostructure.^[209] The Au NPs can couple the incident light into LSPRs, thus enhancing the light absorption transfer into MoS_2 , leading to a significant performance enhancement for the MoS_2 -based NIR photodetector.

8.2. 2D Material-Based IR Photodetectors Integrated with Optical Microcavities

Another commonly used method to enhance the light-absorption of 2D materials is through integrating with optical microcavities

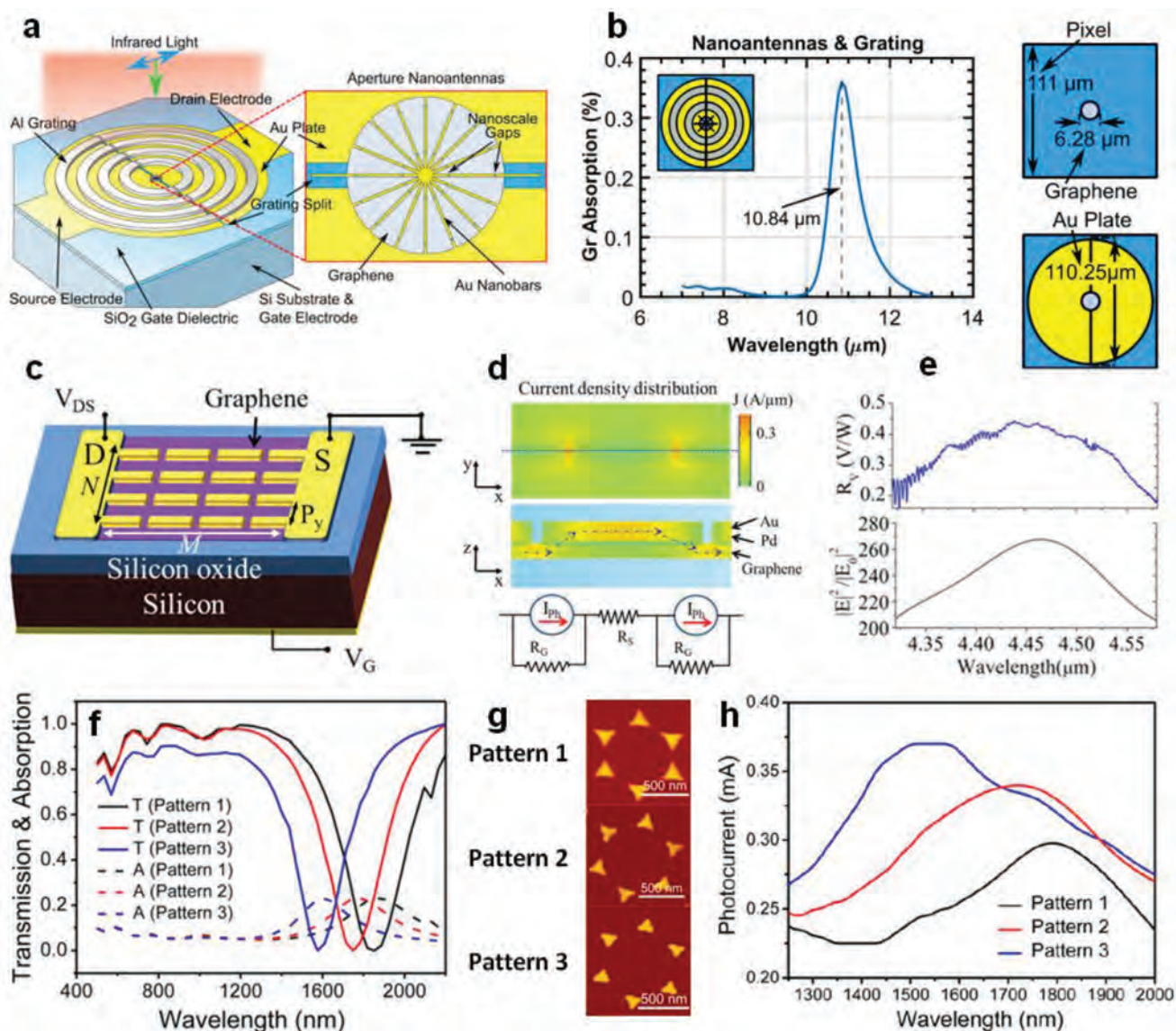


Figure 12. Using metal nanoantennas to improve the performance of 2D material-based IR photodetectors. a) Picture illustrating the “Nanoantennas and Grating” LWIR photodetector. b) Graphene absorption enhancement in the “Nanoantennas and Grating” architecture. Reproduced with permission.^[41] Copyright 2019, American Institute of Physics. c) A 3D schematic of the antenna-enhanced high-responsivity IR graphene photodetectors. d) Top view of the current density distribution in the graphene sheet (top). Side view of the current density distribution in the area around the Au antenna (middle). The equivalent circuit model of the antenna-enhanced graphene detector (bottom). e) Measured photoresponse spectrum of the antenna-assisted graphene detector (top). Simulated wavelength-dependent electric field intensity enhancement in the center of the nanogap (bottom). Reproduced with permission.^[39] Copyright 2014, American Chemical Society. Utilizing Au NP array to improve the performance of 2D material-based IR photodetectors. f) Simulation of transmission and absorption spectra of the graphene/silicon heterojunction decorated with Au NPs array. g) Triangle-like patterns 1, 2, and 3 are the morphology of Au NPs obtained by controlling the annealing time of monolayer PS spheres. h) Photoresponse spectrum of the graphene SWIR photodetector utilizing different triangle-like Au patterns. Reproduced with permission.^[208] Copyright 2017, American Chemical Society.

such as Fabry–Pérot cavities,^[43,211,212] planar photonic crystal (PPC) nanocavities,^[44,213–215] and optical cavity substrates.^[14,45,89]

The Fabry–Pérot cavity was formed by two distributed Bragg mirrors, which consisted of layers of materials with quarter-wavelength thickness and different refractive indices, as shown in **Figure 13a**.^[43] The graphene as an absorbing layer was located between the two mirrors. The materials selected to construct Bragg mirrors have no absorption at the detection wavelength due to their wide bandgaps.

By controlling the thicknesses of Bragg mirror layers at quarter wavelength, the reflectivity of the Bragg mirrors can reach unity, thus the energy of the optical field can be confined in the middle of the optical cavity where the graphene is located. The inset of **Figure 13a** shows the electric field distribution inside the cavity for normal incidence light.^[43] In Furchi et al.’s simulation, the electric field intensity has been enhanced by ≈6.5-fold, which improved the light–graphene interaction considerably. At the wavelength of 855 nm, which corresponds

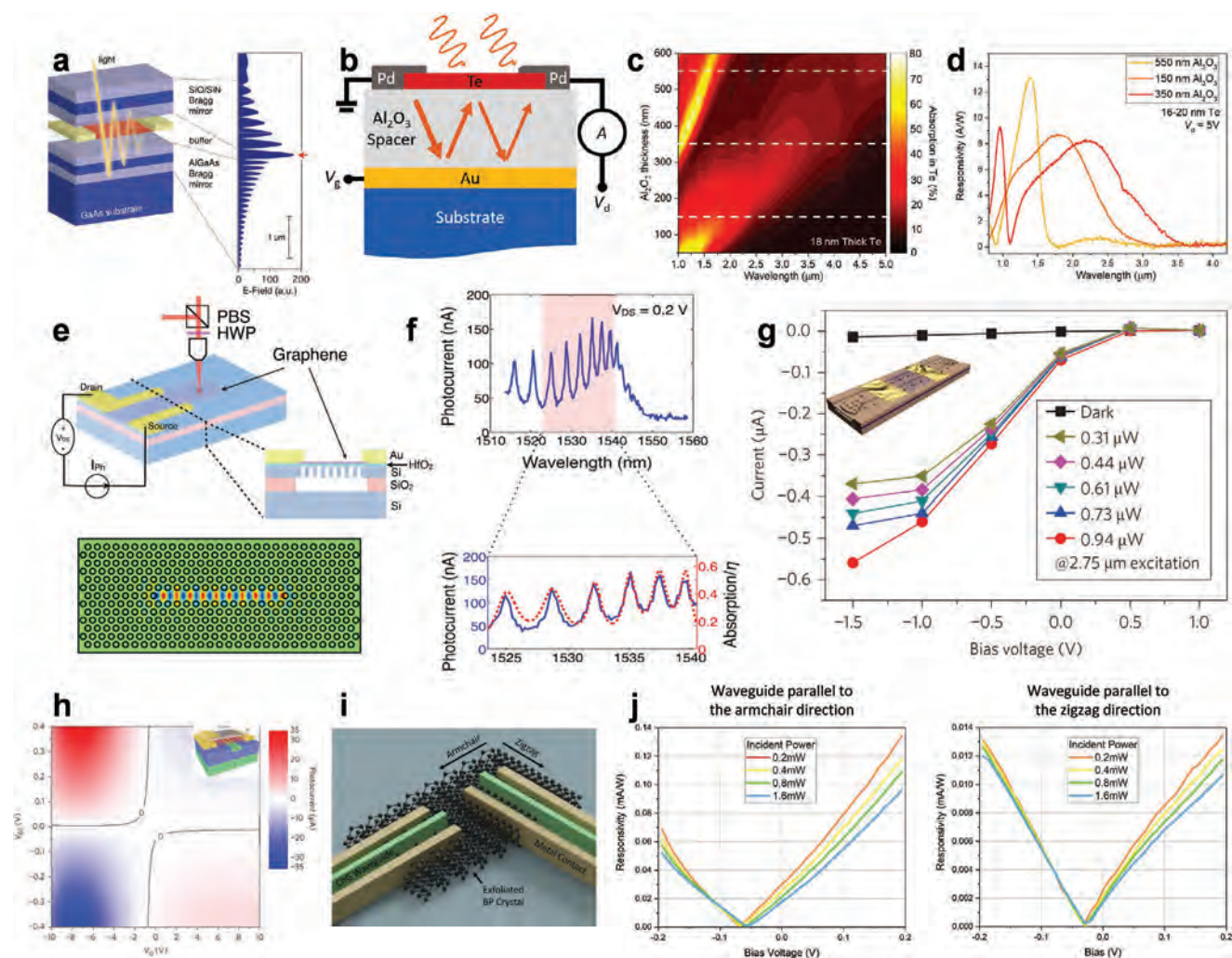


Figure 13. Enhancing the light absorption of 2D material-based IR photodetectors by integration with optical microcavities and cavity substrates. a) Graphene-based NIR photodetector integrated with Fabry–Pérot microcavity. The left-hand diagram shows the electric field distribution inside the cavity under normal light incidence. Reproduced with permission.^[43] Copyright 2012, American Chemical Society. b) Schematic of the Te nanoflake-based IR photodetector integrated with optical cavity substrates. c) Absorption heatmap of the Te layer as a function of wavelength and Al_2O_3 thickness given by theoretical calculation. d) Wavelength dependent responsivities of Te nanoflake fabricated on optical cavity substrates. Reproduced with permission.^[14] Copyright 2018, American Chemical Society. e) Schematic drawing of the graphene photodetector integrated with PPC cavity (top). The FDTD simulation of the localized resonant mode (bottom). f) The photocurrent spectra of the graphene photodetector. Reproduced with permission.^[44] Copyright 2013, American Institute of Physics. Layered 2D material-based IR photodetectors integrated with optical waveguides. g) Dark- and photocurrent varied with bias voltage under different incident lights. Inset is the schematic of the graphene/silicon-heterostructure waveguide photodetector. Reproduced with permission.^[3] Copyright 2013, Nature Publishing Group. h) The contour plot of the photocurrent of the device in the inset as a function of gate and bias voltages. Inset is the illustration of this BP-based IR photodetector integrated with silicon waveguide. Reproduced with permission.^[34] Copyright 2015, Nature Publishing Group. i) Schematic representation of the ChG waveguide-integrated BP-based IR photodetector. j) Photoresponsivities as a function of bias voltage in the cases of waveguide parallel to the armchair and the zigzag directions, respectively. Reproduced with permission.^[217] Copyright 2018, Institute of Physics.

to the cavity resonance, a 26-fold light-absorption enhancement for graphene has been achieved.

Compared with optical microcavities, a more convenient method from a fabrication standpoint to enhance the 2D material–light interaction is to transfer these 2D materials onto the optical cavity substrates. To enhance the light absorption of Te nanoflakes, an optical cavity substrate was used.^[14] The substrate consisted of a thick Au film that serves as a reflecting mirror and an Al_2O_3 dielectric spacer layer, as shown in Figure 13b. The light absorption in the Te was controlled by tuning the thickness

of the Al_2O_3 layer. Based on the calculated absorption of the Te nanoflake, a proper range of the Al_2O_3 thickness was determined for the target wavelength, as shown in Figure 13c. The photoresponsivity spectrum of the Te nanoflake-based IR photodetector was able to be tuned by changing the thickness of the Al_2O_3 spacer layer, which is shown in Figure 13d. Recently, Sefidmooye Azar et al. fabricated the photodetectors based on 2D PtSe_2 atop optical cavity substrates. The optical substrates consisted of TiO_2 spacer and Au mirror. These photodetectors presented a photoresponse with a time constant of 54 ns in the LWIR region.^[89]

Integrating with PPC nanocavities is another way to enhance the photodetection of the graphene-based photodetector. An air-suspended PPC was prepared via a top-down method and linear defects are introduced in the center of the PPC lattice, constituting the optical nanocavity. Finally, the light-absorbing material, i.e., monolayer graphene, which was prepared by mechanical exfoliation method, was transferred onto the cavity, as shown in the top inset in Figure 13e.^[44] The bottom inset shows the finite-difference time-domain (FDTD) simulation result of the optical field in the cavity. It is quite clear that the electromagnetic field is confined inside the PPC cavity. There are multiple spectral peaks occurring in the photocurrent spectrum, which correspond to different resonant modes of the PPC cavity. At the resonant wavelength of 1.535 μm , the photocurrent had an eightfold enhancement compared with that when the incident light is off the cavity resonance, as shown in Figure 13f.

8.3. 2D Material-Based IR Photodetectors Integrated with Optical Waveguides

Optical waveguides can improve the light absorption of 2D material-based IR photodetector by increasing the interaction distance between 2D materials and the light field.^[3,10,34,41,216,217] In the case of a 2D material-based photodetector illuminated by normal incident light, the optical absorption is limited by the atomic thickness of the 2D material. While in the case of a 2D material-based photodetector integrated with optical waveguides, the optical absorption by the 2D material could be improved by increasing the interaction length between the guided optical field and the 2D material.

The optical waveguides are usually fabricated on silicon-on-insulator (SOI) substrates. A graphene/silicon heterostructure waveguide photodetector with high-responsivity was reported by Wang et al. in 2013.^[3] The photodetector consisted of a graphene layer on a silicon optical waveguide on SOI, as shown in the inset in Figure 13g. A focusing subwavelength grating was used to couple the incident light from an optical fiber into the waveguide cavity. This device achieved good performance in the NIR range. Due to the existence of the heterostructure, the photocurrent-to-dark-current ratio was larger than 30. By integrating the graphene/silicon heterostructure with the waveguide, the graphene-based photodetector achieved a responsivity of 0.13 A W^{-1} at a bias voltage of 1.5 V bias for incident light at 2.75 μm at room temperature, as shown in Figure 13g.

In addition to graphene, bP has also been integrated with optical waveguides to construct IR photodetectors. Due to the finite bandgap of bP, the dark-current in bP-based optoelectronic devices are usually lower than that in graphene-based devices.^[218] A 23-layer bP-based IR photodetector integrated with a silicon photonic circuit has been reported by Youngblood et al., which is shown in the inset in Figure 13h.^[34] The silicon waveguide was used to enhance interaction between the optical field and the 2D material. A strong photovoltaic photocurrent was observed at low channel doping levels ($-10 \text{ V} < V_G < -1 \text{ V}$), whereas a weak bolometric photocurrent was observed at high channel doping levels ($V_G > 0 \text{ V}$), as shown in Figure 13h. When the bP was gated to a low doping level, the device exhibited

high responsivity, fast response, and low current, all of which are desirable for practical application.

The use of ChG allows the fabrication of MWIR waveguide-integrated bP detectors along different crystalline axes of bP.^[137,217] ChG is a broadband transparent material with high refractive indexes and offer good fabrication flexibility.^[219–221] Similar to 2D materials, ChG bonds to the substrate through van der Waals forces and can be easily deposited onto bP, serving both as a waveguide material and a passivation layer to prevent the bP degradation during the device fabrication process, as shown in Figure 13i.^[217] The photoresponse strongly depends on the orientation of the waveguide with respect to the crystalline axis of bP, that is the photoresponse was about one magnitude smaller when the waveguide is parallel to the zigzag direction of the bP than that when the waveguide is parallel to the armchair direction of the bP, as shown in Figure 13j. This phenomenon was explained by the in-plane anisotropic mobility and light absorption of bP. This means that, in designing bP-based optoelectronic devices, the crystalline orientation of bP must be considered.

Introducing defects in a planar photonic crystal is another strategy to realize the optical waveguides.^[136,222,223] Compared with the conventional slot waveguide, the photonic crystal defect waveguide design enables a larger gating area, resulting in a better photothermoelectric conversion for 2D material-based IR photodetectors. Taking the graphene photodetector integrated with an optical waveguide, for example, the responsivity was improved by approximately fourfold in the case of using a PhC defect waveguide compared to the case of using the slot waveguide.^[136] The PhC defect waveguide was fabricated by removing one row of holes in the photonic structure. Under zero bias, the PTE effect dominate the detection mechanism, and a maximum responsivity of 0.47 V W^{-1} was obtained. By applying a bias voltage V_{Bias} of 0.4 V, the maximum responsivity was increased to 0.17 A W^{-1} , because the fact that the photoconductive effect also contributed to the photoresponse.

8.4. IR Photodetectors Based on Graphene Plasmons

Due to the unique band structure of graphene, graphene support plasmons in the MWIR to THz region and is widely used in optoelectronic devices. Graphene plasmons have been explored to improve the photoresponsivity of graphene-based IR photodetectors.^[69,70,112,124,224–226] Moreover, graphene has great potential in developing optoelectronic switching devices because its plasmon modes can be tuned by applying a back-gate voltage.

A straightforward approach to excite graphene plasmons with optical fields is by patterning the graphene into periodic plasmonic metamaterials.^[125,126,227] Freitag et al. incorporated arrays of graphene nanoribbons into a graphene-based IR photodetector to support plasmonic resonances.^[125] The GNR was fabricated by patterning a PMMA mask with electron-beam lithography (EBL) followed by oxygen plasma etching, as shown in Figure 14a. The photocurrent was enhanced by using s-polarized light. Through the interaction of the graphene plasmons with surface polar phonons, long-lived hybrid plasmon–phonon modes were resulted. Then, the temperature of electrons and

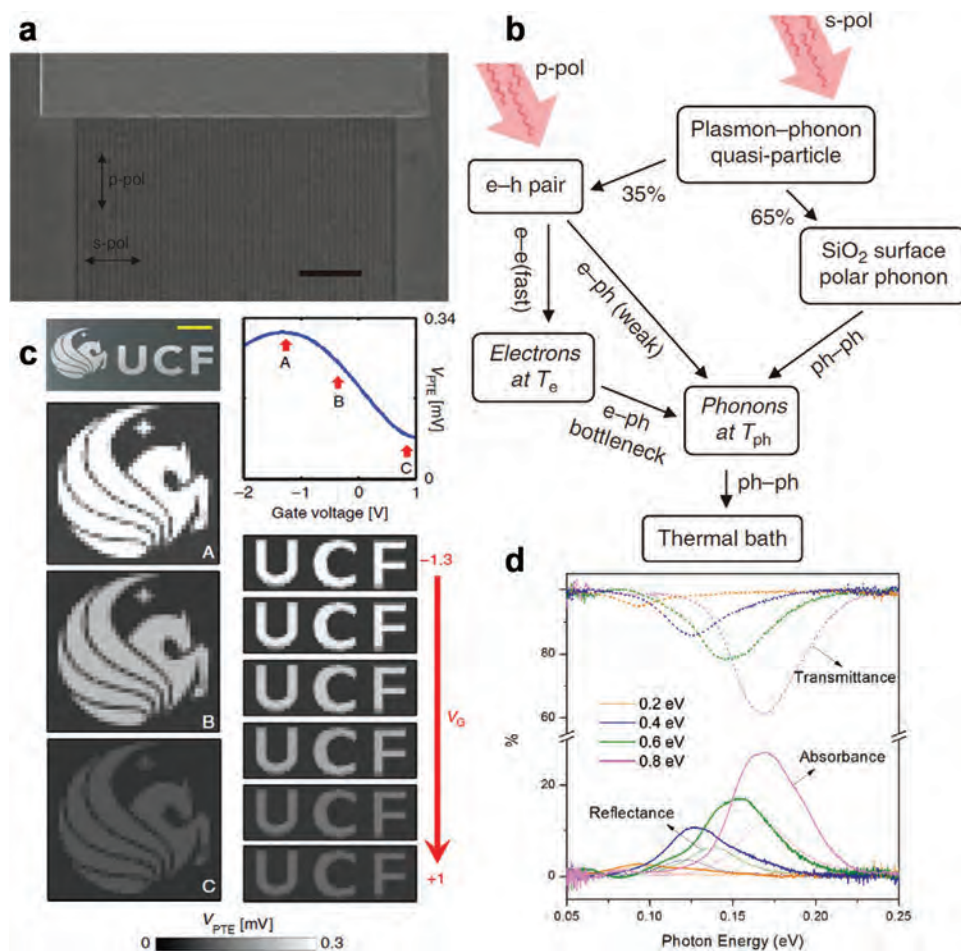


Figure 14. Light–graphene interaction enhancement by graphene plasmons. a) Scanning electron microscopy of the contact area of a GNR array photodetector. b) Illustration of the mechanism of phonon and hot electron generation through decay of the hybrid plasmon–phonon quasi-particles in the cases of s-polarized and p-polarized IR light. Reproduced with permission.^[125] Copyright 2013, Nature Publishing Group. c) IR imaging obtained using the multispectral gate tunable asymmetric graphene-based IR photodetector. Reproduced with permission.^[104] Copyright 2019, Nature Publishing Group. d) Spectra of transmittance, reflectance, and absorbance for graphene nanodisk arrays measured by Fourier transform IR spectrometer. Reproduced with permission.^[228] Copyright 2014, American Chemical Society.

phonons in graphene increased via the decay of the plasmon–phonon modes, resulting in a change in the electrical conductivity and leading to an enhancement of the photocurrent, as shown in Figure 14b. Due to the existence of the GNR superlattice, the graphene-based IR photodetector exhibited an enhancement factor that is an order of magnitude larger than the case with excitation of electron–hole pairs alone.

Patterning the graphene into nanodisk arrays can also excite surface plasmon modes and enhance the light–graphene interaction.^[228–230] In a typical device integrated with graphene nanodisk, the monolayer graphene was transferred onto an In–In₂O₃/BaF₂ substrate, which had no absorption in the 3–12 μm range, and then patterned into nanodisk arrays using EBL.^[228] The patterned graphene sheet absorbed ≈28% of the incident light at $h\nu = 0.17$ eV (wavelength ≈7.2 μm), which was much higher than the absorption for the unpatterned monolayer graphene, as shown in Figure 14d. Based on the plasmon-induced hot-carrier Seebeck effect, a high-performance graphene-based IR photodetector with a short response time (approximately ns) and high specific detectivity (≈10⁹ Jones) has also been

constructed.^[104] Safaei et al. designed a photodetector making use of the asymmetric graphene channel that is only half of the graphene was patterned into a hexagonal array of holes. This asymmetric graphene device was used to demonstrate gate-tunable multispectral imaging, which showed a performance comparable to commercial cameras, as shown in Figure 14c.

9. Large-Scale Array Integration for 2D Material-Based IR Photodetectors

For 2D material-based IR photodetectors, their monolithic integration of large-scale arrays with readout electronics is extremely critical for IR imaging applications, such as target tracking, biomedical diagnostics, and environmental monitoring.^[231] Given that 2D materials can be transferred onto almost any substrates, an array of IR photodetectors based on 2D materials could be potentially integrated with readout circuitry monolithically in a silicon die based on the highly matured CMOS technology.^[35] This CMOS-compatible approach simplifies fabrication and

thus holds cost-effectiveness. In this section, we introduce the recent developments of the monolithic integration of 2D material-based IR photodetectors and their large-scale arrays with CMOS technologies.

In their pioneering study, Pospischil et al. demonstrated a CMOS-compatible silicon waveguide-coupled graphene photoconductor, in which the graphene layer contacted with two ground electrodes (GND electrodes) was sandwiched between the gate electrode (S electrode) and the silicon waveguide covered with a ≈ 7 nm thick SiO₂ film on a SiO₂/Si substrate, as shown in Figure 15a.^[232] By optimizing the width (W) of the silicon waveguide and the length (L) of the device, the incident light was confined to and propagate inside the waveguide, thus allowing for strong light absorption by the graphene layer. Note that for the GND–S–GND configuration, the photocurrent driven by the local potential gradient between the GND and S electrodes was twice of that in a GND–S configuration. In addition, the carriers passing through the zero-bandgap graphene were unblocked, which led to a broad operation bandwidth of photodetectors. Using this approach, a room-temperature responsivity of 0.03 A W^{-1} was acquired at a wavelength of $1.55 \mu\text{m}$ in the best device with trilayer graphene. The estimated internal quantum efficiency was $\approx 10\%$. More importantly, the photodetector achieved a large bandwidth of $\approx 18 \text{ GHz}$. This work demonstrated the feasibility of the monolithic integration of a large-scale graphene photodetector array by the realization of a high-speed graphene IR photoconductor made from fully CMOS-compatible materials. More recently, Goossens et al. reported a broadband IR image sensor, which was composed of a 388×288 array of graphene-based IR photodetectors integrated monolithically with a CMOS readout circuitry, as shown in Figure 15b.^[35] By coating the graphene layer with a film of PbS QDs as shown in Figure 15c, the graphene photoconductor exhibited a considerable photoconductive gain of 10^8 as well as a responsivity higher than 10^7 A W^{-1} . This sensitive photoresponse was due to the fact that the photogenerated holes in PbS QDs were transferred to the graphene channel recirculated many times under an external bias, i.e., a photoconductive gain. More importantly, the graphene-based IR image sensor realized multiple functions by the integration with CMOS readout circuitry, including the amplification of photosignals and their readout from each pixel. These functions are important in real imaging applications. Based on the reflection imaging configuration as shown in Figure 15d, the authors demonstrated experimentally the capability of the CMOS–graphene image sensor to capture SWIR images that cannot be obtained by current silicon-based technologies. The imaging process is as follows. When the object was illuminated by IR light containing SWIR wavelengths ranging from 1.1 to $1.85 \mu\text{m}$, the reflected IR light gets detected by the CMOS–graphene image sensor packaged in a prototype camera with lens components. The IR image of the object was obtained by postprocessing the output signals from all pixels, as shown in Figure 15e. The objects were identified as pear and apple by their clear profile of IR images. Very recently, Tan et al. fabricated a 42×42 focal plane array (FPA) consisted of Se_{0.32}Te_{0.68} IR photoconductors, with a pixel size of $80 \mu\text{m} \times 90 \mu\text{m}$.^[45] The pixels of the FPA exhibited a

narrow distribution in photoresponsivity measured at a wavelength of $1.4 \mu\text{m}$, as shown in Figure 15f. Good uniformity in dark current was also observed in this FPA, with a value ranging from 170 to 220 nA , as shown in Figure 15g. Benefiting from the good uniformity in the responsivity and dark current, the IR image of a white light spot was captured well by the Se_{0.32}Te_{0.68}-based FPA based on a configuration with focusing lens, as shown in Figure 15h. It should be noted that the preparation of the Se_{0.32}Te_{0.68} thin film was done using a simple deposition method (i.e., thermal evaporation), providing opportunities for large scale, high uniformity, and low-cost fabrication. In addition, all 1764 pixels in the IR FPA were functional, corresponding to a yield of 100%. Therefore, the Se_{0.32}Te_{0.68} thin film holds promise for the fabrication of high-performance IR imaging sensors capable of monolithic integration with CMOS readout circuits.

10. Conclusions and Outlooks

In this review, we have summarized the current status of IR photodetectors based on emerging 2D materials and nanophotonics. Based on the device configurations, these 2D material-based IR photodetectors can be roughly classified into three categories, namely, photoconductors, photodiodes, and nanophotonic structure-integrated photodetectors. Among the three classes of IR photodetectors based on 2D materials, photoconductors are the most commonly studied due to their ease of fabrication. Graphene-based photoconductors have exhibited a large bandwidth up to a few tens of GHz,^[32] demonstrating their possible usage in high-speed applications. Owing to the existence of p–n junctions, photodiodes combining different 2D materials also showed good performance in terms of photoresponsivity and noise. For example, room-temperature detectivities of higher than 10^{10} Jones have been realized in these 2D material-based photodiodes (e.g., MoS₂/bP) in the MWIR regime.^[7] As compared to 2D material-based photodetectors without nanophotonic designs, the photodetectors integrated with optical nanostructures have exhibited enhanced performance both in terms of responsivity and specific detectivity since these optical nanostructures can simultaneously increase light absorption in 2D materials.

Although much progress has been made in exploring IR photodetectors based on 2D materials and nanophotonics, there are still some challenges remaining in this field. 1) Owing to the limitation of material bandgaps, the operating wavelength of most current 2D material-based IR photodetectors is limited in the SWIR and MWIR regimes, and only a few 2D materials (e.g., b-P_xAs_{1-x}, graphene, and PtSe₂) can realize LWIR/FIR detections, which are important for applications such as thermal imaging and biosensing. 2) Some key figures-of-merits of photodetectors, such as responsivity, specific detectivity, and response time, have been widely used to characterize 2D material-based IR photodetectors. However, most of these performance characterizations are only carried out under illumination at a single wavelength, which leads to the lack of spectral information and thus does not provide comprehensive characterization data needed for the further optimization of device performance. 3) We also note that many of the results reported

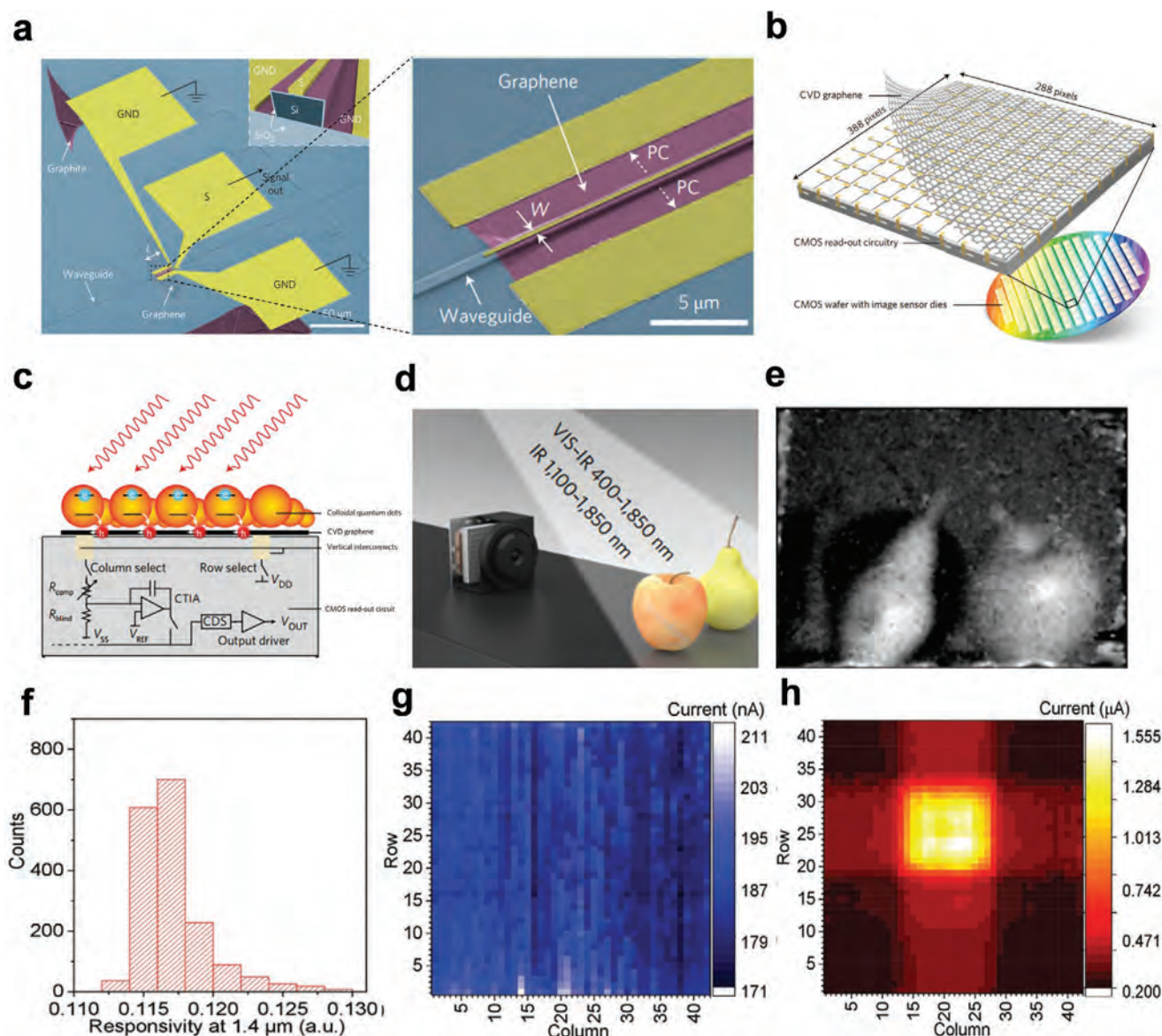


Figure 15. a) Colored SEM image of a CMOS-compatible graphene IR photodetector integrated with the Si waveguide. Reproduced with permission.^[232] Copyright 2013, Nature Publishing Group. b) Schematic of an IR image sensor chip, which consists of the pixel array of 388×288 CVD-growth graphene photodetectors and CMOS readout circuitry. c) Cross-sectional schematic of a quantum-dot-sensitized graphene photodetector in panel (a) and its underlying readout circuit. d) Set-up of reflection imaging using a digital camera made by the IR sensor chip in panel (b). e) The NIR-SWIR light photograph of an apple and pear captured with the reflection imaging configuration in panel (c). Reproduced with permission.^[35] Copyright 2017, Nature Publishing Group. f) Histogram of the responsivity of all pixels in the $\text{Se}_{0.32}\text{Te}_{0.68}$ FPA under $1.4 \mu\text{m}$ SWIR illumination. g) Intensity of the dark current as a function of the row and column number for the FPA in panel (f). h) FPA-captured IR image of the white light beam focused on its surface. Reproduced with permission.^[45] Copyright 2020, John Wiley & Sons, Inc.

thus far for 2D material-based IR photodetectors were obtained with laser illumination. While some of these results are comparable to what can be obtained with conventional IR detectors based on HgCdTe, the use of laser illumination makes one wonder about how applicable these devices would for real world applications. The use of blackbody illumination would address this, but this is only rarely used with 2D material-based IR photodetectors. On the other hand, large-scale arrays of detectors with supporting circuitry (e.g., for optoelectronic conversion and electrical signal processing) are rarely reported. This

is since the fact that the preparation of 2D materials commonly rely on mechanical exfoliation, which is hard to produce large-area and uniform 2D materials.

Considering the fact that the field of 2D material-based IR photodetector is still in its infancy, a variety of research directions could be pursued to advance the field in the near future as listed below. 1) Semiconductor alloys, made by different elements with varying composition (e.g., $\text{In}_x\text{Ga}_{1-x}\text{P}$),^[233,234] have exhibited a wide range of bandgaps. But traditional semiconductor alloys often require complex growth technologies

due to their extremely small tolerance to lattice mismatch. Since nanoscale 2D materials possess a large tolerance to lattice mismatch, their alloys can be readily formed by adjusting the composition of each element, offering an opportunity for bandgap engineering. Therefore, it is a promising research direction to investigate 2D material-based alloys with narrow bandgaps that cover spectral regions from the LWIR to the FIR. 2) Some of the 2D materials (e.g., MoS₂) have been grown by CVD methods, which could provide large-area and uniform samples.^[235,236] However, the CVD growth method has rarely been employed to prepare 2D materials that are suitable for IR photodetectors. Therefore, the exploration of CVD methods to synthesize 2D materials used for IR photodetectors could be another fruitful research direction. 3) For practical applications, photodetectors should possess high performance in terms of specific aspects, such as responsivity, spectral range, response speed, and specific detectivity. However, a systematic characterization of the performance of photodetectors is rarely carried out for 2D material-based IR photodetectors. The performance of most 2D material-based IR photodetectors is only assessed at a single wavelength, which provides no information of spectral response. Consequently, the third research direction is a more comprehensive characterization of the performance of 2D material-based IR photodetectors. 4) In principle, optical nanostructures (e.g., optical waveguides and cavities), which are made of metal and/or dielectric materials, can be integrated with arbitrary 2D materials to enhance their light absorption at specific wavelengths. However, the majority of reported 2D material-based IR photodetectors did not adopt these optical schemes for further performance improvement. Hence, the fourth research direction could be to integrate optical nanostructures into 2D material-based IR photodetectors to achieve higher performance. 5) In imaging applications, fabrication of a large-scale photodetector array integrated with readout modules is essential. But owing to issues including the lack of large-area growth methods and non-CMOS-compatible fabrication steps, the demonstration of 2D material-based IR photodetectors is generally based on a single-pixel device. Therefore, the fifth research direction could be to explore relevant integration techniques for the fabrication of large-scale 2D material-based IR photodetector arrays suitable for IR imaging tasks.

Acknowledgements

J.Z. and M.L. contributed equally to this work. C.T. thanks the funding support from the Start-Up Grant (Project No. 9610495) from the City University of Hong Kong, ECS scheme (CityU 21201821) from the Research Grant Council of Hong Kong and the National Natural Science Foundation of China (52122002). This work was also supported in part by the Australian Research Council (ARC) Centre of Excellence for Transformative Meta-Optical Systems (Project ID CE200100010) and by the ARC Discovery Projects scheme (DP210103428).

Conflict of Interest

The authors declare no conflict of interest.

Keywords

2D materials, heterojunctions, infrared, nanophotonics, photodetectors

Received: November 30, 2021

Published online:

- [1] G. Rao, X. Wang, Y. Wang, P. Wangyang, C. Yan, J. Chu, L. Xue, C. Gong, J. Huang, J. Xiong, Y. Li, *InfoMat* **2019**, 1, 272.
- [2] C. Yin, C. Gong, J. Chu, X. Wang, C. Yan, S. Qian, Y. Wang, G. Rao, H. Wang, Y. Liu, X. Wang, J. Wang, W. Hu, C. Li, J. Xiong, *Adv. Mater.* **2020**, 32, 2002237.
- [3] X. Wang, Z. Cheng, K. Xu, H. K. Tsang, J.-B. Xu, *Nat. Photonics* **2013**, 7, 888.
- [4] N. Huo, S. Gupta, G. Konstantatos, *Adv. Mater.* **2017**, 29, 1606576.
- [5] F. Wang, Y. Zhang, Y. Gao, P. Luo, J. Su, W. Han, K. Liu, H. Li, T. Zhai, *Small* **2019**, 15, 1901347.
- [6] Y. Fang, Y. Ge, C. Wang, H. Zhang, *Laser Photonics Rev.* **2019**, 14, 1900098.
- [7] J. Bullock, M. Amani, J. Cho, Y.-Z. Chen, G. H. Ahn, V. Adinolfi, V. R. Shrestha, Y. Gao, K. B. Crozier, Y.-L. Chueh, A. Javey, *Nat. Photonics* **2018**, 12, 601.
- [8] L. H. Zeng, M. Z. Wang, H. Hu, B. Nie, Y. Q. Yu, C. Y. Wu, L. Wang, J. G. Hu, C. Xie, F. X. Liang, L. B. Luo, *ACS Appl. Mater. Interfaces* **2013**, 5, 9362.
- [9] L. B. Luo, Y. F. Zou, C. W. Ge, K. Zheng, D. D. Wang, R. Lu, T. F. Zhang, Y. Q. Yu, Z. Y. Guo, *Adv. Opt. Mater.* **2016**, 4, 763.
- [10] L. Huang, B. Dong, X. Guo, Y. Chang, N. Chen, X. Huang, W. Liao, C. Zhu, H. Wang, C. Lee, K. W. Ang, *ACS Nano* **2019**, 13, 913.
- [11] E. Wu, D. Wu, C. Jia, Y. Wang, H. Yuan, L. Zeng, T. Xu, Z. Shi, Y. Tian, X. Li, *ACS Photonics* **2019**, 6, 565.
- [12] C. H. Liu, Y. C. Chang, T. B. Norris, Z. Zhong, *Nat. Nanotechnol.* **2014**, 9, 273.
- [13] M. Long, Y. Wang, P. Wang, X. Zhou, H. Xia, C. Luo, S. Huang, G. Zhang, H. Yan, Z. Fan, X. Wu, X. Chen, W. Lu, W. Hu, *ACS Nano* **2019**, 13, 2511.
- [14] M. Amani, C. Tan, G. Zhang, C. Zhao, J. Bullock, X. Song, H. Kim, V. R. Shrestha, Y. Gao, K. B. Crozier, M. Scott, A. Javey, *ACS Nano* **2018**, 12, 7253.
- [15] L. Ye, H. Li, Z. Chen, J. Xu, *ACS Photonics* **2016**, 3, 692.
- [16] M. Long, A. Gao, P. Wang, H. Xia, C. Ott, C. Pan, Y. Fu, E. Liu, X. Chen, W. Lu, T. Nilges, J. Xu, X. Wang, W. Hu, F. Miao, *Sci. Adv.* **2017**, 3, e1700589.
- [17] J. Wang, H. Fang, X. Wang, X. Chen, W. Lu, W. Hu, *Small* **2017**, 13, 1700894.
- [18] F. Yan, Z. Wei, X. Wei, Q. Lv, W. Zhu, K. Wang, *Small Methods* **2018**, 2, 1700349.
- [19] J. Yin, Z. Tan, H. Hong, J. Wu, H. Yuan, Y. Liu, C. Chen, C. Tan, F. Yao, T. Li, Y. Chen, Z. Liu, K. Liu, H. Peng, *Nat. Commun.* **2018**, 9, 3311.
- [20] M. Ye, J. Zha, C. Tan, K. B. Crozier, *Appl. Phys. Rev.* **2021**, 8, 031303.
- [21] F. Xia, H. Wang, D. Xiao, M. Dubey, A. Ramasubramaniam, *Nat. Photonics* **2014**, 8, 899.
- [22] M. Long, P. Wang, H. Fang, W. Hu, *Adv. Funct. Mater.* **2019**, 29, 1803807.
- [23] J. Cheng, C. Wang, X. Zou, L. Liao, *Adv. Opt. Mater.* **2019**, 7, 1800441.
- [24] N. Huo, G. Konstantatos, *Adv. Mater.* **2018**, 30, 1801164.
- [25] A. K. Geim, I. V. Grigorieva, *Nature* **2013**, 499, 419.
- [26] F. H. Koppens, T. Mueller, P. Avouris, A. C. Ferrari, M. S. Vitiello, M. Polini, *Nat. Nanotechnol.* **2014**, 9, 780.
- [27] Z. Ni, L. Ma, S. Du, Y. Xu, M. Yuan, H. Fang, Z. Wang, M. Xu, D. Li, J. Yang, W. Hu, X. Pi, D. Yang, *ACS Nano* **2017**, 11, 9854.

- [28] H. Liu, X. Zhu, X. Sun, C. Zhu, W. Huang, X. Zhang, B. Zheng, Z. Zou, Z. Luo, X. Wang, D. Li, A. Pan, *ACS Nano* **2019**, *13*, 13573.
- [29] X. Chen, X. Lu, B. Deng, O. Sinai, Y. Shao, C. Li, S. Yuan, V. Tran, K. Watanabe, T. Taniguchi, D. Naveh, L. Yang, F. Xia, *Nat. Commun.* **2017**, *8*, 1672.
- [30] M. J. Grotevent, C. U. Hail, S. Yakunin, D. N. Dirin, K. Thodkar, G. Borin Barin, P. Guyot-Sionnest, M. Calame, D. Poulidakos, M. V. Kovalenko, I. Shorubalko, *Adv. Opt. Mater.* **2019**, *7*, 1900019.
- [31] H. Huang, J. Zha, S. Li, C. Tan, *Chin. Chem. Lett.* **2021**, <https://doi.org/10.1016/j.ccllet.2021.06.004>.
- [32] F. Xia, T. Mueller, Y. M. Lin, A. Valdes-Garcia, P. Avouris, *Nat. Nanotechnol.* **2009**, *4*, 839.
- [33] A. Pezeshki, S. H. Shokouh, T. Nazari, K. Oh, S. Im, *Adv. Mater.* **2016**, *28*, 3216.
- [34] N. Youngblood, C. Chen, S. J. Koester, M. Li, *Nat. Photonics* **2015**, *9*, 247.
- [35] S. Goossens, G. Navickaite, C. Monasterio, S. Gupta, J. J. Piqueras, R. Pérez, G. Burwell, I. Nikitskiy, T. Lasanta, T. Galán, E. Puma, A. Centeno, A. Pesquera, A. Zurutuza, G. Konstantatos, F. Koppens, *Nat. Photonics* **2017**, *11*, 366.
- [36] H. Wang, S. Li, R. Ai, H. Huang, L. Shao, J. Wang, *Nanoscale* **2020**, *12*, 8095.
- [37] L. Tao, Z. F. Chen, Z. Y. Li, J. Q. Wang, X. Xu, J. B. Xu, *InfoMat* **2021**, *3*, 36.
- [38] Z. Fang, Z. Liu, Y. Wang, P. M. Ajayan, P. Nordlander, N. J. Halas, *Nano Lett.* **2012**, *12*, 3808.
- [39] Y. Yao, R. Shankar, P. Rauter, Y. Song, J. Kong, M. Loncar, F. Capasso, *Nano Lett.* **2014**, *14*, 3749.
- [40] W. Wang, A. Klotz, F. Prasai, Y. Yang, K. I. Bolotin, J. Valentine, *Nano Lett.* **2015**, *15*, 7440.
- [41] N. S. Azar, V. R. Shrestha, K. B. Crozier, *Appl. Phys. Lett.* **2019**, *114*, 091108.
- [42] R. Kumar, A. Sharma, M. Kaur, S. Husale, *Adv. Opt. Mater.* **2017**, *5*, 1700009.
- [43] M. Furchi, A. Urich, A. Pospischil, G. Lilley, K. Unterrainer, H. Detz, P. Klang, A. M. Andrews, W. Schrenk, G. Strasser, T. Mueller, *Nano Lett.* **2012**, *12*, 2773.
- [44] R. J. Shiue, X. T. Gan, Y. D. Gao, L. Z. Li, X. W. Yao, A. Szep, D. Walker, J. Hone, D. Englund, *Appl. Phys. Lett.* **2013**, *103*, 241109.
- [45] C. Tan, M. Amani, C. Zhao, M. Hettick, X. Song, D.-H. Lien, H. Li, M. Yeh, V. R. Shrestha, K. B. Crozier, M. C. Scott, A. Javey, *Adv. Mater.* **2020**, *32*, 2001329.
- [46] X. Gan, R.-J. Shiue, Y. Gao, I. Meric, T. F. Heinz, K. Shepard, J. Hone, S. Assefa, D. Englund, *Nat. Photonics* **2013**, *7*, 883.
- [47] Y. Liu, N. O. Weiss, X. Duan, H.-C. Cheng, Y. Huang, X. Duan, *Nat. Rev. Mater.* **2016**, *1*, 16042.
- [48] K. S. Novoselov, A. Mishchenko, A. Carvalho, A. H. C. Neto, *Science* **2016**, *353*, aac9439.
- [49] X. Wang, F. Xia, *Nat. Mater.* **2015**, *14*, 264.
- [50] G. Simone, M. J. Dyson, C. H. L. Weijtens, S. C. J. Meskers, R. Coehoorn, R. A. J. Janssen, G. H. Gelinck, *Adv. Opt. Mater.* **2020**, *8*, 1901568.
- [51] L. Britnell, R. M. Ribeiro, A. Eckmann, R. Jalil, B. D. Belle, A. Mishchenko, Y.-J. Kim, R. V. Gorbachev, T. Georgiou, S. V. Morozov, A. N. Grigorenko, A. K. Geim, C. Casiraghi, A. H. C. Neto, K. S. Novoselov, *Science* **2013**, *340*, 1311.
- [52] G. Eda, S. A. Maier, *ACS Nano* **2013**, *7*, 5660.
- [53] R. R. Nair, P. Blake, A. N. Grigorenko, K. S. Novoselov, T. J. Booth, T. Stauber, N. M. R. Peres, A. K. Geim, *Science* **2008**, *320*, 1308.
- [54] K. Tsakmakidis, *Nat. Mater.* **2013**, *12*, 688.
- [55] K. F. Mak, M. Y. Sfeir, Y. Wu, C. H. Lui, J. A. Misewich, T. F. Heinz, *Phys. Rev. Lett.* **2008**, *101*, 196405.
- [56] V. Tran, R. Soklaski, Y. Liang, L. Yang, *Phys. Rev. B* **2014**, *89*, 235319.
- [57] Z. Zhang, P. Chen, X. Duan, K. Zang, J. Luo, X. Duan, *Science* **2017**, *357*, 788.
- [58] Y.-C. Lin, R. K. Ghosh, R. Addou, N. Lu, S. M. Eichfeld, H. Zhu, M.-Y. Li, X. Peng, M. J. Kim, L.-J. Li, R. M. Wallace, S. Datta, J. A. Robinson, *Nat. Commun.* **2015**, *6*, 7311.
- [59] Y. Gong, J. Lin, X. Wang, G. Shi, S. Lei, Z. Lin, X. Zou, G. Ye, R. Vajtai, B. I. Yakobson, H. Terrones, M. Terrones, Beng K. Tay, J. Lou, S. T. Pantelides, Z. Liu, W. Zhou, P. M. Ajayan, *Nat. Mater.* **2014**, *13*, 1135.
- [60] A. Piotrowski, P. Madejczyk, W. Gawron, K. Kłós, J. Pawluczyk, J. Rutkowski, J. Piotrowski, A. Rogalski, *Infrared Phys. Technol.* **2007**, *49*, 173.
- [61] K. S. Novoselov, A. K. Geim, S. V. Morozov, D. Jiang, Y. Zhang, S. V. Dubonos, I. V. Grigorieva, A. A. Firsov, *Science* **2004**, *306*, 666.
- [62] C. Tan, X. Cao, X.-J. Wu, Q. He, J. Yang, X. Zhang, J. Chen, W. Zhao, S. Han, G.-H. Nam, M. Sindoro, H. Zhang, *Chem. Rev.* **2017**, *117*, 6225.
- [63] C. Tan, Z. Lai, H. Zhang, *Adv. Mater.* **2017**, *29*, 1701392.
- [64] C. Tan, H. Zhang, *Nat. Commun.* **2015**, *6*, 7873.
- [65] C. Chang, W. Chen, Y. Chen, Y. Chen, Y. Chen, F. Ding, C. Fan, H. Fan, Z. Fan, C. Gong, Y. Gong, Q. He, X. Hong, S. Hu, W. Hu, W. Huang, Y. Huang, W. Ji, D. Li, L. Li, Q. Li, L. Lin, C. Ling, M. Liu, N. Liu, Z. Liu, K. Loh, J. Ma, F. Miao, H. Peng, et al., *Acta Phys.-Chim. Sin.* **2021**, *37*, 2108017.
- [66] R. A. Hemnani, J. P. Tischler, C. Carfano, R. Maiti, M. H. Tahersima, L. Bartels, R. Agarwal, V. J. Sorger, *2D Mater.* **2019**, *6*, 015006.
- [67] F. Schwier, *Nat. Nanotechnol.* **2010**, *5*, 487.
- [68] H. T. Liu, Y. Q. Liu, D. B. Zhu, *J. Mater. Chem.* **2011**, *21*, 3335.
- [69] Q. S. Guo, C. Li, B. C. Deng, S. F. Yuan, F. Guinea, F. N. Xia, *ACS Photonics* **2017**, *4*, 2989.
- [70] A. N. Grigorenko, M. Polini, K. S. Novoselov, *Nat. Photonics* **2012**, *6*, 749.
- [71] G. Konstantatos, M. Badioli, L. Gaudreau, J. Osmond, M. Bernechea, F. P. Garcia de Arquer, F. Gatti, F. H. Koppens, *Nat. Nanotechnol.* **2012**, *7*, 363.
- [72] I. Nikitskiy, S. Goossens, D. Kufer, T. Lasanta, G. Navickaite, F. H. Koppens, G. Konstantatos, *Nat. Commun.* **2016**, *7*, 11954.
- [73] K. Zhang, T. Zhang, G. Cheng, T. Li, S. Wang, W. Wei, X. Zhou, W. Yu, Y. Sun, P. Wang, D. Zhang, C. Zeng, X. Wang, W. Hu, H. J. Fan, G. Shen, X. Chen, X. Duan, K. Chang, N. Dai, *ACS Nano* **2016**, *10*, 3852.
- [74] X. Hong, J. Kim, S.-F. Shi, Y. Zhang, C. Jin, Y. Sun, S. Tongay, J. Wu, Y. Zhang, F. Wang, *Nat. Nanotechnol.* **2014**, *9*, 682.
- [75] Z. L. Guo, N. H. Miao, J. Zhou, B. S. Sa, Z. Sun, *J. Mater. Chem. C* **2017**, *5*, 978.
- [76] H. P. Komsa, A. V. Krasheninnikov, *Phys. Rev. B* **2013**, *88*, 085318.
- [77] M. M. Furchi, A. Pospischil, F. Libisch, J. Burgdorfer, T. Mueller, *Nano Lett.* **2014**, *14*, 4785.
- [78] D. Kufer, I. Nikitskiy, T. Lasanta, G. Navickaite, F. H. L. Koppens, G. Konstantatos, *Adv. Mater.* **2015**, *27*, 176.
- [79] F. N. Xia, H. Wang, Y. C. Jia, *Nat. Commun.* **2014**, *5*, 4458.
- [80] H. T. Yuan, X. G. Liu, F. Afshinmanesh, W. Li, G. Xu, J. Sun, B. Lian, A. G. Curto, G. J. Ye, Y. Hikita, Z. X. Shen, S. C. Zhang, X. H. Chen, M. Brongersma, H. Y. Hwang, Y. Cui, *Nat. Nanotechnol.* **2015**, *10*, 707.
- [81] M. Amani, E. Regan, J. Bullock, G. H. Ahn, A. Javey, *ACS Nano* **2017**, *11*, 11724.
- [82] B. Deng, V. Tran, Y. Xie, H. Jiang, C. Li, Q. Guo, X. Wang, H. Tian, S. J. Koester, H. Wang, J. J. Cha, Q. Xia, L. Yang, F. Xia, *Nat. Commun.* **2017**, *8*, 14474.
- [83] H. Kim, S. Z. Uddin, D.-H. Lien, M. Yeh, N. S. Azar, S. Balendhran, T. Kim, N. Gupta, Y. Rho, C. P. Grigoropoulos, K. B. Crozier, A. Javey, *Nature* **2021**, *596*, 232.
- [84] B. L. Liu, M. Kopf, A. N. Abbas, X. M. Wang, Q. S. Guo, Y. C. Jia, F. N. Xia, R. Wehrich, F. Bachhuber, F. Pielhofer, H. Wang, R. Dhall, S. B. Cronin, M. Y. Ge, X. Fang, T. Nilges, C. W. Zhou, *Adv. Mater.* **2015**, *27*, 4423.

- [85] X. Yu, P. Yu, D. Wu, B. Singh, Q. Zeng, H. Lin, W. Zhou, J. Lin, K. Suenaga, Z. Liu, Q. J. Wang, *Nat. Commun.* **2018**, *9*, 1545.
- [86] G. Zhang, M. Amani, A. Chaturvedi, C. Tan, J. Bullock, X. Song, H. Kim, D.-H. Lien, M. C. Scott, H. Zhang, A. Javey, *Appl. Phys. Lett.* **2019**, *114*, 253102.
- [87] L.-H. Zeng, D. Wu, S.-H. Lin, C. Xie, H.-Y. Yuan, W. Lu, S. P. Lau, Y. Chai, L.-B. Luo, Z.-J. Li, Y. H. Tsang, *Adv. Funct. Mater.* **2019**, *29*, 1806878.
- [88] C. Yim, N. McEvoy, S. Riazimehr, D. S. Schneider, F. City, S. Monaghan, P. K. Hurley, M. C. Lemme, G. S. Duesberg, *Nano Lett.* **2018**, *18*, 1794.
- [89] N. Sefidmooye Azar, J. Bullock, V. R. Shrestha, S. Balendhran, W. Yan, H. Kim, A. Javey, K. B. Crozier, *ACS Nano* **2021**, *15*, 6573.
- [90] Y. X. Wang, G. Qiu, R. X. Wang, S. Y. Huang, Q. X. Wang, Y. Y. Liu, Y. C. Du, W. A. Goddard, M. J. Kim, X. F. Xu, P. D. Ye, W. Z. Wu, *Nat. Electron.* **2018**, *1*, 228.
- [91] C. Zhao, L. Hurtado, A. Javey, *Appl. Phys. Lett.* **2020**, *117*, 192104.
- [92] C. Zhao, C. Tan, D.-H. Lien, X. Song, M. Amani, M. Hettick, H. Y. Y. Nyein, Z. Yuan, L. Li, M. C. Scott, A. Javey, *Nat. Nanotechnol.* **2020**, *15*, 53.
- [93] J. Qiao, Y. Pan, F. Yang, C. Wang, Y. Chai, W. Ji, *Sci. Bull.* **2018**, *63*, 159.
- [94] H. Fang, W. Hu, *Adv. Sci.* **2017**, *4*, 1700323.
- [95] Z. Qiu, M. Trushin, H. Fang, I. Verzhbitskiy, S. Gao, E. Laksono, M. Yang, P. Lyu, J. Li, J. Su, M. Telychko, K. Watanabe, T. Taniguchi, J. Wu, A. H. C. Neto, L. Yang, G. Eda, S. Adam, J. Lu, *Sci. Adv.* **2019**, *5*, eaaw2387.
- [96] K. K. Manga, J. Wang, M. Lin, J. Zhang, M. Nesladek, V. Nalla, W. Ji, K. P. Loh, *Adv. Mater.* **2012**, *24*, 1697.
- [97] F. Gong, H. Fang, P. Wang, M. Su, Q. Li, J. C. Ho, X. Chen, W. Lu, L. Liao, J. Wang, W. Hu, *Nanotechnology* **2017**, *28*, 484002.
- [98] N. M. Gabor, J. C. W. Song, Q. Ma, N. L. Nair, T. Taychatanapat, K. Watanabe, T. Taniguchi, L. S. Levitov, P. Jarillo-Herrero, *Science* **2011**, *334*, 648.
- [99] X. Cai, A. B. Sushkov, R. J. Suess, M. M. Jadidi, G. S. Jenkins, L. O. Nyakiti, R. L. Myers-Ward, S. Li, J. Yan, D. K. Gaskill, T. E. Murphy, H. D. Drew, M. S. Fuhrer, *Nat. Nanotechnol.* **2014**, *9*, 814.
- [100] X. Lu, L. Sun, P. Jiang, X. Bao, *Adv. Mater.* **2019**, *31*, 1902044.
- [101] W. Guo, Z. Dong, Y. Xu, C. Liu, D. Wei, L. Zhang, X. Shi, C. Guo, H. Xu, G. Chen, L. Wang, K. Zhang, X. Chen, W. Lu, *Adv. Sci.* **2020**, *7*, 1902699.
- [102] M. Cutler, N. F. Mott, *Phys. Rev.* **1969**, *181*, 1336.
- [103] A. L. Hsu, P. K. Herring, N. M. Gabor, S. Ha, Y. C. Shin, Y. Song, M. Chin, M. Dubey, A. P. Chandrakasan, J. Kong, P. Jarillo-Herrero, T. Palacios, *Nano Lett.* **2015**, *15*, 7211.
- [104] A. Safaei, S. Chandra, M. W. Shabbir, M. N. Leuenberger, D. Chanda, *Nat. Commun.* **2019**, *10*, 3498.
- [105] P. L. Richards, *J. Appl. Phys.* **1994**, *76*, 1.
- [106] D. E. Carlson, G. Lin, G. Ganguly, in Proceedings of the 28th IEEE Photovoltaic Specialist Conf., IEEE, Piscataway, NJ **2000**, p. 707.
- [107] H. Xu, L. Hao, H. Liu, S. Dong, Y. Wu, Y. Liu, B. Cao, Z. Wang, C. Ling, S. Li, Z. Xu, Q. Xue, K. Yan, *ACS Appl. Mater. Interfaces* **2020**, *12*, 31.
- [108] M.-C. Luo, F.-F. Ren, N. Gagrani, K. Qiu, Q. Wang, L. Yu, J. Ye, F. Yan, R. Zhang, H. H. Tan, C. Jagadish, X. Ji, *Adv. Opt. Mater.* **2020**, *8*, 2000514.
- [109] J. Liu, F. Xia, D. Xiao, F. J. García de Abajo, D. Sun, *Nat. Mater.* **2020**, *19*, 830.
- [110] A. Rogalski, *Prog. Quantum Electron.* **2012**, *36*, 342.
- [111] A. Rogalski, *Prog. Quantum Electron.* **2003**, *27*, 59.
- [112] T. Low, P. Avouris, *ACS Nano* **2014**, *8*, 1086.
- [113] H. Li, Y. Anugrah, S. J. Koester, M. Li, *Appl. Phys. Lett.* **2012**, *101*, 111110.
- [114] J. A. Schuller, E. S. Barnard, W. S. Cai, Y. C. Jun, J. S. White, M. L. Brongersma, *Nat. Mater.* **2010**, *9*, 193.
- [115] W. H. Weber, G. W. Ford, *Opt. Lett.* **1981**, *6*, 122.
- [116] A. V. Zayats, I. I. Smolyaninov, A. A. Maradudin, *Phys. Rep.* **2005**, *408*, 131.
- [117] J. Z. Zhang, C. Noguez, *Plasmonics* **2008**, *3*, 127.
- [118] S. Jeong, Y. Liu, Y. Zhong, X. Zhan, Y. Li, Y. Wang, P. M. Cha, J. Chen, X. Ye, *Nano Lett.* **2020**, *20*, 7263.
- [119] T. R. Jensen, M. D. Malinsky, C. L. Haynes, R. P. Van Duyne, *J. Phys. Chem. B* **2000**, *104*, 10549.
- [120] J. Aizpurua, P. Hanarp, D. S. Sutherland, M. Käll, G. W. Bryant, F. J. García de Abajo, *Phys. Rev. Lett.* **2003**, *90*, 057401.
- [121] R. Sundararaman, P. Narang, A. S. Jermyn, W. A. Goddard3rd, H. A. Atwater, *Nat. Commun.* **2014**, *5*, 5788.
- [122] L. Li, W. Liu, A. Gao, Y. Zhao, Q. Lu, L. Yu, J. Wang, L. Yu, L. Shao, F. Miao, Y. Shi, Y. Xu, X. Wang, *Nano Lett.* **2019**, *19*, 3295.
- [123] R. Kolesov, B. Grotz, G. Balasubramanian, R. J. Stohr, A. A. L. Nicolet, P. R. Hemmer, F. Jelezko, J. Wrachtrup, *Nat. Phys.* **2009**, *5*, 470.
- [124] F. H. L. Koppens, D. E. Chang, F. J. G. de Abajo, *Nano Lett.* **2011**, *11*, 3370.
- [125] M. Freitag, T. Low, W. Zhu, H. Yan, F. Xia, P. Avouris, *Nat. Commun.* **2013**, *4*, 1951.
- [126] H. G. Yan, T. Low, W. J. Zhu, Y. Q. Wu, M. Freitag, X. S. Li, F. Guinea, P. Avouris, F. N. Xia, *Nat. Photonics* **2013**, *7*, 394.
- [127] Z. Fei, G. O. Andreev, W. Bao, L. M. Zhang, A. S. McLeod, C. Wang, M. K. Stewart, Z. Zhao, G. Dominguez, M. Thiemens, M. M. Fogler, M. J. Tauber, A. H. Castro-Neto, C. N. Lau, F. Keilmann, D. N. Basov, *Nano Lett.* **2011**, *11*, 4701.
- [128] Y. M. Qing, H. F. Ma, T. J. Cui, *ACS Photonics* **2019**, *6*, 2884.
- [129] K. J. Vahala, *Nature* **2003**, *424*, 839.
- [130] S. M. Spillane, T. J. Kippenberg, K. J. Vahala, *Nature* **2002**, *415*, 621.
- [131] S. L. McCall, A. F. J. Levi, R. E. Slusher, S. J. Pearton, R. A. Logan, *Appl. Phys. Lett.* **1992**, *60*, 289.
- [132] W. Noh, M. Dupre, A. Ndao, A. Kodigala, B. Kante, *ACS Photonics* **2019**, *6*, 389.
- [133] I. M. White, H. Oveys, X. D. Fan, *Opt. Lett.* **2006**, *31*, 1319.
- [134] E. J. R. Vesseur, F. J. G. de Abajo, A. Polman, *Nano Lett.* **2009**, *9*, 3147.
- [135] Z. P. Sun, A. Martinez, F. Wang, *Nat. Photonics* **2016**, *10*, 227.
- [136] S. Schuler, D. Schall, D. Neumaier, B. Schwarz, K. Watanabe, T. Taniguchi, T. Mueller, *ACS Photonics* **2018**, *5*, 4758.
- [137] H. T. Lin, Y. Song, Y. Z. Huang, D. Kita, S. Deckoff-Jones, K. Q. Wang, L. Li, J. Y. Li, H. Y. Zheng, Z. Q. Luo, H. Z. Wang, S. Novak, A. Yadav, C. C. Huang, R. J. Shiue, D. Englund, T. Gu, D. Hewak, K. Richardson, J. Kong, J. J. Hu, *Nat. Photonics* **2017**, *11*, 798.
- [138] X. Guo, W. Wang, H. Nan, Y. Yu, J. Jiang, W. Zhao, J. Li, Z. Zafar, N. Xiang, Z. Ni, W. Hu, Y. You, Z. Ni, *Optica* **2016**, *3*, 1066.
- [139] F. Bonaccorso, Z. Sun, T. Hasan, A. C. Ferrari, *Nat. Photonics* **2010**, *4*, 611.
- [140] T. Mueller, F. Xia, P. Avouris, *Nat. Photonics* **2010**, *4*, 297.
- [141] B. Chitara, L. S. Panchakarla, S. B. Krupanidhi, C. N. Rao, *Adv. Mater.* **2011**, *23*, 5419.
- [142] H. Chang, Z. Sun, M. Saito, Q. Yuan, H. Zhang, J. Li, Z. Wang, T. Fujita, F. Ding, Z. Zheng, F. Yan, H. Wu, M. Chen, Y. Ikuhara, *ACS Nano* **2013**, *7*, 6310.
- [143] S. Du, W. Lu, A. Ali, P. Zhao, K. Shehzad, H. Guo, L. Ma, X. Liu, X. Pi, P. Wang, H. Fang, Z. Xu, C. Gao, Y. Dan, P. Tan, H. Wang, C.-T. Lin, J. Yang, S. Dong, Z. Cheng, E. Li, W. Yin, J. Luo, B. Yu, T. Hasan, Y. Xu, W. Hu, X. Duan, *Adv. Mater.* **2017**, *29*, 1700463.
- [144] B. Y. Zhang, T. Liu, B. Meng, X. Li, G. Liang, X. Hu, Q. J. Wang, *Nat. Commun.* **2013**, *4*, 1811.
- [145] T. Deng, Z. Zhang, Y. Liu, Y. Wang, F. Su, S. Li, Y. Zhang, H. Li, H. Chen, Z. Zhao, Y. Li, Z. Liu, *Nano Lett.* **2019**, *19*, 1494.

- [146] B. Deng, C. Ma, Q. Wang, S. Yuan, K. Watanabe, T. Taniguchi, F. Zhang, F. Xia, *Nat. Photonics* **2020**, *14*, 549.
- [147] L. Yin, K. Xu, Y. Wen, Z. Wang, Y. Huang, F. Wang, T. A. Shifa, R. Cheng, H. Ma, J. He, *Appl. Phys. Lett.* **2016**, *109*, 213105.
- [148] H. Huang, J. Wang, W. Hu, L. Liao, P. Wang, X. Wang, F. Gong, Y. Chen, G. Wu, W. Luo, H. Shen, T. Lin, J. Sun, X. Meng, X. Chen, J. Chu, *Nanotechnology* **2016**, *27*, 445201.
- [149] S. H. Jo, H. Y. Park, D. H. Kang, J. Shim, J. Jeon, S. Choi, M. Kim, Y. Park, J. Lee, Y. J. Song, S. Lee, J. H. Park, *Adv. Mater.* **2016**, *28*, 6518.
- [150] Q. Liang, Q. Wang, Q. Zhang, J. Wei, S. X. Lim, R. Zhu, J. Hu, W. Wei, C. Lee, C. Sow, W. Zhang, A. T. S. Wee, *Adv. Mater.* **2019**, *31*, 1807609.
- [151] T. Jiang, Y. Zang, H. Sun, X. Zheng, Y. Liu, Y. Gong, L. Fang, X. Cheng, K. He, *Adv. Opt. Mater.* **2017**, *5*, 1600727.
- [152] J. Guo, Y. Liu, Y. Ma, E. Zhu, S. Lee, Z. Lu, Z. Zhao, C. Xu, S. J. Lee, H. Wu, K. Kovnir, Y. Huang, X. Duan, *Adv. Mater.* **2018**, *30*, 1705934.
- [153] Y. Wang, P. Wu, Z. Wang, M. Luo, F. Zhong, X. Ge, K. Zhang, M. Peng, Y. Ye, Q. Li, H. Ge, J. Ye, T. He, Y. Chen, T. Xu, C. Yu, Y. Wang, Z. Hu, X. Zhou, C. Shan, M. Long, P. Wang, P. Zhou, W. Hu, *Adv. Mater.* **2020**, *32*, 2005037.
- [154] J. Lai, Y. Liu, J. Ma, X. Zhuo, Y. Peng, W. Lu, Z. Liu, J. Chen, D. Sun, *ACS Nano* **2018**, *12*, 4055.
- [155] W. Yan, B. C. Johnson, S. Balendhran, J. Cadusch, D. Yan, J. I. Michel, S. Wang, T. Zheng, K. Crozier, J. Bullock, *ACS Appl. Mater. Interfaces* **2021**, *13*, 38.
- [156] M. Buscema, D. J. Groenendijk, S. I. Blanter, G. A. Steele, H. S. van der Zant, A. Castellanos-Gomez, *Nano Lett.* **2014**, *14*, 3347.
- [157] M. Huang, M. Wang, C. Chen, Z. Ma, X. Li, J. Han, Y. Wu, *Adv. Mater.* **2016**, *28*, 3481.
- [158] Q. Guo, A. Pospischil, M. Bhuiyan, H. Jiang, H. Tian, D. Farmer, B. Deng, C. Li, S. J. Han, H. Wang, Q. Xia, T. P. Ma, T. Mueller, F. Xia, *Nano Lett.* **2016**, *16*, 4648.
- [159] W. C. Tan, L. Huang, R. J. Ng, L. Wang, D. M. N. Hasan, T. J. Duffin, K. S. Kumar, C. A. Nijhuis, C. Lee, K. W. Ang, *Adv. Mater.* **2018**, *30*, 1705039.
- [160] L. Tong, X. Huang, P. Wang, L. Ye, M. Peng, L. An, Q. Sun, Y. Zhang, G. Yang, Z. Li, F. Zhong, F. Wang, Y. Wang, M. Motlag, W. Wu, G. J. Cheng, W. Hu, *Nat. Commun.* **2020**, *11*, 2308.
- [161] X. Wang, P. Wang, J. Wang, W. Hu, X. Zhou, N. Guo, H. Huang, S. Sun, H. Shen, T. Lin, M. Tang, L. Liao, A. Jiang, J. Sun, X. Meng, X. Chen, W. Lu, J. Chu, *Adv. Mater.* **2015**, *27*, 6575.
- [162] D. Kufer, G. Konstantatos, *ACS Photonics* **2016**, *3*, 2197.
- [163] Z. Sun, Z. Liu, J. Li, G. A. Tai, S. P. Lau, F. Yan, *Adv. Mater.* **2012**, *24*, 5878.
- [164] X. Yu, Y. Li, X. Hu, D. Zhang, Y. Tao, Z. Liu, Y. He, M. A. Haque, Z. Liu, T. Wu, Q. J. Wang, *Nat. Commun.* **2018**, *9*, 4299.
- [165] Y. Liu, F. Wang, X. Wang, X. Wang, E. Flahaut, X. Liu, Y. Li, X. Wang, Y. Xu, Y. Shi, R. Zhang, *Nat. Commun.* **2015**, *6*, 8589.
- [166] F. Yang, K. Yu, H. Cong, C. Xue, B. Cheng, N. Wang, L. Zhou, Z. Liu, Q. Wang, *ACS Photonics* **2019**, *6*, 1199.
- [167] L. Ye, P. Wang, W. Luo, F. Gong, L. Liao, T. Liu, L. Tong, J. Zang, J. Xu, W. Hu, *Nano Energy* **2017**, *37*, 53.
- [168] Y. Liu, B. N. Shivananju, Y. Wang, Y. Zhang, W. Yu, S. Xiao, T. Sun, W. Ma, H. Mu, S. Lin, H. Zhang, Y. Lu, C.-W. Qiu, S. Li, Q. Bao, *ACS Appl. Mater. Interfaces* **2017**, *9*, 36137.
- [169] L. Wang, J.-J. Li, Q. Fan, Z.-F. Huang, Y.-C. Lu, C. Xie, C.-Y. Wu, L.-B. Luo, *J. Mater. Chem. C* **2019**, *7*, 5019.
- [170] H. Qiao, J. Yuan, Z. Xu, C. Chen, S. Lin, Y. Wang, J. Song, Y. Liu, Q. Khan, H. Y. Hoh, C.-X. Pan, S. Li, Q. Bao, *ACS Nano* **2015**, *9*, 1886.
- [171] Y. Yu, Y. Zhang, X. Song, H. Zhang, M. Cao, Y. Che, H. Dai, J. Yang, H. Zhang, J. Yao, *ACS Photonics* **2017**, *4*, 950.
- [172] L. Gao, C. Chen, K. Zeng, C. Ge, D. Yang, H. Song, J. Tang, *Light: Sci. Appl.* **2016**, *5*, e16126.
- [173] M. Peng, X. Xie, H. Zheng, Y. Wang, Q. Zhuo, G. Yuan, W. Ma, M. Shao, Z. Wen, X. Sun, *ACS Appl. Mater. Interfaces* **2018**, *10*, 43887.
- [174] P. Luo, F. Zhuge, F. Wang, L. Lian, K. Liu, J. Zhang, T. Zhai, *ACS Nano* **2019**, *13*, 9028.
- [175] P. Vabbina, N. Choudhary, A. A. Chowdhury, R. Sinha, M. Karabiyik, S. Das, W. Choi, N. Pala, *ACS Appl. Mater. Interfaces* **2015**, *7*, 15206.
- [176] M. Long, E. Liu, P. Wang, A. Gao, H. Xia, W. Luo, B. Wang, J. Zeng, Y. Fu, K. Xu, W. Zhou, Y. Lv, S. Yao, M. Lu, Y. Chen, Z. Ni, Y. You, X. Zhang, S. Qin, Y. Shi, W. Hu, D. Xing, F. Miao, *Nano Lett.* **2016**, *16*, 2254.
- [177] K. Zhang, X. Fang, Y. Wang, Y. Wan, Q. Song, W. Zhai, Y. Li, G. Ran, Y. Ye, L. Dai, *ACS Appl. Mater. Interfaces* **2017**, *9*, 5392.
- [178] W. Deng, Y. Chen, C. You, B. An, B. Liu, S. Li, Y. Zhang, H. Yan, L. Sun, *2D Mater.* **2018**, *5*, 045027.
- [179] A. Li, Q. Chen, P. Wang, Y. Gan, T. Qi, P. Wang, F. Tang, J. Z. Wu, R. Chen, L. Zhang, Y. Gong, *Adv. Mater.* **2019**, *31*, 1970040.
- [180] J. Yuan, T. Sun, Z. Hu, W. Yu, W. Ma, K. Zhang, B. Sun, S. P. Lau, Q. Bao, S. Lin, S. Li, *ACS Appl. Mater. Interfaces* **2018**, *10*, 40614.
- [181] H. Li, L. Ye, J. Xu, *ACS Photonics* **2017**, *4*, 823.
- [182] A. M. Afzal, G. Dastgeer, M. Z. Iqbal, P. Gautam, M. M. Faisal, *ACS Appl. Mater. Interfaces* **2020**, *12*, 19625.
- [183] D. Jariwala, T. J. Marks, M. C. Hersam, *Nat. Mater.* **2017**, *16*, 170.
- [184] U. N. Noubme, C. Greboval, C. Livache, A. Chu, H. Majjad, L. E. Parra Lopez, L. D. N. Mouafo, B. Doudin, S. Berciaud, J. Chaste, A. Ouerghi, E. Lhuillier, J. F. Dayen, *ACS Nano* **2020**, *14*, 4567.
- [185] X. Liu, X. Ji, M. Liu, N. Liu, Z. Tao, Q. Dai, L. Wei, C. Li, X. Zhang, B. Wang, *ACS Appl. Mater. Interfaces* **2015**, *7*, 2452.
- [186] J. Miao, W. Hu, N. Guo, Z. Lu, X. Liu, L. Liao, P. Chen, T. Jiang, S. Wu, J. C. Ho, L. Wang, X. Chen, W. Lu, *Small* **2015**, *11*, 936.
- [187] Y. Cao, J. Zhu, J. Xu, J. He, J. L. Sun, Y. Wang, Z. Zhao, *Small* **2014**, *10*, 2345.
- [188] Z. Zhang, L. Zeng, X. Tong, Y. Gao, C. Xie, Y. Tsang, L. Luo, Y. Wu, *J. Phys. Chem. Lett.* **2018**, *9*, 1185.
- [189] L. Wang, J. Jie, Z. Shao, Q. Zhang, X. Zhang, Y. Wang, Z. Sun, S.-T. Lee, *Adv. Funct. Mater.* **2015**, *25*, 2910.
- [190] G. Li, L. Liu, G. Wu, W. Chen, S. Qin, Y. Wang, T. Zhang, *Small* **2016**, *12*, 5019.
- [191] L.-B. Luo, J.-J. Chen, M.-Z. Wang, H. Hu, C.-Y. Wu, Q. Li, L. Wang, J.-A. Huang, F.-X. Liang, *Adv. Funct. Mater.* **2014**, *24*, 2794.
- [192] Y.-L. Liu, C.-C. Yu, K.-T. Lin, T.-C. Yang, E.-Y. Wang, H.-L. Chen, L.-C. Chen, K.-H. Chen, *ACS Nano* **2015**, *9*, 5093.
- [193] F. Hao, P. Nordlander, Y. Sonnefraud, P. Van Dorpe, S. A. Maier, *ACS Nano* **2009**, *3*, 643.
- [194] A. Brioude, X. C. Jiang, M. P. Pileni, *J. Phys. Chem. B* **2005**, *109*, 13138.
- [195] Q. Zhang, Y. X. Hu, S. R. Guo, J. Goebel, Y. D. Yin, *Nano Lett.* **2010**, *10*, 5037.
- [196] K. F. Wu, W. E. Rodriguez-Cordoba, Y. Yang, T. Q. Lian, *Nano Lett.* **2013**, *13*, 5255.
- [197] C. Clavero, *Nat. Photonics* **2014**, *8*, 95.
- [198] M. W. Knight, H. Sobhani, P. Nordlander, N. J. Halas, *Science* **2011**, *332*, 702.
- [199] L. Shao, J. P. Zheng, *Appl. Mater. Today* **2019**, *15*, 6.
- [200] Y. N. Xia, Y. J. Xiong, B. Lim, S. E. Skrabalak, *Angew. Chem., Int. Ed.* **2009**, *48*, 60.
- [201] H. J. Chen, L. Shao, Q. Li, J. F. Wang, *Chem. Soc. Rev.* **2013**, *42*, 2679.
- [202] L. Shao, X. Wang, H. Xu, J. Wang, J.-B. Xu, L.-M. Peng, H.-Q. Lin, *Adv. Opt. Mater.* **2014**, *2*, 162.
- [203] G. W. Bryant, F. J. G. De Abajo, J. Aizpurua, *Nano Lett.* **2008**, *8*, 631.
- [204] Z. Y. Fang, Y. M. Wang, Z. Liu, A. Schlather, P. M. Ajayan, F. H. L. Koppens, P. Nordlander, N. J. Halas, *ACS Nano* **2012**, *6*, 10222.
- [205] M. Ye, Y. Gao, J. J. Cadusch, S. Balendhran, K. B. Crozier, *Adv. Opt. Mater.* **2021**, *9*, 2001854.

- [206] T. Hong, B. Chamlagain, S. R. Hu, S. M. Weiss, Z. X. Zhou, Y. Q. Xu, *ACS Nano* **2015**, *9*, 5357.
- [207] J. Wei, Y. Li, L. Wang, W. Liao, B. Dong, C. Xu, C. Zhu, K.-W. Ang, C.-W. Qiu, C. Lee, *Nat. Commun.* **2020**, *11*, 6404.
- [208] Z. Chen, X. Li, J. Wang, L. Tao, M. Long, S. J. Liang, L. K. Ang, C. Shu, H. K. Tsang, J. B. Xu, *ACS Nano* **2017**, *11*, 430.
- [209] J. X. Guo, S. D. Li, Z. B. He, Y. Y. Li, Z. C. Lei, Y. Liu, W. Huang, T. X. Gong, Q. Q. Ai, L. N. Mao, Y. W. He, Y. Z. Ke, S. F. Zhou, B. Yu, *Appl. Surf. Sci.* **2019**, *483*, 1037.
- [210] C. L. Haynes, R. P. Van Duyne, *J. Phys. Chem. B* **2001**, *105*, 5599.
- [211] A. Ferreira, N. M. R. Peres, R. M. Ribeiro, T. Stauber, *Phys. Rev. B* **2012**, *85*, 115438.
- [212] W. Yan, V. R. Shresha, Q. Jeangros, N. S. Azar, S. Balendhran, C. Ballif, K. Crozier, J. Bullock, *ACS Nano* **2020**, *14*, 13465.
- [213] X. T. Gan, K. F. Mak, Y. D. Gao, Y. M. You, F. Hatami, J. Hone, T. F. Heinz, D. Englund, *Nano Lett.* **2012**, *12*, 5626.
- [214] C. H. Liu, J. J. Zheng, Y. Y. Chen, T. Fryett, A. Majumdar, *Opt. Mater. Express* **2019**, *9*, 384.
- [215] A. Majumdar, J. Kim, J. Vuckovic, F. Wang, *Nano Lett.* **2013**, *13*, 515.
- [216] M. Liu, X. Yin, E. Ulin-Avila, B. Geng, T. Zentgraf, L. Ju, F. Wang, X. Zhang, *Nature* **2011**, *474*, 64.
- [217] S. Deckoff-Jones, H. T. Lin, D. Kita, H. Y. Zheng, D. H. Li, W. Zhang, J. J. Hu, *J. Opt.* **2018**, *20*, 044004.
- [218] S. Das, W. Zhang, M. Demarteau, A. Hoffmann, M. Dubey, A. Roelofs, *Nano Lett.* **2014**, *14*, 5733.
- [219] Y. Zou, D. N. Zhang, H. T. Lin, L. Li, L. Moreel, J. Zhou, Q. Y. Du, O. Ogbuu, S. Danto, J. D. Musgraves, K. Richardson, K. D. Dobson, R. Birkmire, J. J. Hu, *Adv. Opt. Mater.* **2014**, *2*, 478.
- [220] Q. Y. Du, Y. Z. Huang, J. Y. Li, D. Kita, J. Michon, H. T. Lin, L. Li, S. Novak, K. Richardson, W. Zhang, J. J. Hu, *Opt. Lett.* **2016**, *41*, 3090.
- [221] P. Lucas, Z. Y. Yang, M. K. Fah, T. Luo, S. B. Jiang, C. Boussard-Pledel, M. L. Anne, B. Bureau, *Opt. Mater. Express* **2013**, *3*, 1049.
- [222] T. J. Karle, D. H. Brown, R. Wilson, M. Steer, T. F. Krauss, *IEEE J. Sel. Top. Quantum Electron.* **2002**, *8*, 909.
- [223] A. Martinez, J. Garcia, P. Sanchis, E. Cuesta-Soto, J. Blasco, J. Marti, *Opt. Lett.* **2007**, *32*, 635.
- [224] X. H. Cai, A. B. Sushkov, M. M. Jadidi, L. Nyakiti, R. L. Myers-Ward, D. K. Gaskill, T. E. Murphy, M. S. Fuhrer, H. D. Drew, *Nano Lett.* **2015**, *15*, 4295.
- [225] S. S. Xiao, X. L. Zhu, B. H. Li, N. A. Mortensen, *Phys. Rev. B* **2016**, *11*, 205418.
- [226] E. H. Hwang, S. Das Sarma, *Phys. Rev. B* **2007**, *75*, 205418.
- [227] L. Ju, B. S. Geng, J. Horng, C. Girit, M. Martin, Z. Hao, H. A. Bechtel, X. G. Liang, A. Zettl, Y. R. Shen, F. Wang, *Nano-technol.* **2011**, *6*, 630.
- [228] Z. Y. Fang, Y. M. Wang, A. E. Schather, Z. Liu, P. M. Ajayan, F. J. G. de Abajo, P. Nordlander, X. Zhu, N. J. Halas, *Nano Lett.* **2014**, *14*, 299.
- [229] S. Thongrattanasiri, F. H. L. Koppens, F. J. G. de Abajo, *Phys. Rev. Lett.* **2012**, *108*, 047401.
- [230] A. Safaei, S. Chandra, M. N. Leuenberger, D. Chanda, *ACS Nano* **2019**, *13*, 421.
- [231] Y. Cai, Z. Wei, C. Song, C. Tang, W. Han, X. Dong, *Chem. Soc. Rev.* **2019**, *48*, 22.
- [232] A. Pospischil, M. Humer, M. M. Furchi, D. Bachmann, R. Guider, T. Fromherz, T. Mueller, *Nat. Photonics* **2013**, *7*, 892.
- [233] N. Kornienko, D. D. Whitmore, Y. Yu, S. R. Leone, P. Yang, *ACS Nano* **2015**, *9*, 3951.
- [234] A. Onton, M. R. Lorenz, W. Reuter, *J. Appl. Phys.* **1971**, *42*, 3420.
- [235] W. Wu, D. De, S.-C. Chang, Y. Wang, H. Peng, J. Bao, S.-S. Pei, *Appl. Phys. Lett.* **2013**, *102*, 142106.
- [236] H. Yu, M. Liao, W. Zhao, G. Liu, X. J. Zhou, Z. Wei, X. Xu, K. Liu, Z. Hu, K. Deng, S. Zhou, J.-A. Shi, L. Gu, C. Shen, T. Zhang, L. Du, L. Xie, J. Zhu, W. Chen, R. Yang, D. Shi, G. Zhang, *ACS Nano* **2017**, *11*, 12001.



Jiajia Zha received his B.S. degree from Southeast University in 2017. After receiving his M.S. degree from Fudan University in 2020, he moved to the Department of Electrical Engineering in the City University of Hong Kong in 2020 to pursue his Ph.D. under the supervision of Asst. Prof. Chaoliang Tan. His research interests mainly include the nanoelectronics/optoelectronics based on 2D materials.



James Bullock completed his Ph.D. in engineering, as an Australian Renewable Energy Agency fellow, at the Australian National University. Following that, he was a postdoctoral researcher in the Electrical Engineering and Computer Sciences department at UC Berkeley and an affiliate in the Materials Sciences Division at the Lawrence Berkeley National Laboratory. James now heads the Sustainable Energy and Environmental Devices group in the Electrical and Electronic Engineering Department at the University of Melbourne.



Kenneth B. Crozier is currently a professor of physics and electronic engineering at the University of Melbourne. Prior to joining the University of Melbourne, he was an associate professor at Harvard University. He joined Harvard as an assistant professor of electrical engineering in 2004, and was promoted to associate professor in 2008. He received his undergraduate degrees in electrical engineering (with first class honors, with LR East Medal) and physics at the University of Melbourne. He received his M.S.E.E. and Ph.D. degrees in electrical engineering from Stanford University.



Chaoliang Tan is currently an assistant professor in the Department of Electrical Engineering at the City University of Hong Kong. He received his Ph.D. degree in materials science with Prof. Hua Zhang from Nanyang Technological University (Singapore) in June, 2016. After working as a research fellow at the same place for about one year, he worked as a postdoc research fellow in the University of California, Berkeley (with Prof. Ali Javey) for two years. Currently, his research interests focus on 2D materials for electronics/optoelectronics and engineering of layered materials and demonstration of their applications in biomedicine, energy storage, etc.